**Title**
Experimental Fast Ion Research on DIII-D

**Permalink**
https://escholarship.org/uc/item/79h4m3n3

**Author**
Lin, Daniel

**Publication Date**
2022

Peer reviewed|Thesis/dissertation

UNIVERSITY OF CALIFORNIA,
IRVINE


Experimental Fast Ion Research on DIII-D

DISSERTATION


submitted in partial satisfaction of the requirements
for the degree of


DOCTOR OF PHILOSOPHY

in Physics


by


Daniel J. Lin


Dissertation Committee:
Professor William W. Heidbrink, Chair
Professor Zhihong Lin
Professor Franklin J. Dollar


2022

# TABLE OF CONTENTS

# LIST OF FIGURES

vi

# LIST OF TABLES

# ACKNOWLEDGMENTS

I would like to first and foremost thank God for His continual grace and mercy that He has demonstrated in all aspects of my life.

I would like to thank my graduate advisor Bill Heidbrink for his guidance, mentorship, and encouragement in my development as a scientist.

I would like to thank my friends and cohort who studied alongside me and endured the plasma physics curriculum at UCI: Genevieve H. DeGranchamp, Kenneth R. Gage, Alvin V. Garcia, Eric C. Nelson, and Michael W.L. Seggebruch.

I would also like to thank the scientists at DIII-D who guided my development in addition to setting an example before me: Cami S. Collins, Xiaodi Du, Javier Gonzlez Martin, Jeff Lestz, Deyong Liu, Chris M. Muscatello, Luke E. Stagner, and Michael A. Van Zeeland.

Last but certainly not least, I would like to thank my family and friends for their support in my life.

Discussion from previously published works is presented in Sec. 2.4 (reproduced from [10] with permission from AIP Publishing) and Ch. 3 (reproduced from [11] with permission from IOP Publishing) while submitted work is presented in Ch. 4 [12].

# VITA

## Daniel J. Lin

### EDUCATION

**Doctor of Philosophy in Physics**                                   **2022**
University of California, Irvine                          *Irvine, California*

**Bachelor of Science in Physics**                                   **2016**
University of California, Irvine                          *Irvine, California*

**Bachelor of Science in Aerospace Engineering**                     **2016**
University of California, Irvine                          *Irvine, California*

### RESEARCH EXPERIENCE

**Graduate Student Researcher**                                  **2017–2022**
University of California, Irvine                          *Irvine, California*

**Junior Specialist**                                            **2016–2017**
University of California, Irvine                          *Irvine, California*

**Student Researcher**                                               **2016**
University of California, Irvine                          *Irvine, California*

### TEACHING EXPERIENCE

**Teaching Assistant**                                               **2018**
University of California, Irvine                          *Irvine, California*

### FIRST AUTHOR PUBLICATIONS

1. **D.J. Lin**, W.W. Heidbrink, N.A. Crocker, X.D. Du, R. Nazikian, M.A. Van Zeeland, and K. Barada. "Energetic Particle-Induced Geodesic Acoustic Modes on DIII-D" ***Submitted to Nucl. Fusion*** (2022)

2. **D.J. Lin**, C.M. Muscatello, and W.W. Heidbrink. "Development of a narrow stop-band filter for spectroscopic fast ion deuterium-alpha measurements" ***Rev. of Sci. Instrum.*** 92, 033107 (2021)

3. **D.J. Lin**, X.D. Du, W.W. Heidbrink, and M.A. Van Zeeland. "Validation of the imaging neutral particle analyzer in nearly MHD quiescent plasmas using injected beam ions on DIII-D" ***Nucl. Fusion*** 60 112008 (2020)

## CONFERENCE PRESENTATIONS

1. **D.J. Lin**, W.W. Heidbrink, M.A. Van Zeeland, X.D. Du, and R. Nazikian, "Energetic Particle-Induced Geodesic Acoustic Modes on DIII-D," *Contributed Oral*, **17**$^{th}$ **Technical Meeting on Energetic Particles and Theory of Plasma Instabilities in Magnetic Confinement Fusion**, Virtual Event, Dec. 6-10 2021

2. **D.J. Lin**, W.W. Heidbrink, M.A. Van Zeeland, and R. Nazikian, "Characterization of the Energetic Particle-Induced Geodesic Acoustic Modes on DIII-D," *Poster*, **63**$^{rd}$ **Annual Meeting of the APS Division of Plasma Physics**, Pittsburgh, Pennsylvania, Nov. 8-12 2021

3. **D.J. Lin**, C.M. Muscatello, and W.W. Heidbrink, "Development of a narrow stopband filter for spectroscopic fast ion deuterium-alpha measurements on DIII-D," *Poster*, **23**$^{rd}$ **Topical Conference on High Temperature Plasma Diagnostics**, Santa Fe, New Mexico, May 31 - Jun 4 2020

4. **D.J. Lin**, X.D. Du, W.W. Heidbrink, and M.A. Van Zeeland, "Validation of the Imaging Neutral Particle Analyzer via Pitch Angle Scattering of Injected Beam Ions," *Poster*, **16**$^{th}$ **Technical Meeting on Energetic Particles in Magnetic Confinement Systems — Theory of Plasma Instabilities (EPPI 2019)**, Shizuoka City, Japan, Sep. 3-6 2019

5. **D.J. Lin**, X.D. Du, W.W. Heidbrink, and M.A. Van Zeeland, "Verification of the Imaging Neutral Particle Analyzer via Pitch Angle Scattering of Injected Beam Ions," *Poster*, **60**$^{th}$ **Annual Meeting of the APS Division of Plasma Physics**, Portland, Oregon, Nov. 5-9 2018

6. **D.J. Lin**, C.S. Collins, W.W. Heidbrink, G.J. Kramer, D.C. Pace, C.C. Petty, M. Podesta, L. Stagner, M.A. Van Zeeland, R. White, Y. Zhu, and the DIII-D team. "Fast-ion Profiles in DIII-D Discharges with Alfvén Eigenmode Activity," *Contributed Oral*, **15**$^{th}$ **IAEA Technical Meeting on Energetic Particles in Magnetic Confinement Systems**, Princeton, New Jersey, Sep. 5-8 2017

## CO-AUTHOR PUBLICATIONS

1. C. Marini, C.S. Collins, M.A. Van Zeeland, K.E. Thome, W.W. Heidbrink, and **D. Lin**. "The imaging fast ion D-alpha diagnostic (IFIDA) on DIII-D" ***Rev. of Sci. Instrum.*** **92, 033533 (2021)**

2. X.D. Du, M.A. Van Zeeland, W.W. Heidbrink, J. Gonzalez-Martin, K. Särkimäki, A. Snicker, **D. Lin**, C.S. Collins, M.E. Austin, G.R. McKee, Z. Yan, Y. Todo, and W. Wu. "Visualization of Fast Ion Phase-Space Flow Driven by Alfvén Instabilities" ***Phys. Rev. Lett.*** **127, 235002 (2021)**

3. X.D. Du, M.A. Van Zeeland, W.W. Heidbrink, L. Stagner, A. Wingen, **D. Lin** and C.S. Collins. "Resolving the fast ion distribution from imaging neutral particle analyzer measurements" ***Nucl. Fusion*** **60 112001 (2020)**

4. B. Madsen, M. Salewski, W.W. Heidbrink, L. Stagner, M. Podestà, **D. Lin**, A.V. Garcia, P.C. Hansen, J. Huang and the DIII-D team. "Tomography of the positive-pitch fast-ion velocity distribution in DIII-D plasmas with Alfvén eigenmodes and neoclassical tearing modes" ***Nucl. Fusion*** **60 066024 (2020)**

5. M.A. Van Zeeland, C.S. Collins, W.W. Heidbrink, M.E. Austin, X.D. Du, V.N. Duarte, A. Hyatt, G. Kramer, N. Gorelenkov, B. Grierson, **D. Lin**, A. Marinoni, G. McKee, C. Muscatello, C. Petty, C. Sung, K.E. Thome, M. Walker and Y.B. Zhu. "Alfvén eigenmodes and fast ion transport in negative triangularity DIII-D plasmas" ***Nucl. Fusion*** **59 086028 (2019)**

6. W.W. Heidbrink, L. Bardoczi, C.S. Collins, G.J. Kramer, R.J. La Haye, **D.J. Lin**, C.M. Muscatello, M. Podestà, L. Stagner, M.A. Van Zeeland and Y.B. Zhu. "The phase-space dependence of fast-ion interaction with tearing modes" ***Nucl. Fusion*** **58 082027 (2018)**

# ABSTRACT OF THE DISSERTATION

Experimental Fast Ion Research on DIII-D

By

Daniel J. Lin

Doctor of Philosophy in Physics

University of California, Irvine, 2022

Professor William W. Heidbrink, Chair

Fast ion research is necessary to understand confinement of high energy particles in fusion devices like DIII-D. Measuring the fast ion distribution is necessary to understand how well it is confined. The fast ion D-alpha (FIDA) diagnostic and neutral particle analyzer (NPA) are two diagnostics that measure part of the distribution. Upgrades to the FIDA diagnostic are necessary to resolve scattering issues from the unshifted D-alpha emission that contaminates other parts of the measured spectra. Effective filter performance is possible using the reflection of a narrow bandpass filter. The imaging neutral particle analyzer (INPA) was developed on DIII-D to provide greater spatial and energy resolution compared to traditional NPAs. Measured images are validated using simulations. Robust passive signals are also observed and found to come from fast ion populations traversing the edge. Fast ions can also interact with plasma waves or modes to transfer energy which can lead to losses. The energetic particle-induced geodesic acoustic mode (EGAM) is one plasma mode that is excited by fast ions. Various phenomena associated with EGAMs are characterized to assess the impact it has on fast ions.

# Chapter 1

# Introduction

## 1.1 Fusion energy

Fusion is the process in which two nuclei are combined to form a heavier nucleus. Generally, energy can be extracted from the release of binding energy if the nucleus mass is below that of $Fe^{56}$. Nature utilizes this process to power stars, like the Sun. Stars are born when hydrogen gas in space coalesce through gravitational attraction. As the gas becomes more dense, collisions heat it up until it gains enough energy for the electrons to separate from the nucleus (ions). The shift from a collection of neutral particles to charged particles give rise to an additional force (electromagnetic force) to mediate interactions between particles. This collection of electrons and ions that interact with each other is essentially a plasma. In order for fusion to occur in plasmas, ions must overcome the Coulomb repulsion to get close enough to fuse. Stars are considered to be burning plasmas since it is primarily heated by fusion reactions. Not only that, they have also reached the point where the fusion reaction is self sustaining (fusion ignition).

Fusion energy is considered to be a viable pathway towards achieving clean and sustainable

energy on Earth. While gravitational confinement of plasma is used by stars, it is not a feasible method here on Earth. Instead, other methods are considered for confinement. One popular method uses inertial confinement. The fundamental idea behind inertial confinement fusion (ICF) is to uniformly compress a fuel pellet using powerful lasers. The fuel within the pellet would then fuse and release energy.

Magnetic confinement fusion (MCF) is the other popular way to achieve fusion on Earth. MCF, as the name suggests, uses magnetic fields to confine charged particles that make up the plasma. Any motion perpendicular to the magnetic field direction is redirected based on the Lorentz force, $F = q(v \times B)$, which results in a cyclic motion (gyromotion) around a central point (guiding center). Under a uniform magnetic field, the guiding center of the particle would not drift away from the initial field line that it follows.

Stars like our Sun are able to fuse hydrogen ($^1_1H$) and produce net energy because of passive confinement from gravity. Terrestrial methods require active confinement methods which provides more constraints towards achieving net energy gain. Choosing more favorable fusion reactions, like using deuterium ($^2_1H = {}^2_1D$) and tritium ($^3_1H = {}^3_1T$), helps improve the efficiency of a potential reactor. Processes that will most likely be used are as follows:

$$^2_1D + {}^3_1T \longrightarrow {}^4_2He \ (3.52 \ MeV) + n^0 \ (14.06 \ MeV) \tag{1.1}$$

$$^2_1D + {}^2_1D \longrightarrow {}^3_1T \ (1.01 \ MeV) + p^+ \ (3.02 \ MeV) \tag{1.2}$$

$$^2_1D + {}^2_1D \longrightarrow {}^3_2He \ (0.82 \ MeV) + n^0 \ (2.45 \ MeV) \tag{1.3}$$

$$^2_1D + {}^3_2He \longrightarrow {}^4_2He \ (3.60 \ MeV) + p^+ \ (14.70 \ MeV) \tag{1.4}$$
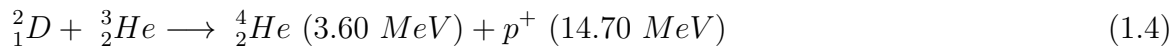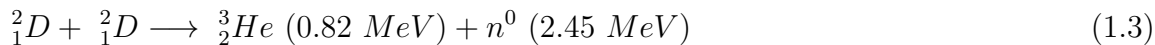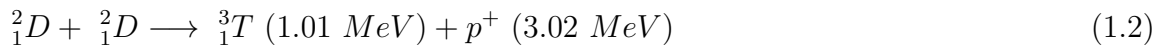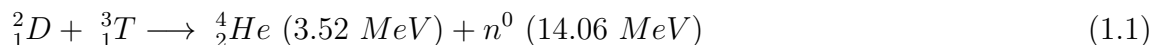
In addition to choosing the right reaction, using the right conditions can also improve the efficiency. The probability (or cross section) for fusion reactions to occur between two particles depend on the energy (or temperature) of the particles. A plot for the cross section of fusion reactions is shown in Fig. 1.1 where the probability for the fusion reaction generally
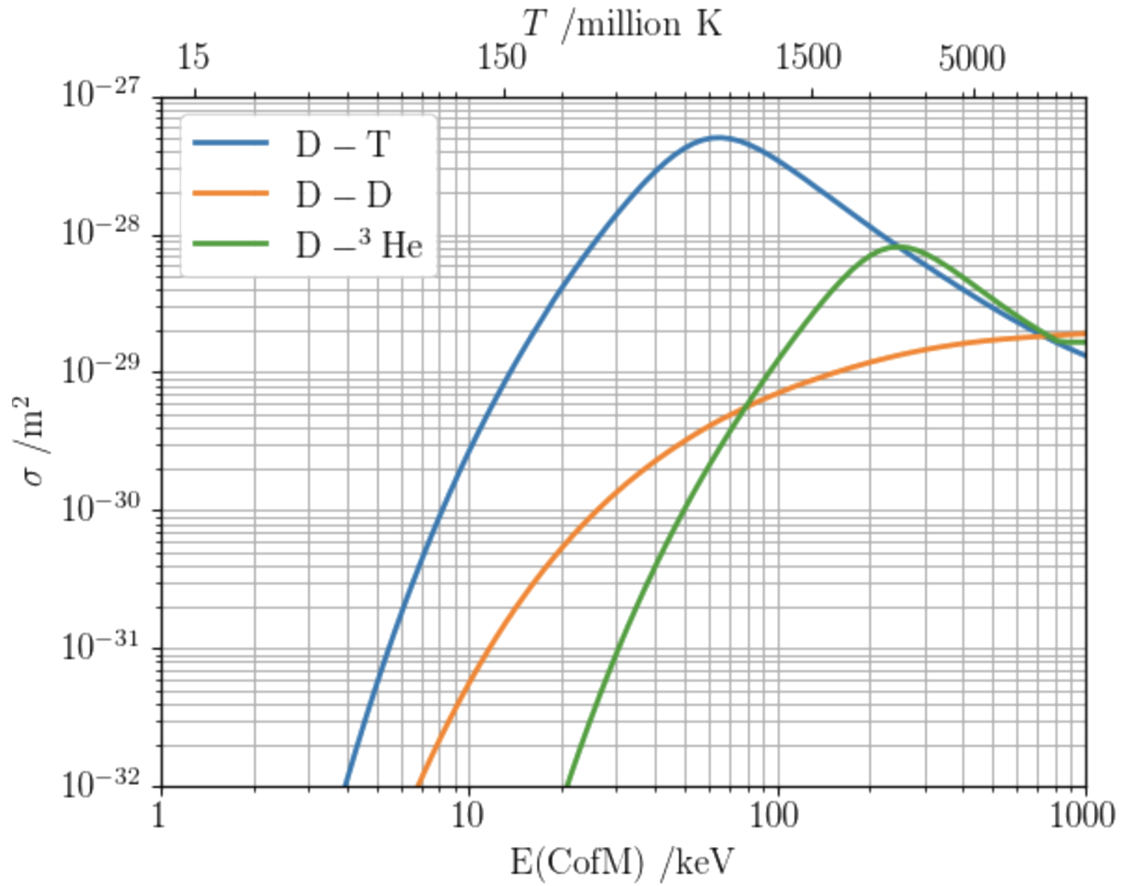
Figure 1.1: Fusion cross sections are shown for D-T (blue), D-D (orange), and D-He (green). Cross sections generally increase as the energy increases. Data for this figure is taken from [1]

increases with the energy of the particles. The reaction involving deuterium and tritium have the highest cross section and peaks at the lowest temperature which makes it an attractive choice. The amount of fusion power produced is also modified by the density. In general, increasing the density increases the amount of fusion power produced, since having more particles increases the number of fusion reactions.

## 1.2 Tokamak

One popular device in the magnetic confinement category is the tokamak. A tokamak is a torus shaped device that uses external coils to produce a magnetic field (B-field) in the toroidal direction (along the torus) and relies on the plasma current to produce a poloidal B-field (directed around the cross section). The resulting field is a helical shape that winds along the direction of the torus. Figure 1.2 shows an example of field lines in the tokamak. Because the B-field is not uniform, charged particles are not strictly confined to one field line. In a tokamak, the nonuniformity is primarily caused by the varying magnitude of the B-field over the cross section (grad B) and the curvature of the B-field. The drifts are described by

$$\vec{v}_{\nabla B} = \frac{W_\perp}{qB} \frac{\vec{B} \times \nabla B}{B^2} \tag{1.5}$$

$$\vec{v}_R = \frac{2W_\parallel}{qB} \frac{\vec{R}_c \times \vec{B}}{R_c^2 B} \tag{1.6}$$

where $\vec{v}_{\nabla B}$ is the grad B drift, $W_\perp$ is the energy of the perpendicular velocity component, $q$ is the charge of the particle, $B$ is the magnetic field, $\vec{v}_R$ is the curvature drift, $W_\parallel$ is the energy of the parallel velocity component, and $\vec{R}_c$ is the radius of curvature. Considering only the toroidal B-field, the curvature drift (Eq. 1.6) is pointed in opposite directions depending on the charge of the particle (positive for ions and negative for electrons). This can create charge separation that introduces an electric field leading to the $\vec{E} \times \vec{B}$ drift (Eq. 1.7).

$$\vec{v}_E = \frac{\vec{E} \times \vec{B}}{B^2} \tag{1.7}$$

In this case particles will drift out of the confined region and be lost. The helical structure of the total B-field mitigates the effects of these drifts. As particles follow the field line, half of the trajectory causes outward drifts (away from the center) while the other half causes inward drifts (towards the center).
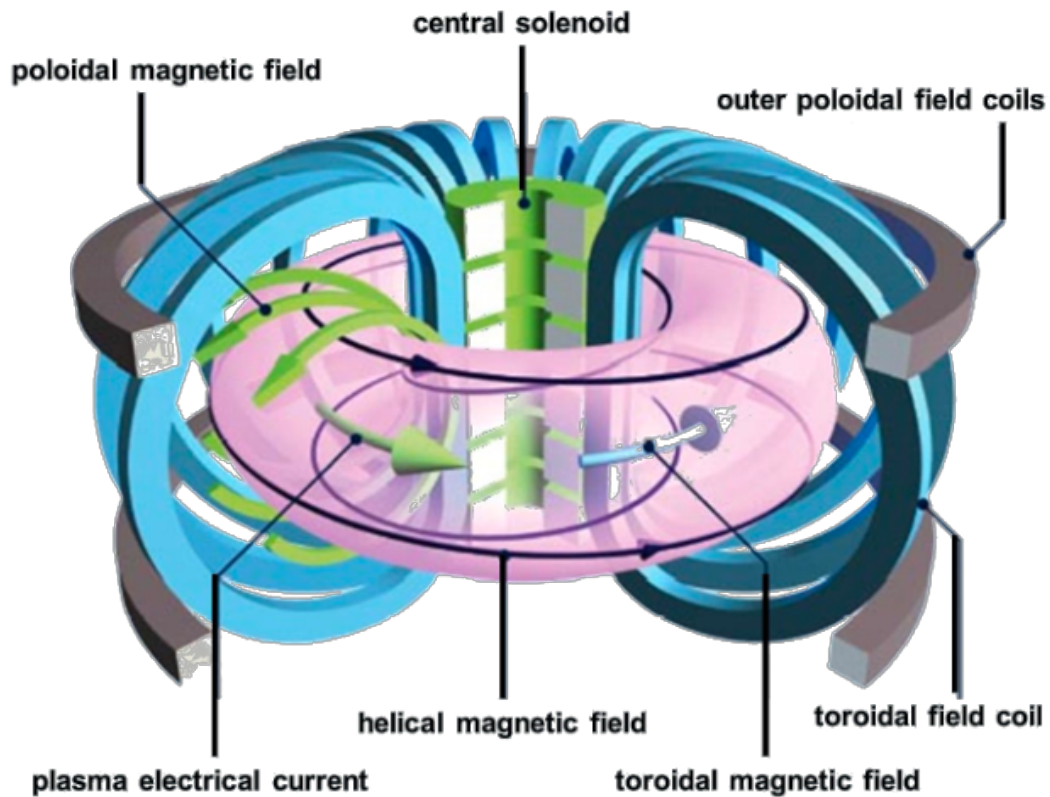
Figure 1.2: The helical magnetic field structure (black) inside the tokamak is shown. The magnetic field in the toroidal direction is produced by the external field coil while the magnetic field in the poloidal direction is produced by the plasma current. Figure is taken from [2]

In order to increase the likelihood of fusion reactions occurring, the plasma temperature needs to be raised. Two popular methods used to achieve this are radio frequency (RF) heating and neutral beam injection (NBI). RF heating uses radio frequency waves that resonate with the particle gyration frequency to transfer energy. In ion cyclotron resonance heating (ICRH), energy is directly transferred to the ions from the wave, while in electron cyclotron resonance heating (ECRH), energy is provided to the electrons which in turn transfers it to the ions through collisions. For NBI, neutral gas in a chamber is ionized and accelerated through electrostatic grids before they are neutralized again and enter the device. Once the neutral particles enter the device, they are ionized through interactions with the bulk plasma. Collisional processes allow energy to be transferred from these energetic ions to the rest of the plasma. In addition to heating the plasma, this method also introduces more particles into the plasma. The penetration of the deposition depends on the plasma density profile. Both heating methods utilize plasma collisions to mediate the transfer of energy to the bulk plasma.

First wall components play an important role in protecting the vacuum vessel from deterioration caused by the plasma. Particles that lose confinement impart their energies onto the wall. This is especially critical when large losses create particle heat fluxes that need to be absorbed by the wall. Materials like tungsten or carbon are typically used to absorb heat loads without melting. The composition of the material can also lead to inward fluxes of undesired particles into the confined plasma. Escaping high energy ions can also interact with the wall to sputter material (impurities). These particles, when recycled back into the bulk plasma, can absorb and radiate energy. This lowers heating efficiency by diverting energy away from fusion reactants. Divertors are used to capture and remove waste material (including impurities and fusion products) from the confined plasma.

Plasma scenarios are designed to leverage different tokamak physics and phenoma in a way that maximizes the fusion energy output while using different control methods to avoid
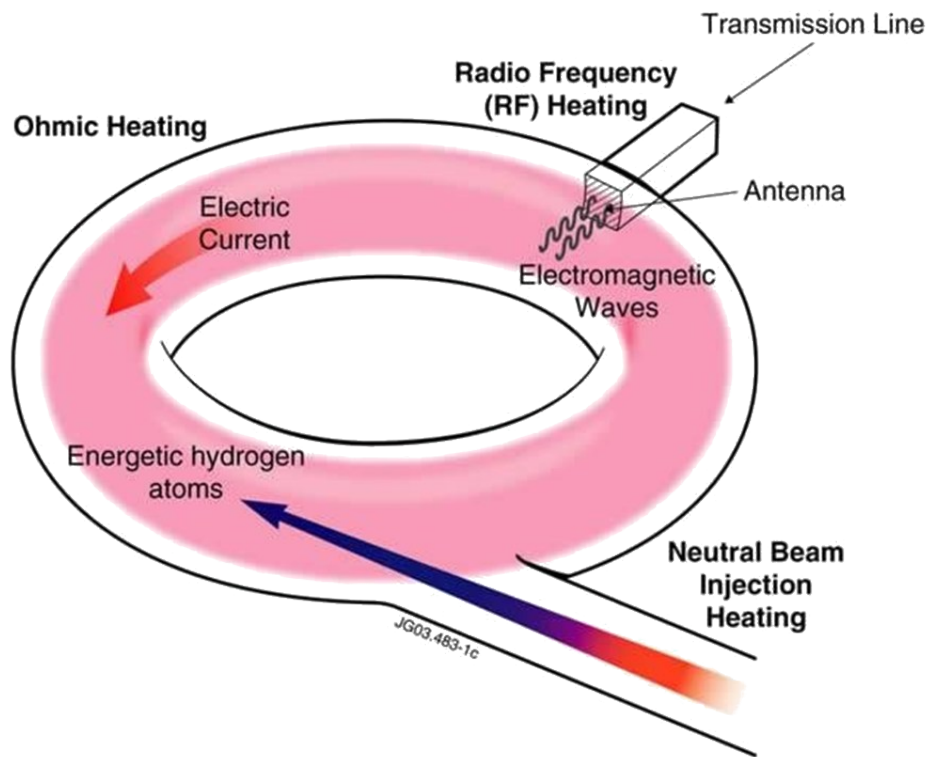
Figure 1.3: Different mechanisms for heating the plasma is shown. Radio frequency heating injects electromagnetic waves that imparts its energy on particles it resonates with. Neutral beams injection heats the plasma by adding high energy particles into the plasma population. Figure is taken from [3].

7

any deleterious regimes. The major operational physics parameters that are examined are temperature, density, current, and magnetic field. There are operational limits associated with each parameter. For example, while it is desirable to increase the plasma density as high as possible (to increase the fusion power), it can only be operationally increased up to a threshold (Greenwald density limit). Further increases in density past this threshold will cause the plasma to lose confinement and expel its energy onto the wall in an event called a disruption. Control systems can be put in place to regulate and ensure that the density stays safely below the threshold.

## 1.3　Fast ion population

Fast ions are a population of particles that have energies greater than that of the bulk ions. On DIII-D, this population of particles is typically generated from injected beam ions. Continuous injection would lead to a slowing down distribution caused by plasma collisions.

The fast ion distribution is described with a 6D phase space coordinate system (3D in configuration space and 3D in velocity space). For configuration space, cylindrical coordinates of radius $r$, elevation $z$, and toroidal angle $\phi$ are used. Tokamaks are considered axisymmetric so the toroidal angle dimension is usually ignored, reducing the spatial dimension to 2D $(r, z)$. For velocity space, guiding center coordinates of energy $(E)$, pitch $(p = v_{||}/v)$, and gyrophase $(\alpha)$ are used. This coordinate describes the trajectory of a particle relative to direction of the local B-field. The magnitude of the particle velocity is described by the energy, while the direction of the particle can be separated by the guiding center motion (described by pitch) and the gyromotion (described by the gyrophase). The gyromotion is usually assumed to be negligible since its effect is usually on a much faster time scale and a much smaller spatial scale than the time and space of interest. With all the assumptions, the fast ion distribution can be described by 4D $(E, p, r, z)$.
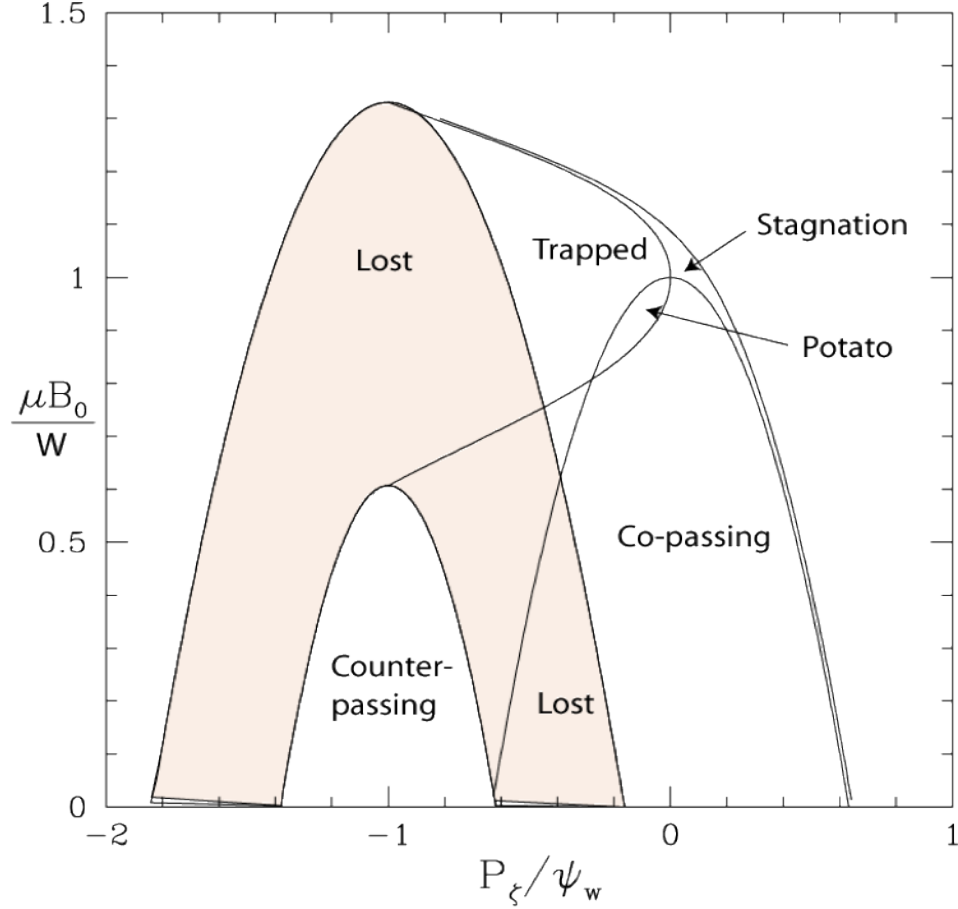
Figure 1.4: Different classification of orbits are shown in the space of normalized canonical angular momentum and normalized magnetic moment for fixed energy. Figure is taken from [4].

Further reduction of the dimensions can be reduced by transforming into constants of motions space where quantities are generally conserved. Here, the coordinates are energy $(E)$, toroidal canonical angular momentum $(P_\phi = mrv_\phi + q\Psi_p)$, and magnetic moment $(\mu = \frac{W_\perp}{B})$. Figure 1.4 shows a plot of the different orbit topologies in the space of normalized toroidal canonical angular momentum and normalized magnetic moment for a given energy. Different regions correspond to different classifications of orbit trajectories. The shaded region indicates particles on lost orbits. Perturbations from waves or instabilities can push particles, near the lost boundary, into the lost region.

At the start of injection, the distribution appears as a 2D Gaussian in the velocity space of
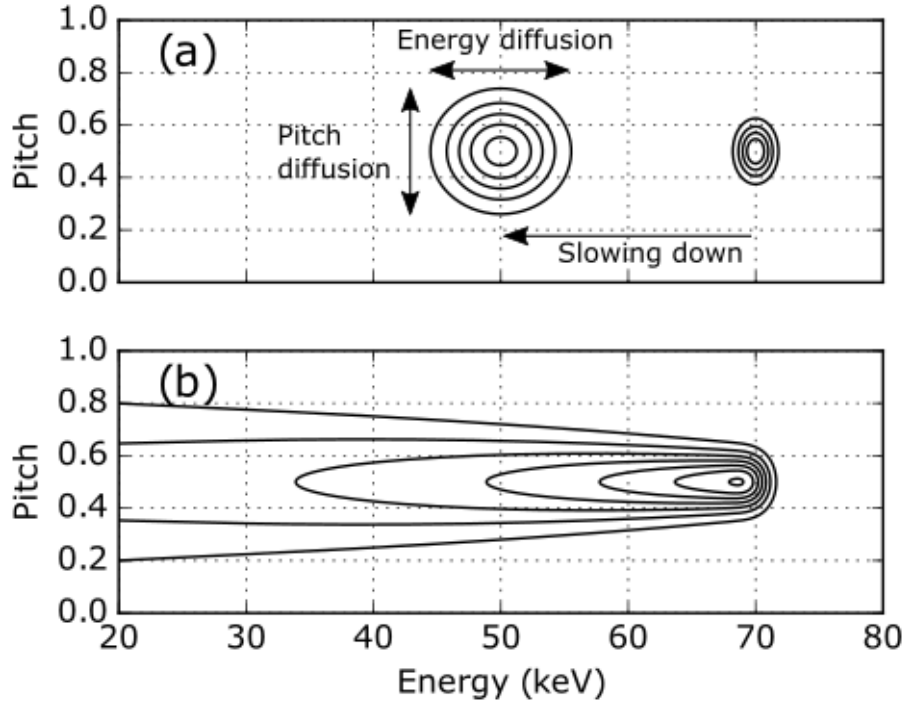
Figure 1.5: (a) Different scattering effects on a Gaussian distribution is shown. The energy and pitch diffusion increases the spread while the slowing down process shifts the distribution down in energy. (b) The typical shape for a full slowing down distribution is shown. This happens when scattering processes occur with a constant source.

energy ($E$) and pitch ($p$). As time evolves, the distribution will be modified through collisions with the bulk plasma resulting in 3 different scattering mechanisms: energy diffusion, pitch diffusion, and slowing down. The energy and pitch diffusion process increases the spread of the distribution while the slowing down process shifts the entire distribution down in energy. Figure 1.5(a) demonstrates the different scattering effects on a Gaussian source and Fig. 1.5(b) shows the full slowing down distribution with a constant source. In reality, the neutral beams introduce particles at three energy levels corresponding to the different molecular species being accelerated to the same energy. This results in the combination of three slowing down distributions contributing to the fast ion population.

## 1.4  Plasma waves and instabilities

Good energetic particle confinement is needed to achieve burning plasmas. Transport mechanisms, such as wave particle resonances, can cause energetic particle losses [13, 14]. Localized losses of energetic particles can cause intolerable heat loads on first wall components. Additionally, efficiency of heating mechanisms is dependent on energetic particle confinement. Waves and instabilities in plasma can cause losses of energetic particles thereby decreasing the heating efficiency.

In general waves are oscillating disturbances in an equilibrium medium. The amplitude of the wave can grow or shrink depending on the drive and damping mechanisms. Waves are typically considered as instabilities when their amplitude grows with time during its linear phase. Plasma waves can exchange energy through any of the orbital motion. Energy can be gained/lost by the particle if the wave is in/out of phase with the cyclic motion. As a result, the constants of motions associated with the particle is no longer conserved which can cause a change in orbit type. This becomes detrimental when particles on confined orbits become lost.

Energetic particles can transfer energy to plasma waves through wave-particle resonance [14]. This can occur when the particle motion is in phase with the wave such that

$$\Delta W = \oint q\mathbf{E} \cdot d\mathbf{l} \tag{1.8}$$

where $\Delta W$ is the energy change, $q$ is the particle charge, $\mathbf{E}$ is the electric field of the wave, and $\mathbf{dl}$ is the instantaneous path of the particle. This can be generalized to

$$\omega = l\omega_c + m\omega_\theta + n\omega_\phi \tag{1.9}$$

where the mode frequency $\omega$ matches some integer combination of the particle cyclotron

frequency $\omega_c$, poloidal frequency $\omega_\theta$, and toroidal frequency $\omega_\phi$.

From Ref. [15], the energy transferred to a wave from a distribution of particles, assuming the magnetic moment $\mu$ is conserved, is described by

$$\frac{\partial f}{\partial E}\bigg|_{E'} = \frac{\partial f}{\partial E}\bigg|_{P_\phi} + \frac{n}{\omega}\frac{\partial f}{\partial P_\phi}\bigg|_E \tag{1.10}$$

where $f$ is the energetic particle distribution function, $E' = E + \omega P_\phi$ is the conserved quantity, $E$ is the energy, $P_\phi$ is the canonical toroidal angular momentum, $\omega$ is the wave frequency, and n is the toroidal mode number.

Multiple instabilities can overlap to create a stochastic region which leads to large losses of particles. Within the stochastic region, particle trajectories are largely influenced by diffusive processes. This leads to phenomena such as the critical gradient threshold [16, 13]. As the neutral beam injects more power into the plasma, the energetic particle population increases up to a threshold; further increases in beam power results in higher losses of injected particles. Since energy transfer in wave particle resonances can go both ways, plasma waves can also be useful in facilitating energy transport between different populations. This is the basic idea behind alpha channelling [17]. Fusion reactions create high energy alpha particles that can be used to heat the bulk plasma. Wave particle interaction is thought to be one possible way to facilitate the flow of energy.

## 1.5  Roadmap

The proceeding chapters cover studies in different aspects of fast ion research on the DIII-D tokamak. Chapter 2 presents different techniques used to measure different plasma quantities including a more in depth discussion on developments to improve the fast ion D-alpha (FIDA) diagnostic. Chapter 3 presents validation work of the imaging neutral particle analyzer

(INPA) by simulating different distribution functions to reproduce experimental images. Chapter 4 discusses the effort to characterize the energetic particle-driven geodesic acoustic mode (EGAM) that is, as the name suggests, driven by energetic particles. Chapter 5 gives a brief summary of the main findings for each study and provides an outlook on future research directions. Appendix A provides documentation for the FIDA data analysis GUI. Appendix B provides tables of quantities correlated to the frequency and stability of EGAMs.

# Chapter 2

# Diagnostics

## 2.1 General plasma diagnostics

Measuring plasma conditions is necessary to evaluate the performance. To do so, multiple diagnostics are used to take advantage of certain properties and mechanisms of plasmas. One of the most common diagnostic in tokamak plasmas is the Thomson scattering diagnostic. This diagnostic utilizes probing lasers that scatter off electrons, where the shape of the emission is assumed to be a Gaussian. The intensity of the emission provides information for the electron density and the width provides information on the temperature. Spatial coverage is provided by collection optics with line of sights that intersect the laser at different radii.

The magnetic fields are measured by probes along the edge of the device. There are different types of probes but they all operate under the same principle of Faraday's law

$$V = -\frac{d\Phi}{dt} \tag{2.1}$$

where $V$ is the measured voltage, $\Phi = NAB$ is the magnetic flux over the enclosed area, and
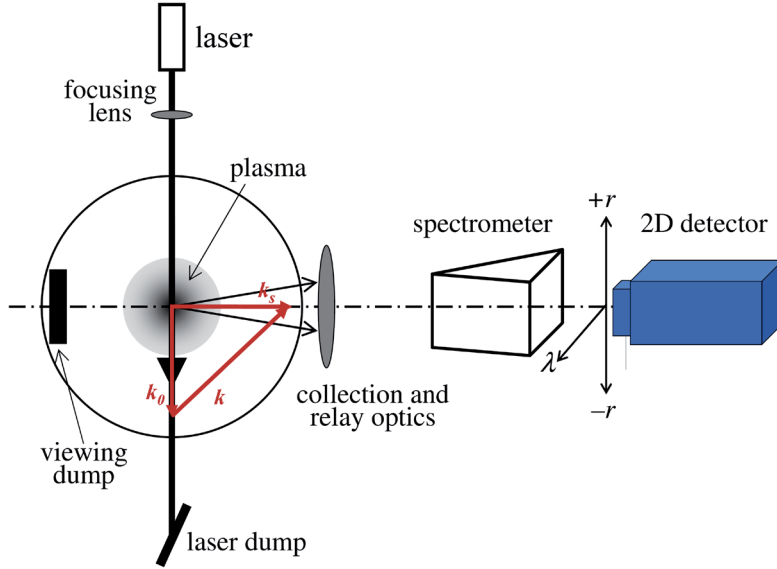
Figure 2.1: Schematic for the operating principle of the Thomson scattering diagnostic. Figure taken from [5].

$\frac{d\Phi}{dt}$ is the change in flux over time. Integrator circuits are used to obtain the measurement of the magnetic field at the probe. These measurements are useful in inferring the magnetic structure within the device by constraining the solution of the Grad-Shafranov equation (ideal MHD solution for 2D plasma equilibrium) at the edge.

The equilibrium can be further constrained with internal pitch angle measurements of the magnetic field by the motional start effect (MSE) diagnostic. The measurement constrains the safety factor (q) which depends on the ratio of the toroidal to poloidal magnetic field. The diagnostic measures the different $\sigma$ and $\pi$ polarization emitted by particles injected by the neutral beams to determine the polarization angle. The different polarizations are present due to the motional stark effect experienced by the injected neutral particles in the presence of a magnetic field.

$$\vec{E} = \vec{v} \times \vec{B} \tag{2.2}$$

With the direction of $\vec{E}$ given by the different polarization components and the direction of
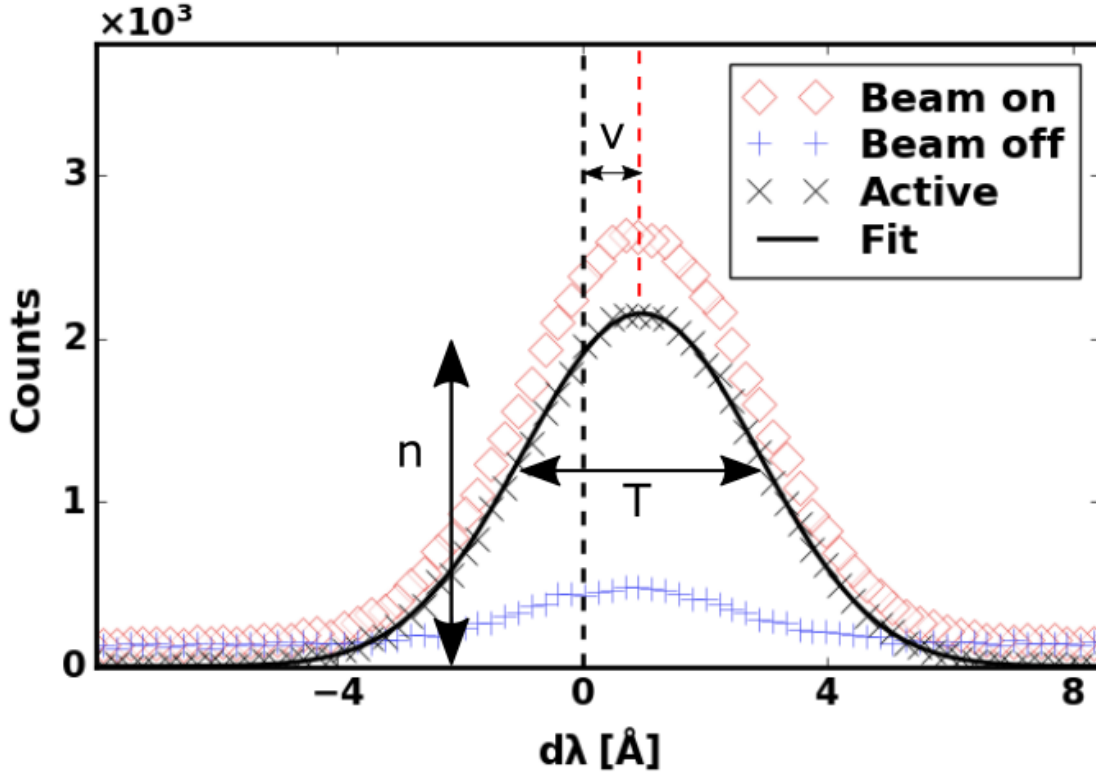
Figure 2.2: An example spectra measuring charge exchange emission is shown. Density is determined by the intensity of the emission, temperature is determined by the width of the Gaussian fit, and rotational velocity is determined by the shift in peak wavelength. Figure is provided courtesy of Cami Collins.

the particle trajectory $\vec{v}$ known, the direction of the magnetic field $\vec{B}$ at the measurement location can be calculated.

Information from plasma ions can be obtained with the charge exchange recombination (CER) diagnostic. Measurements of charge exchange emission between injected beam neutrals and impurity ions are made to obtain the impurity density, temperature, and rotation. Figure 2.2 shows an example spectrum measured by the CER diagnostic. Charge exchange emissions are also assumed to be Gaussian so the intensity of the signal corresponds to the density, the width of the Gaussian corresponds to the temperature, and the Doppler shift of the Gaussian peak corresponds to the rotational velocity.
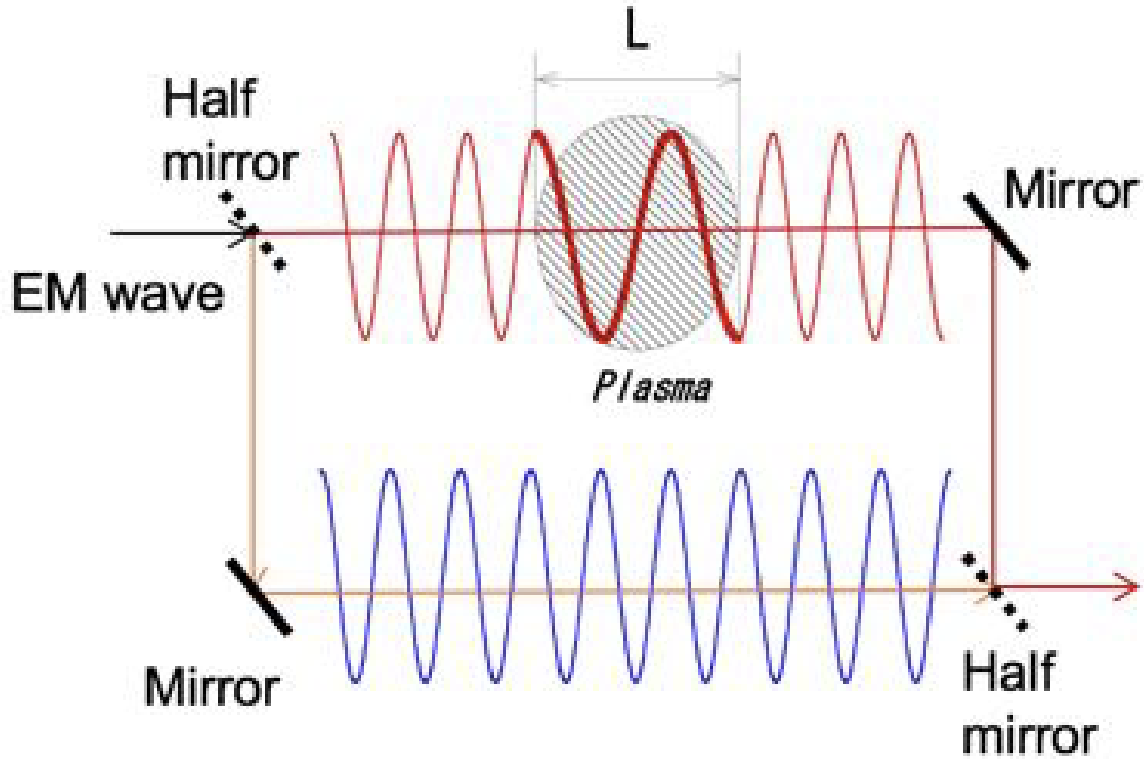
Figure 2.3: Schematic of interferometer principle is shown. Light from a laser is split and travels in two different paths of equal length. One path passes through the plasma and acquires a relative phase shift due to the refractive index of the plasma which depends on density. Figure is provided courtesy of Mike Van Zeeland.

The $CO_2$ interferometer provides a measurement for the line integrated density of the plasma. Figure 2.3 shows a schematic for the operating principle of the diagnostic. Laser emissions from a source is split into two paths. One path is directed from the source, through the plasma, and back out. The other path for the emission remains outside of the plasma before being combined with the emission from the other pathway. The refractive index of the plasma causes a phase delay between the two laser pathways which is used to calculate the density of the plasma.

The temperature of electrons can be obtained through the electron cyclotron emission (ECE) diagnostic. Electrons in the plasma can emit radiation as they gyrate around the magnetic field. The intensity of the emission is proportional to the temperature of the electron. The location of the emission is calculated through the frequency of the signal since the cyclotron

frequency depends on the magnetic field which monotonically decreases in a tokamak.

## 2.2 Fast ion diagnostics

Other diagnostics are needed to measure the fast ion population in order to understand the effects of energetic particle instabilities. While the distribution for thermal particles are generally considered to be Gaussian, the fast ion distribution is highly anisotropic which make it difficult to measure and interpret its effect. It is difficult to measure the entire phase space distribution so multiple diagnostics are typically employed in tandem to gain a better picture.

Many diagnostics have been developed to investigate different parts of phase space using different techniques. Some diagnostics like neutron or fast ion $D\alpha$ (FIDA) measurements effectively average over much of velocity space; these diagnostics are useful for general assessments of fast-ion behavior. Other diagnostics are localized in phase space; these are most useful for detailed assessment of physics mechanisms, such as the wave-particle interaction associated with a particular resonance.

The amount of fusion reactions can be measured by the number of neutrons emitted. For D-D reactions (1.2 and 1.3), there is a 50% chance that a neutron will be produced. For tokamak experiments (like DIII-D), neutrons emissions can come from fusion between bulk ions in the plasma (thermonuclear emissions) or between beam ions and the plasma (beam-plasma emissions). This distinction is necessary to properly assess the progress made towards developing a reactor. Since beam-plasma emissions originate from interactions with beam ions, the measured amount can be used as a 0D measurement of the fast ion distribution produced by the neutral beam. Neutrons are measured using scintillators that emit light when neutrons pass through them. A detector like a photomultiplier tube (PMT) records

the emissions over time to give a neutron rate measurement.

The neutral particle analyzer (NPA) measures the fast ions that were neutralized through charge exchange with injected neutrals. This diagnostic uses a small pinhole to measure a highly localized population in phase space. Accepted particles are ionized again and measured with a detector. The imaging neutral particle analyzer (INPA) is an upgraded version of the NPA that resolves the energy of the detected particle. This is done by allowing the reionized particle to gyrate around the local magnetic field and onto a scintillator plate. Higher energy particles have a larger gyroradius which illuminates a location further away from the stripping foil. A camera is used to record the strike location as the discharge evolves in time. Further discussion on the INPA is presented in Ch. 3.

The same fast neutral particles can also emit photons if the particles are in an excited state. The wavelength of these emitted photons would be Doppler shifted according to the particle energy and direction relative to the diagnostic line of sight. The FIDA diagnostic measures these emissions to provide a rough measurement of the fast ion density. Collection optics viewing different positions along the beam line provide a radial profile for the measurement. Further discussion on the FIDA diagnostic is presented in Sec. 2.4. Documentation of the data analysis GUI used at DIII-D is presented in Appx. A.

Fast ions have energies that are much greater than that of thermal ions. Because of this, particle orbits are affected more by the $\nabla B$ and curvature drift. This provides a pathway, for fast ions born in the plasma, to traverse outside of the last closed flux surface and hit the wall. These particles can be measured by the fast ion loss detector (FILD). Figure 2.5 shows a diagram of the operating principle of the FILD. Certain particle trajectories are selected using a pinhole. The local magnetic field causes the particle to gyrate onto a scintillating plate where the intensity of light emission corresponds to density of particles.
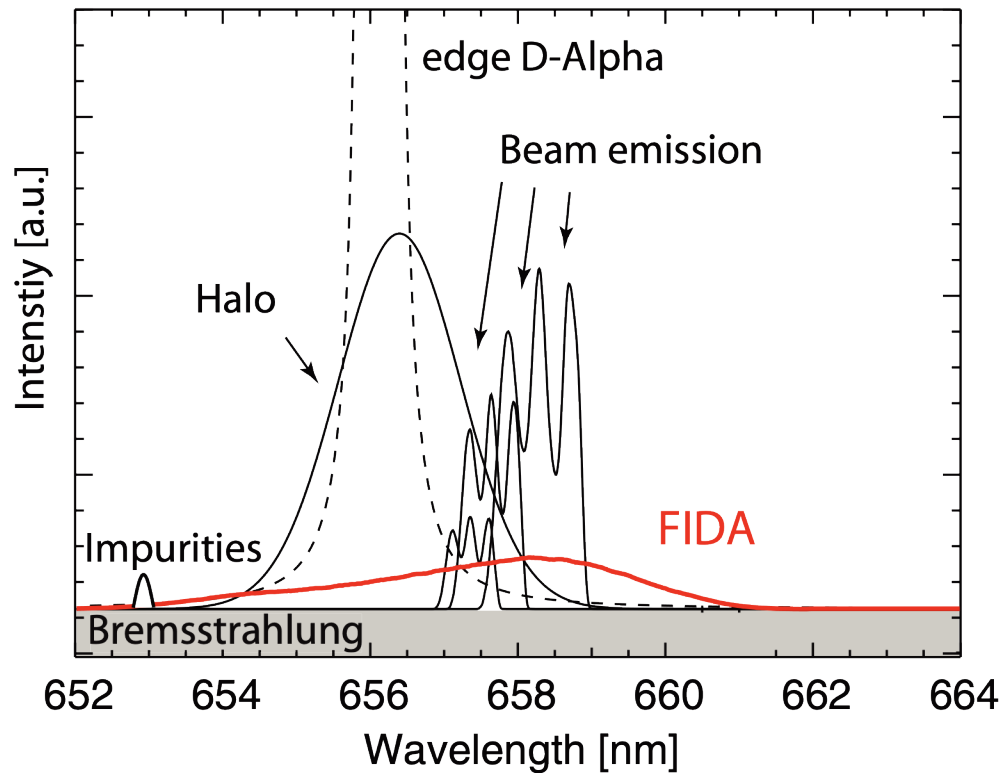
Figure 2.4: Example spectral components measured by the FIDA diagnostic. The FIDA signal (red) has a relatively low intensity but broad spectral range compared to the other spectral components. Figure taken from [6].
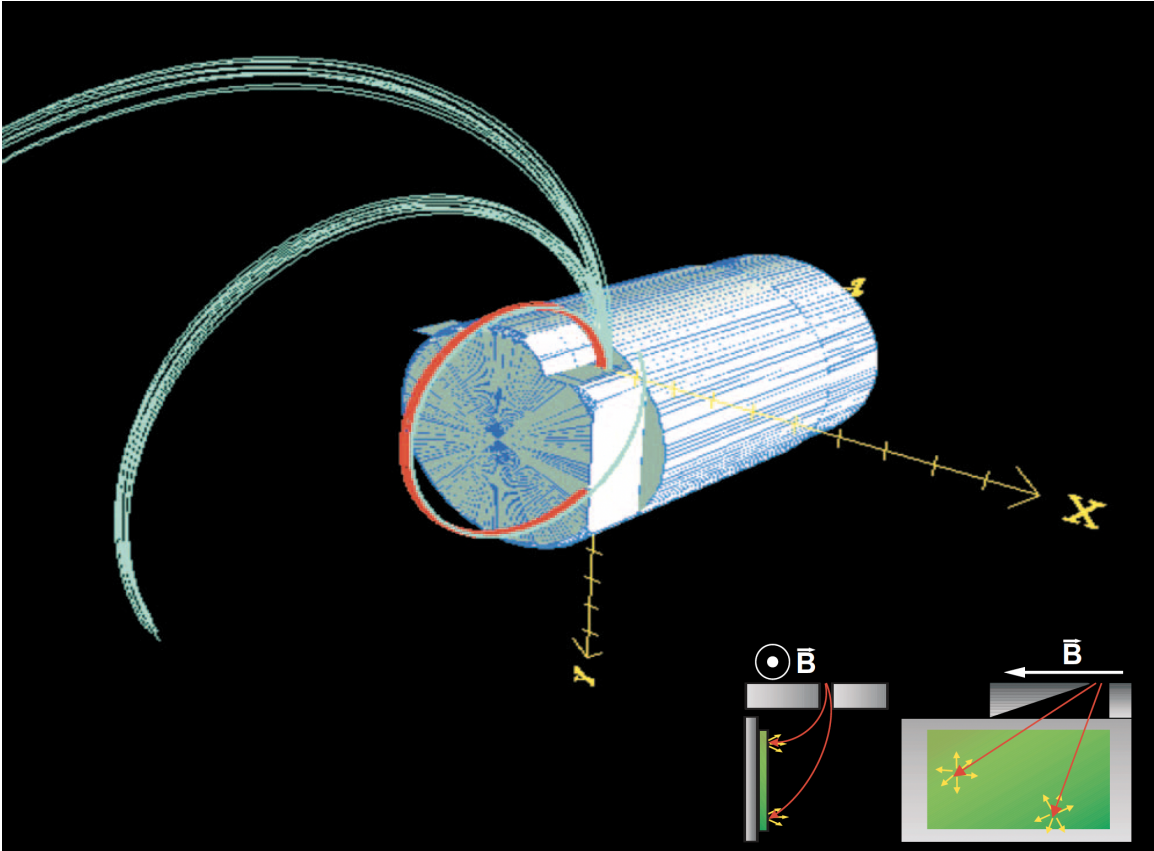
Figure 2.5: Operating principle of the FILD is shown. The diagnostic captures lost particles through a pinhole at the top of the device and uses the local magnetic field to guide the particle onto the scintillating plate. The strikepoint on the scintillating plate depends on the particle energy and gyroradius. Figure taken from [7].

## 2.3 Fluctuation diagnostics

Diagnosing perturbations in plasma requires more precise measurements since fluctuation values are only a fraction of the equilibrium value. Since the presence of plasma waves and instabilities may not be beneficial for plasma confinement, diagnostics are needed to detect and mitigate them if necessary. Measurements of neutron signals are one of the best ways to characterize fusion performance since they are only produced from fusion reactions. Instabilities that are deleterious to the plasma decrease the performance and reveal themselves through lower than expected neutron signals.

While neutrons may reveal the presence a wave or instability, they do not provide other useful characteristics. One way to extract more information is by looking at fluctuating quantities from the equilibrium medium. The linearization of plasma quantities motivates the separation into an equilibrium and fluctuation term. If the value of the signal is high enough compared to the noise, small fluctuation in the signals caused by plasma waves can be detected. Characteristics like the wave frequency and amplitude can be obtained by taking a fast Fourier transform (FFT) of signal. The measurement also needs to have sufficient temporal resolution to collect enough samples and accurately describe the form of the perturbation. Plasma waves and instabilities may only interact and affect certain quantities. Fluctuations in density, temperature, and magnetic fields are detected by the $CO_2$ interferometer, ECE radiometer, and magnetic probes respectively.

Fluctuations in the electrostatic potential can be indirectly diagnosed using the Doppler backscattering (DBS) diagnostic. The DBS diagnostic launches waves that refracts as it propagates through the plasma until it reaches a cutoff where it backscatters off turbulence. Different frequencies change the location of the cutoff, allowing for the construction of the electrostatic mode structure. The frequency of the Doppler shift is related to the $E \times B$ velocity caused by any electrostatic potential fluctuations. The diagnostic can also detect density
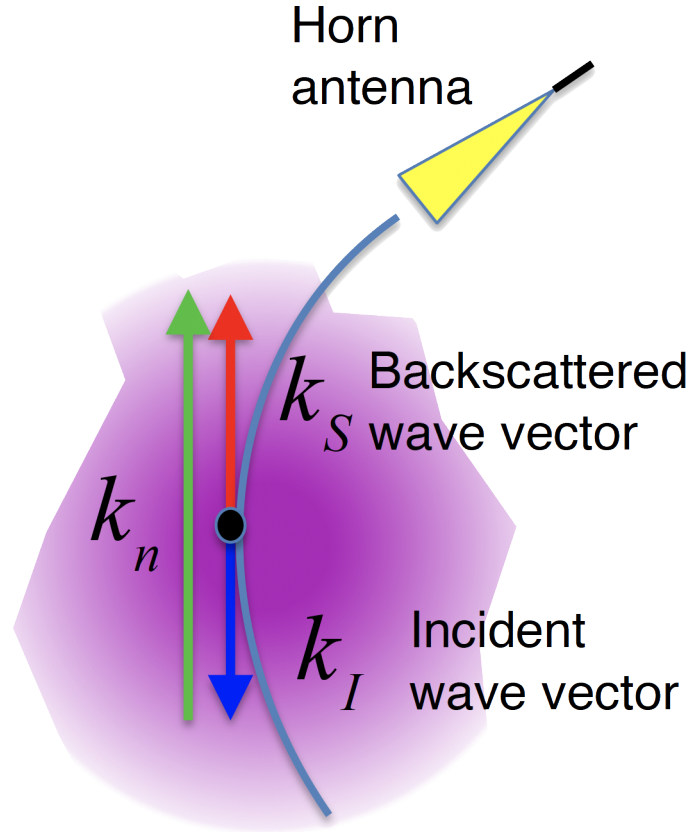
Figure 2.6: Operating schematic of the DBS diagnostic. Launched waves backscatter off a cutoff location and measures the perturbation wavenumber. Figure is provided courtesy of Lothar Schmitz.

fluctuations so care needs to be taken to accurately measure the electrostatic perturbation.

The beam emission spectroscopy (BES) diagnostic measures D-alpha emissions from beam neutrals. These emissions occur when beam neutrals that are born in an excited state collide with the background plasma causing D-alpha emissions. Collection optics organized in an array provide different spatial measurements depending on the setup.

## 2.4 Development of narrow stopband filter for FIDA measurements

The fast ion deuterium alpha (FIDA) diagnostic is commonly used to measure the fast ion population. The FIDA diagnostic is a spectroscopic diagnostic that measures the Doppler shifted Balmer-alpha (D-alpha for deuterium) emission that results from charge exchange reactions between fast ions and injected beam neutrals [18]. Measurement of this emission can be Doppler shifted if the neutral particle has significant energy and velocity components along the line of sight (LOS). At DIII-D, beam ions are typically injected at 80 keV resulting in maximum Doppler shifts around 650 and 662 nm for blue and red shifted emission respectively.

An important aspect for the operation of this diagnostic is the attenuation of the unshifted D-alpha emission around 656.1 nm. The emission originates from the n=3 to n=2 transition of deuterium atoms along the diagnostic LOS; this consists of signals produced from interactions with edge and wall neutrals as well as beam neutrals in the core of the plasma. Electron impact excitation of thermal neutrals and charge exchange between thermal ions and neutral particles provide the mechanisms that produces this emission. Since the thermal population makes up a larger fraction compared to the energetic ions, the resulting spectral component is also larger. This creates an issue where light collected from two spectrally close features differ by 3 or more orders of magnitude. A portion of the detector can easily saturate and bloom, due to the unshifted D-alpha emissions, making it difficult to achieve good signal to noise ratios at the Doppler shifted FIDA region.

There are a few ways to deal with the strong emission. One way is to simply avoid measuring the strong signals by tuning the system out of the wavelength range [19, 20]. One drawback is that only the red or blue shifted information would be measured, which means the other would be lost. To measure the full spectrum, the unshifted D-alpha emission needs to be
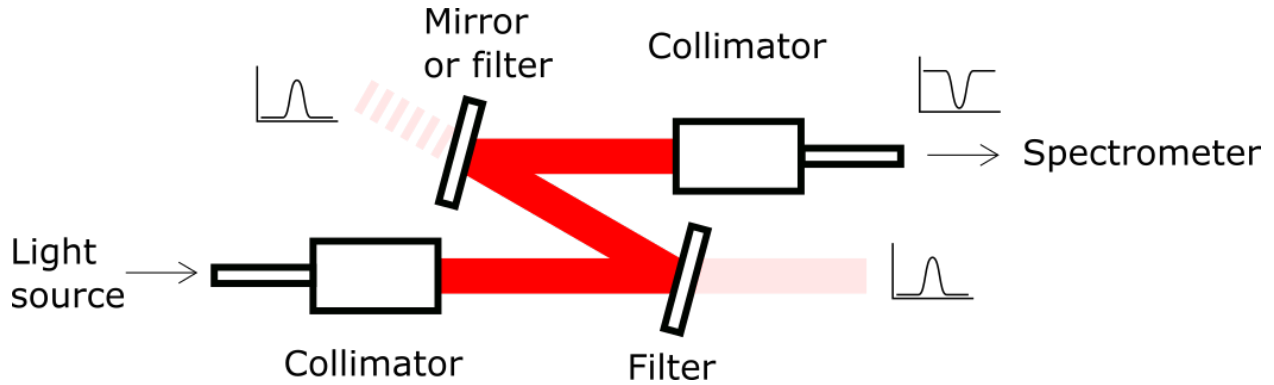
Figure 2.7: Optical layout to attenuate the D-alpha emission.

attenuated. This can be done using neutral density (ND) filter strips with an optical density (OD) of 2 that are placed at an intermediate focal plane of the dispersed image [18, 21]. Another method involves placing a narrow bar close to the detector in order to create a shadow that reduces the intensity of the strong signal [22].

While these methods work to prevent saturation and blooming on the detector, it does little to reduce the amount of scattered light which has been previously observed to contaminate the FIDA measurement [21]. This section describes a technique aimed towards reducing the intensity of the unshifted D-alpha region before it enters the spectrometer. To do this, the reflection off an ultra-narrow bandpass filter is utilized to obtain the desired blocking properties. Section 2.4.1 will describe the design of the optical layout and section 2.4.2 will show the results. Finally, section 2.4.3 provides a summary and discusses future works.

## 2.4.1   Design and Hardware

The goal of this design is to obtain an OD 2 blocking within a 1 nm FWHM region around 656.1 nm while maintaining high transmission (> 95%) outside of that range. A narrow stopband (notch) filter with these properties would be an obvious candidate. However, technological advances have not progressed far enough to the point where the blocking width and out-of-band transmission requirement can be satisfied; therefore, the reflection off an

ultra-narrowband filter is used. The optical setup is shown in figure 2.7. Light from a broadband LED source is transmitted through optical fibers and then collimated. The resulting collimated beam is then filtered using the reflection off one or two ultra-narrowband filters. The beam is then focused back into another fiber and transmitted to a spectrometer for measurement.

The 25.4 mm diameter and 2 mm thick (3.5 mm with the mount) filter used is designed and manufactured by Alluxa [23] to transmit a 1 nm region around 656.1 nm at an angle of incidence (AOI) of 15° while reflecting the rest of the spectra. The AOI is chosen to minimize the splitting between the $s$ and $p$ polarization of the incident light [24] and minimize the path length for light to travel. The transmission curve for the filter at a 0° AOI, supplied by the vendor, is shown as the black curve in figure 2.8. The filter provides $\sim 95\%$ maximum transmission in the passband region and $\sim 99\%$ reflection in the out of band region. Measurements for this figure are made using a dual monochromator design with a series of slits to narrow the angle of the light cone [25]. The wavelength affected by the filter varies with the AOI by the formula

$$\lambda_\theta = \lambda_0 \sqrt{1 - \left(\frac{n_0}{n_{eff}} \sin\theta\right)^2} \tag{2.3}$$

where $\lambda_0$ is the wavelength at 0° AOI, $n_0$ is the index of refraction of the incident medium, and $n_{eff}$ is the effective index of refraction for the filter. In general, $n_{eff}$ is larger than $n_0$ so $\lambda_\theta$ can only decrease with changes in incidence angles.

Testing of the filter performance is done using 200 $\mu$m and 400 $\mu$m core diameter fiber with a numerical aperture (NA) of 0.22. These are typical specifications for fibers used in many FIDA installations. Broadband light is provided by a Thorlabs MWWHF2 LED source which has a peak intensity at 600 nm. The intensity drops with increasing wavelength and 50% of the peak intensity resides around 650 nm. Identical collimators are used to collimate

26
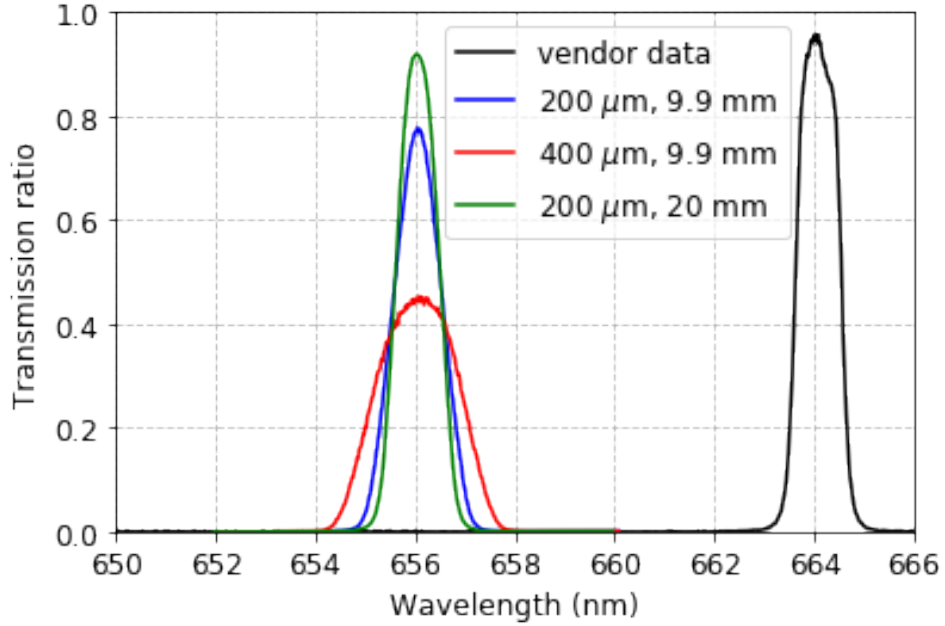
Figure 2.8: Transmission specifications of the filter at 0° AOI provided by the vendor is shown in black. The blue, red, and green curves are simulated signals, using different combinations of fibers and collimator focal lengths, at 15° AOI.

and focus the light. Two types of collimators are used in this study; one has a focal length of 9.9 mm and a clear aperture of 11 mm, while the other has a focal length of 20 mm and a clear aperture of 25 mm. The resulting collimated beam will have a divergence described by

$$\theta_d = \frac{D_m}{f} \tag{2.4}$$

where $D_m$ is the mode field diameter (MFD) of the fiber, which can be taken as the diameter where the the intensity drops to $1/e^2$, and $f$ is the focal length of the collimating element [26].

An Ocean Optics (now called Ocean Insight) HR4000 spectrometer is used to measure the spectra from 630 - 683 nm. The spectrometer input uses a 5 $\mu$m wide slit with an f/4, 101 mm focal length lens and data is collected over an integration period of 10 ms. The spectral sensitivity is peaked and slowly decreases away from 650 nm. The CCD collects

27
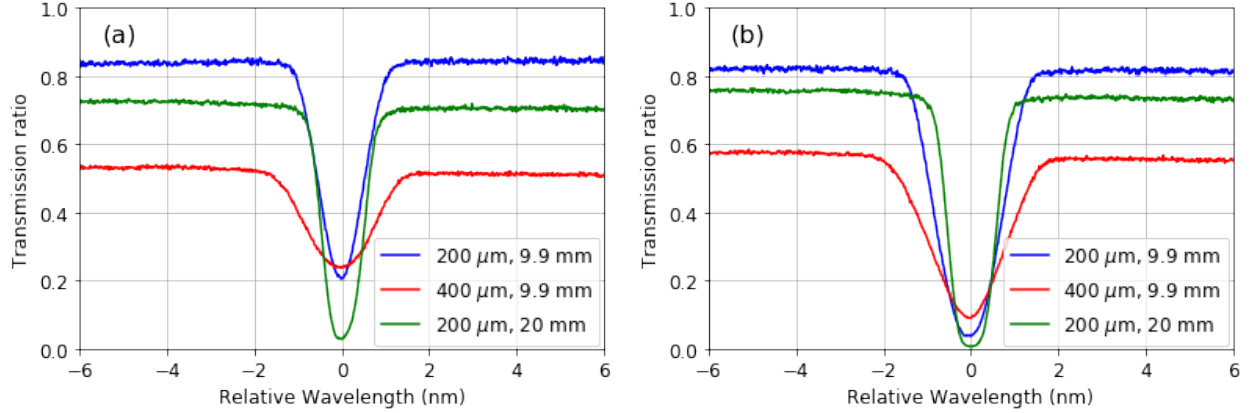
Figure 2.9: Transmission curves for different combinations of filters and collimator focal lengths are plotted against the wavelength relative to the maximum blocking wavelength. The (a) left figure contains measurements using 1 filter while the (b) right figure contains measurements using 2 filters.

$\sim 10^4$ photons per wavelength bin with SNR $\sim 100$. In this setup, the spectrometer has the highest f/number which constrains the measured light cone. This prevents full diagnosis of the light cone from the fibers with NA=0.22 (f/2.2).

## 2.4.2    Results

The transmission curves for different combinations of filters, fibers, and collimators are shown in figure 2.9. The values are obtained by normalizing the measured signal to a baseline measurement of the source using the corresponding fiber. The abscissa is given in wavelength relative to the location of maximum attenuation. The shape of the transmission profile differs from the inverse of the vendor supplied profile, shown in figure 2.8, because of the different beam divergence and AOI for each system.

The larger divergence in this study blurs fine features and produces a wider distribution of incidence angles for all wavelengths. This effect is simulated in figure 2.8 for 200 $\mu$m (blue) and 400 $\mu$m (red) fibers at 15° AOI. A simple Monte Carlo simulation with a uniform spread of angles (within the beam divergence) is used with eq. 2.3 and the vendor supplied data
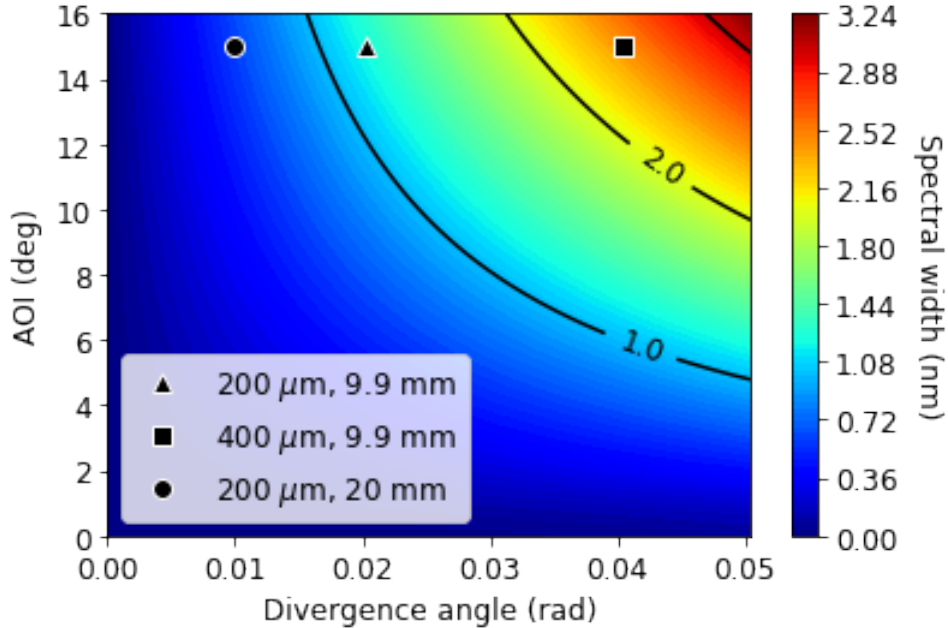
Figure 2.10: Calculated spectral widths for a single wavelength based off eq. 2.3 for various incident and divergence angles. The triangle, square, and circle markers indicate the combinations of angles probed in this study.

(as a look-up table) to produce the spectra. Larger divergences create more combinations (incident angles and wavelengths) that can satisfy the transmission requirement for the interference filter. The result is a more gradual slope near the boundaries that affects regions further away from the CWL (located around 656.1 nm). Increasing the AOI from $\theta_i = 0°$ to $\theta_i = 15°$ also widens the spectral feature. From eq. 2.3, the spectral width can be defined as $\Delta\lambda = \lambda_{\theta_i - \theta_d/2} - \lambda_{\theta_i + \theta_d/2}$ when $\theta_i \geq \theta_d/2$. Figure 2.10 shows the relationship where the increase in AOI or divergence angle causes the spectral width to increase. These effects do not impact the FIDA measurement region which starts at least 2 nm away from the CWL.

The performance of each configuration shown in figure 2.9 is summarized in table 2.1. Measurements indicate that each configuration reduces the transmission of the overall spectrum by different amounts. The 200 $\mu$m and 400 $\mu$m fibers using the 9.9 mm focal length collimators have transmissions around 83% and 55% respectively in the blue shifted FIDA range (around 650 - 654 nm). When using the 20 mm focal length collimator with the 200 $\mu$m

29

| Fiber Size ($\mu$m) | Focal (mm) | Divergence (rad) | # of Filters | CWL Transmission | Out-of-Band Transmission | FWHM (nm) |
|---|---|---|---|---|---|---|
| 200 | 9.9 | 0.0202 | 1 | 0.206 | 0.838 | 1.13 |
| 200 | 9.9 | 0.0202 | 2 | 0.037 | 0.821 | 1.66 |
| 400 | 9.9 | 0.0404 | 1 | 0.237 | 0.532 | 1.79 |
| 400 | 9.9 | 0.0404 | 2 | 0.090 | 0.576 | 1.92 |
| 200 | 20 | 0.0100 | 1 | 0.029 | 0.725 | 1.04 |
| 200 | 20 | 0.0100 | 2 | 0.006 | 0.756 | 1.16 |

Table 2.1: Filter performance for different configurations of fibers and collimators.

fiber, the out-of-band transmission is around 74%. Apart from the overall transmission loss, the different configurations affect the width and maximum attenuation at the CWL.

As expected, the addition of another filter decreases the minimum transmission at the CWL since the total attenuation is the product of the attenuations of each filter. Theoretically, squaring the minimum transmission for one filter should result in the minimum transmission for two filters. In practice, it is difficult to perfectly align both filters so that the maximum possible attenuation is achieved. Slight differences in the AOI between two filters result in small shifts in attenuated wavelength which reduces the maximum attenuation.

For the 9.9 mm focal length collimator, 200 $\mu$m fibers have lower minimum transmissions compared to the 400 $\mu$m fibers. Fibers with smaller core diameters will also have smaller MFD which, from eq. 2.4, will reduce the beam divergence of the collimated beam. The decreased divergence leads to a narrower distribution of incidence angles, on the filter, which results in a deeper and narrower blocking profile. The same effect takes place when comparing the measurements between the 9.9 mm and 20 mm focal length collimators for the 200 $\mu$m fibers. In this case, the divergence is decreased by increasing the focal length.

The coupling loss due to the beam divergence is also tested for the different configurations. In this test, light is transmitted from one collimator and subsequently collected by a second collimator; signals are obtained and normalized at various path lengths defined by the distance between the tips of the collimators. The average transmission between 651 - 653
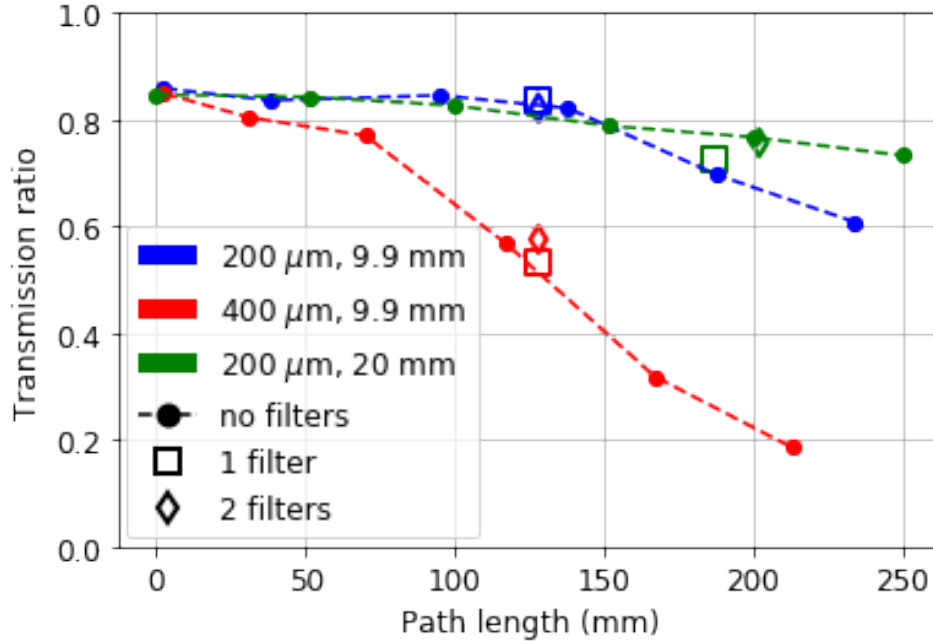
Figure 2.11: Average transmission of different combinations of fiber size and focal length is plotted for different total path lengths, defined by distance between the tips of the collimators. Transmission values for figure 2.9 are shown by the square and diamond markers.

nm is used as a measure for the performance. The measured transmission loss due to beam divergence is shown in figure 2.11 as a function of the path length. The blue dots connected by the dashed line correspond to measurements with 200 $\mu$m fibers (using 9.9 mm collimators) without using any filters while the red dots connected by the dashed line correspond to measurements with the 400 $\mu$m fiber (using 9.9 mm collimators) without using any filters. The measurements of the 200 $\mu$m fibers (using the 20 mm collimators) without any filters are represented by the green dots connected by dashed line. The configuration using the 400 $\mu$m fiber has the largest beam divergence in this study (0.0404 rad). This configuration contains losses that increase at a faster rate, with path length, compared to the other configurations. The configuration using the 20 mm collimator has the lowest divergence in this study (0.0100). This configuration contains the slowest loss rate with path length.

The averaged out-of-band transmission for each spectra shown in figure 2.9 is also plotted in figure 2.11. The square marker represents measurements that use one filter and the diamond

marker represents measurements that use two filters. The path length is around 125 mm for the configurations using the 9.9 mm collimator and around 190 mm for the configuration using the 20 mm collimator. The transmissions with the filters in place are consistent with the transmissions without the filters. This means that the losses observed are due to the divergence of the collimated beam and not from the filter.

## 2.4.3 Summary

A new technique to attenuate the unshifted D-alpha emission (656.1 nm) for the FIDA diagnostic has been developed. The reflection off an ultra-narrow bandpass filter is used to achieve a blocking FWHM of $1-2$ nm within the divergence range of $0.0100 - 0.0404$ rad. Using the two-filter configuration further decreases the transmission of the D-alpha region and a minimum of 0.006 was achieved for the lowest divergence angles (0.0100 rad). The overall transmission losses ($\sim26\%$, $\sim17\%$, and $\sim45\%$ for beam divergences of 0.0100 rad, 0.0202 rad, and 0.0404 rad) are attributed to coupling loss caused by the beam divergence and not the filter. The beam divergence is proportional to the fiber size and inversely proportional to collimator focal length. As the beam divergence decreases, both the filter and coupling efficiency increases. These results only characterize light limited by the f/4 optics from the spectrometer and more work is needed to characterize the full output from the fibers (f/2.2).

While the current results for this technique seem promising, further developments are needed to improve performance and compete with other available techniques. Available D-alpha blocking methods provide attenuations around OD 2 in the D-alpha range without causing further losses in the out-of-band regions. The maximum attenuation of the D-alpha signal and overall transmission of the technique in this section can be improved upon by reducing the divergence of the collimated beam. For a given fiber size, this can only be done by

increasing the focal length. To prevent overfilling of the optics, the size of the collimating element must also increase to have the same or smaller f/number. It is impractical to have large collimators for each fiber. Alternatively, this technique can be incorporated into the FIDA spectrometer design. Currently, light from multiple fibers are collimated through a large lens in the spectrometer input. It then passes through a bandpass filter (648 - 662 nm) and grism before it is transmitted out of the spectrometer. The path can be modified to utilize the reflection off the ultra-narrowband filter before it enters the grism. In addition to improving the performance, this will drastically drive down the potential cost for filtering each fiber individually ($\sim$ 2000 USD per filtered fiber for the prototype).

# Chapter 3

# Validation of the INPA on DIII-D

## 3.1 Introduction

This chapter will discuss the work in validating signals obtained from the INPA which has been recently developed on DIII-D [8, 27]. The design is based off traditional NPA diagnostics which have excellent velocity-space resolution because escaping neutrals have a well-defined velocity vector. NPA measurements of fast ions have been performed in tokamaks since the early days of fusion research [28]. The INPA (Fig. 3.1) combines three well-known elements to achieve a powerful new diagnostic technique. Escaping neutrals are produced when fast ions that traverse an injected neutral beam gain an electron in a charge-exchange reaction, as in a conventional active charge-exchange NPA diagnostic [29]. A carbon stripping foil converts neutrals into ions, as in a compact NPA [30]. The ions gyrate in the local magnetic field until they strike a scintillator plate and the emitted light is measured by a CCD camera, as in a fast-ion loss detector (FILD) [31, 32]. The resulting diagnostic measures more radial positions and energies than a conventional NPA, with superior signal-to-noise ratio [8, 27].
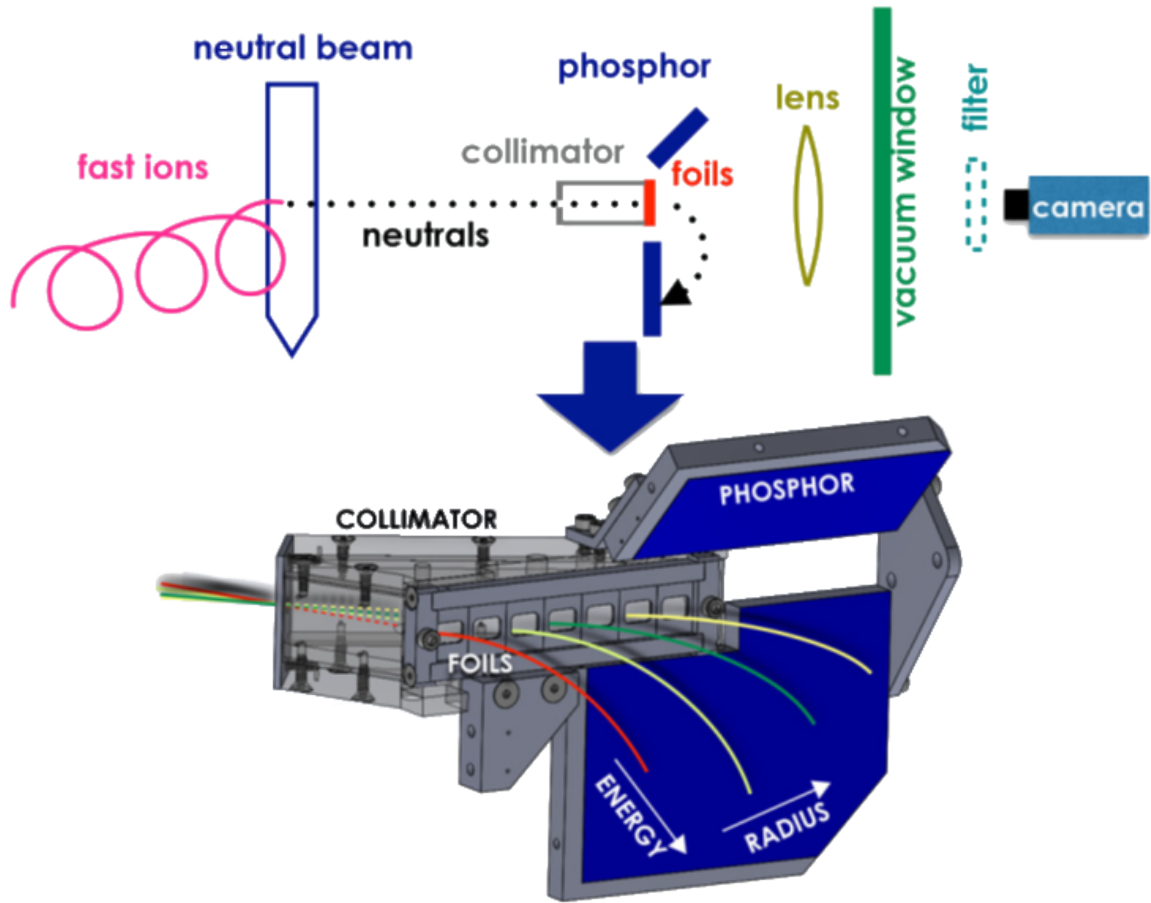
Figure 3.1: Diagram of the INPA diagnostic taken from [8]. The INPA measures fast neutrals from charge exchange reactions between fast ions and beam neutrals. Detected neutrals pass through the pinhole and are ionized by the carbon stripping foil. Local magnetic fields bend cause the ions to gyrate onto the phosphor plate. Light emitted from the phosphor is captured by a camera.

Because the INPA is a new diagnostic technique, it is important to verify its performance. Several qualitative tests have already been reported [8, 27]. The full, half, and third energy components of the injected neutrals are resolved with ∼ 7.5 keV energy resolution [27]. The measured image varies as expected with magnetic field [8, 27]. The time evolution of the signal in response to short beam pulses shows the expected behavior, including the dependence on beam geometry [8]. Sawteeth cause redistribution of passing fast ions, as expected [8, 27]. An initial simulation of the signal resembles the measurement [8].

The purpose of the present work is to provide quantitative validation of the INPA measurements. To provide a known distribution function, dedicated discharges with low levels of MHD were created on DIII-D and the plasma parameters were systematically varied to alter the distribution function. In the absence of instabilities, the evolution of the beam ion distribution function $f$ in a uniform Maxwellian background plasma is described by the Fokker-Planck equation, $\partial f/\partial t = S + C$, where $S$ represents sources and sinks, and the collision operator $C$ is [33],

$$
\begin{aligned}
C(v,\zeta,t) =& \frac{1}{\tau_{se}} v \left[ \left( v^3 + v_c^3 \right) f(v,\zeta,t) \right] + \\
& \frac{1}{2\tau_{se}} v \left[ \frac{v_e^2 m_e}{m_f} + \frac{v_c v_i^2 m_i}{v^3 m_f} \right] f v(v,\zeta,t) + \\
& \frac{1}{2\tau_{se}} \frac{m_i}{m_f} \frac{Z_{eff}}{[Z]} \frac{v_c^3}{v^3} \zeta \left[ \left( 1 - \zeta^2 \right) f \zeta(v,\zeta,t) \right]
\end{aligned}
\tag{3.1}
$$

Here, $\zeta = v_\parallel/v$ is the pitch relative to the magnetic field, $\tau_{se}$ is the Spitzer slowing down time on electrons, and $v_c$ is the critical speed where the drag on the background species of electrons and ions are equal. The first term in Eq. 3.1 represents drag on the fast ions by the background plasma. The last two terms describe the diffusion in energy and scattering in pitch, respectively.

Because NPA signals essentially measure a single pitch $\zeta$, they are very sensitive to the third term in Eq. 3.1, the pitch-angle scattering term. Many previous studies have used conventional NPAs to explore this dependence [28]. In particular, a DIII-D experiment that compared measured NPA signals with signals predicted by the TRANSP NUBEAM [34] code in MHD-quiescent plasmas reported excellent quantitative agreement with the expected dependence on the pitch-angle scattering rate $\nu_{PAS}$ [35, 36]. Accordingly, the dependence of the INPA signals on $\nu_{PAS}$ is explored in the present experiment. One approach is to vary the injection angle, which varies the initial pitch $\zeta_0$ relative to the value of $\zeta$ measured by the INPA. The second approach is to vary the electron temperature $T_e$ in order to vary the

critical speed $v_c$; since fast ions only pitch-angle scatter when they slow down on thermal ions (not electrons), changes in $T_e$ alter the expected signal. Another strong expected dependence of the INPA signal is on the electron density $n_e$: Increased density reduces the number of injected neutrals through increased attenuation, reduces the number of confined fast ions by shortening the slowing-down time, and reduces the number of escaping neutrals that escape the plasma without reionizing. The dependencies of INPA signals on $\zeta_0$, $T_e$, and $n_e$ are explored in the present work by reproducing different experimental conditions with simulations.
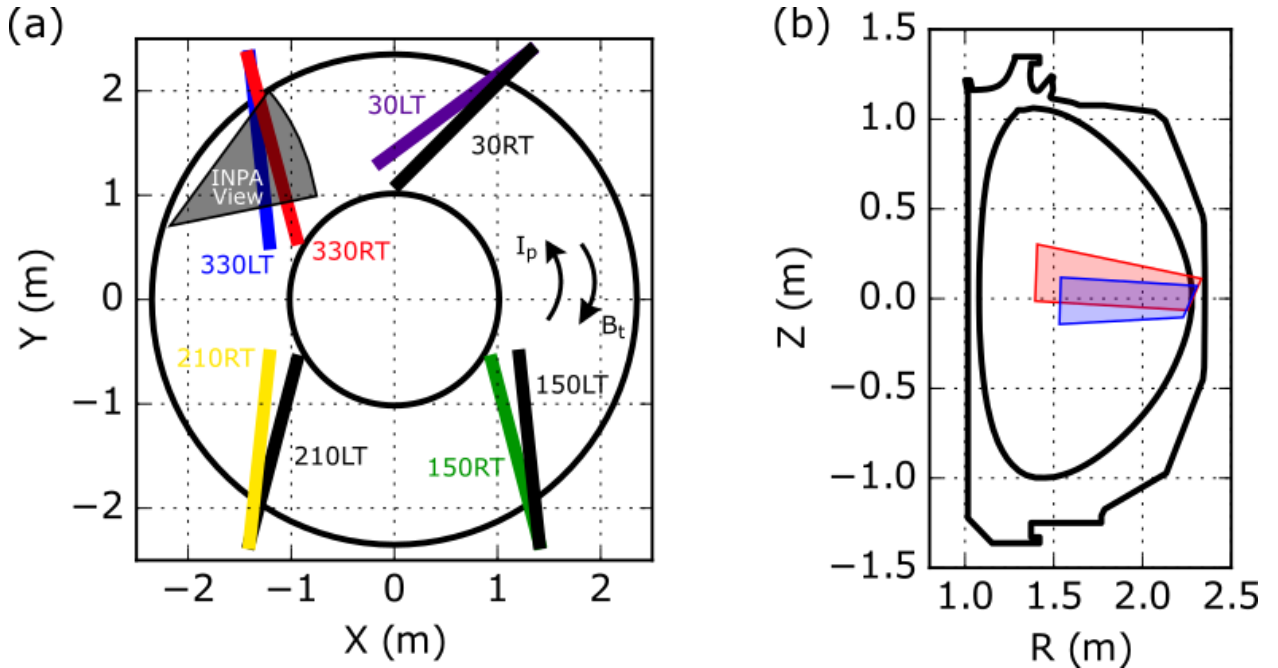


Figure 3.2: (a) The top down view of the DIII-D tokamak is shown with the different neutral beams. There are 6 beams (30LT/RT, 150 LT/RT, 330LT/RT) that inject in the co-current direction and 2 beams (210RT/LT) that inject in the counter-current direction (on-axis at the time of the experiment). The sightline for the INPA (shaded region) intersects the 330LT/RT beams. (b) The cross section of the device is plotted with an outline of the plasma boundary. The intersection of the diagnostic sighline with the vertical beam plane is overlaid. The blue and red regions correspond to the intersection with the 330LT and 330RT beam respectively.

Several different neutral populations can charge exchange with a fast ion to create a measured fast neutral. The sightlines of the INPA, shown in figure 3.2, are designed to intersect

37

with both 330LT and 330RT co-injecting beams near the midplane. This allows for different sensitivities in phase space, depending on which diagnostic beam is used. Aside from probing fast ions at different locations, the two beams probe at slightly different pitches. The 330LT beam, which injects at a more tangential direction, allows the INPA to detect pitches centered around $\zeta \sim 0.77$. The 330RT, which beam injects at a more perpendicular direction, allows the INPA to measure pitches centered around $\zeta \sim 0.79$. Signals produced by reactions with either the 330LT or 330RT beams are termed "active" signals. "Passive" signals are produced by charge-exchange reactions with cold edge neutrals. A previous study [37] distinguished between three different fast-ion populations that produce passive signals. One population is the axisymmetric population of confined fast ions that orbits in the edge region. This fast-ion population is included in the distribution function calculated by TRANSP NUBEAM. Another population that can be important in their first pass orbit was dubbed the "asymmetric" source in Ref. [37]. In this case, ionization of neutrals from a particular beam produces fast ions that traverse the diagnostic sightline near the edge or scrape off layer (SOL) region on their first full orbit. Part of the asymmetric population is made up of promptly lost particles while the other part equilibrates with the confined fast ion distribution through scattering processes. While both of these types of passive INPA signals are considered in the present study, the asymmetric source will be examined qualitatively. The third type of fast ion discussed in [37], fast ions expelled to the edge by instabilities, is unimportant in the present work.

In this study, the operation of the INPA is validated during classical conditions. Experimental images are compared to synthetic images that account for both active and passive contributions. The experiment to validate the operation and images produced by the INPA is described in section 3.2. The codes used to simulate and recreate the images are discussed in section 3.3. Section 3.4 compares the modelled images to the experiment.

## 3.2 Experimental Setup

The experiment is performed on the DIII-D tokamak which has a major radius of $R = 1.67$ m and a minor radius of $a = 0.67$ m. The signal from the INPA is tested by altering the fast ion distribution function during an MHD-quiescent classical discharge. To do this, the pitch-angle scattering rate $\nu_{PAS}$ is modified by varying the electron temperature $T_e$, through electron cyclotron heating (ECH), and the electron density $n_e$. The electron temperature and density ranged from $2 - 4$ keV and $3 \times 10^{19} - 5 \times 10^{19}$ $m^{-3}$ respectively at the core.

Figure 3.3 shows the time traces for two discharges (175242 and 175244). While an MHD-quiescent plasma was the target, a sawtooth instability was observed with a $q = 1$ surface around $R = 1.9$ m. Care is taken to select times with the least amount of sawtooth crashes for each ECH step. Lower signal levels are produced at later time, as the plasma density steadily increased. Time slices are averaged over a period of 80 ms to reduce noise and mitigate the impact of the sawtooth instability, which as shown in Refs [8, 27], can cause significant fast ion transport in the region of phase space probed by the INPA.
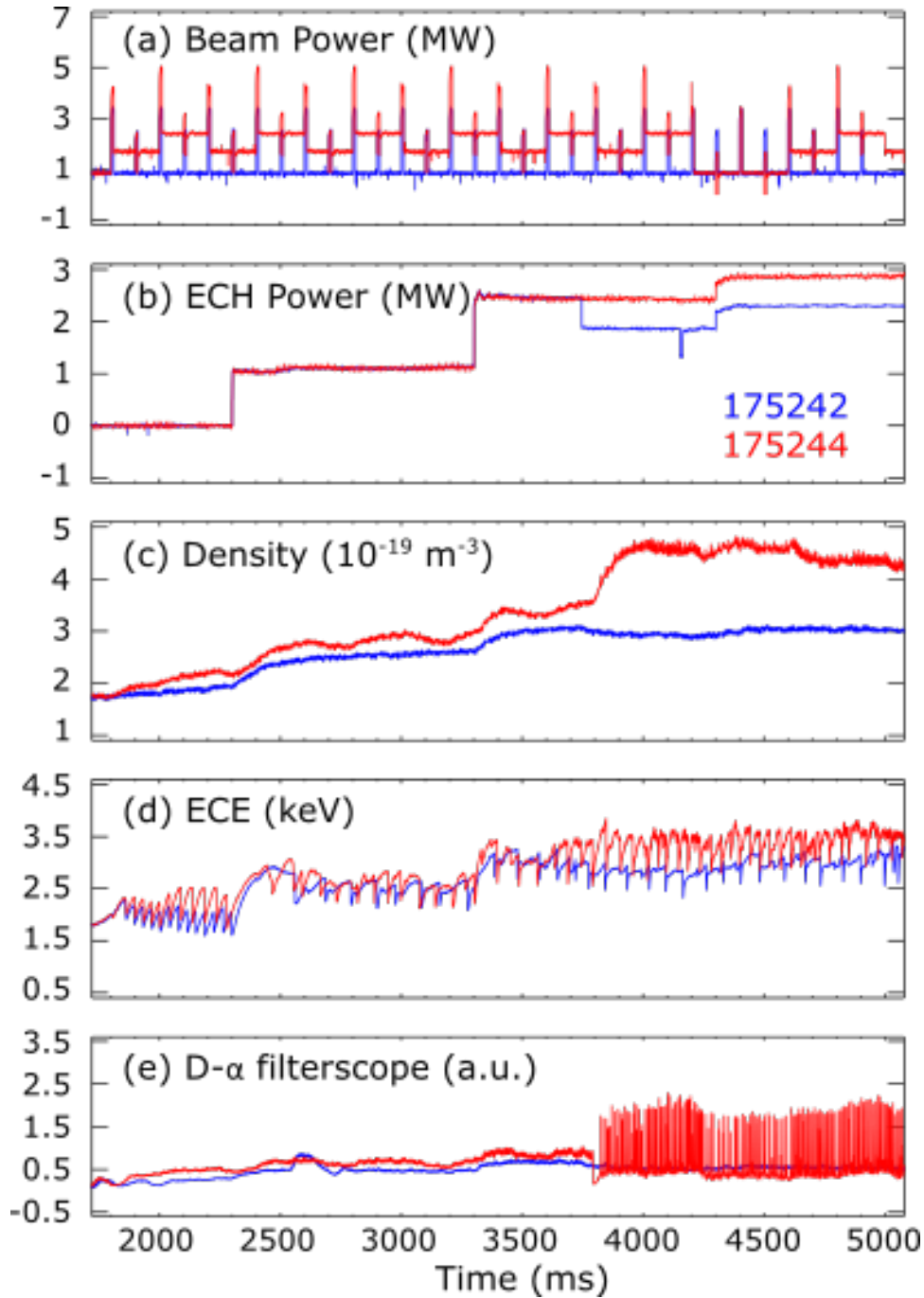
Figure 3.3: Time traces are shown for shot 175242 (blue) and 175244 (red). (a) The total beam power is mostly periodic for the duration of both discharges. (b) ECH power is increased in steps throughout both discharges. (c) The line integrated density near the core steadily increases. The density for shot 175244 sharply increases around 3800 ms which corresponds to a transition into H-mode. (d) The core electron temperature shows mild sawtooth activity for both cases. Activity increases for shot 175244 when it enters H-mode. (e) D-$\alpha$ measurements for shot 175244 show the appearance of edge localized modes (ELMs) as the plasma transitions into H-mode around 3800 ms.

The plasma equilibrium is calculated through equilibrium code EFIT [38] using data collected by magnetic probes and the motional stark effect diagnostic [39]. The current flattop portion of the discharge is set at a constant current of $I_p = 0.8$ MA and a constant field of $B_T = -2.05$ T.

Various plasma profiles, shown in figure 3.4, are obtained through a variety of diagnostics. The electron temperature is measured with Thomson scattering [40] and the electron cyclotron emission radiometer [41]. The electron density is measured by Thomson scattering [40] and the profile reflectometer [42]. The carbon impurity temperature, density, and rotation are all measured by charge exchange recombination spectroscopy [43]. Zeff is not measured directly but is derived through quasi-neutrality using the density profiles [44].
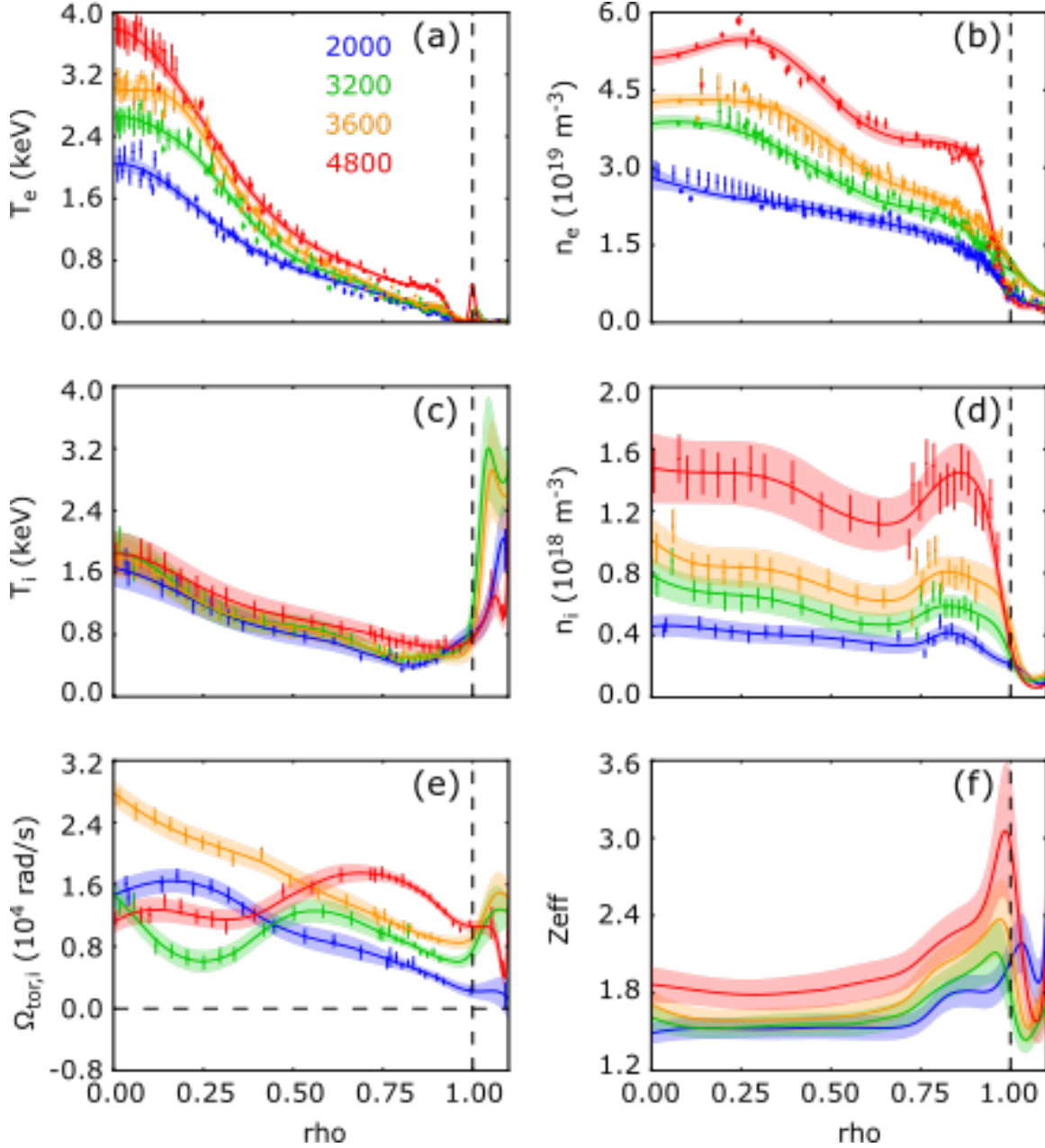
Figure 3.4: Profiles for the (a) electron temperature and (b) density, (c) carbon impurity temperature, (d) density, and (e) rotation, and (f) effective charge of the plasma are plotted against the normalized toroidal flux values (rho). The different colors represent different time ranges, from shot 175244, averaged over 80 ms. Blue, green, orange, and red corresponds to 2120-2000 ms, 3120-3200 ms, 3520-3600 ms, and 4720-4800 ms respectively. The measured data points are shown in addition to the best fit curves (with uncertainties indicated by the shaded region). Zeff is the only measurement that is not measured directly so there are no associated data points. The electron temperature, electron density, and carbon impurity density rise as the ECH power increases during the discharge.

The two shots have different beam patterns shown in figure 3.5. The first shot (175242) has the co-injecting 330LT beam on, at 50 keV for the whole duration of the phase, as the source for the fast ion distribution. Two other beams (the 30LT at 82 keV and the 150RT at 78 keV) alternate with 10 ms pulses every 100 ms for diagnostic purposes. Electron cyclotron heating (ECH) power is increased in steps to raise the electron temperature.
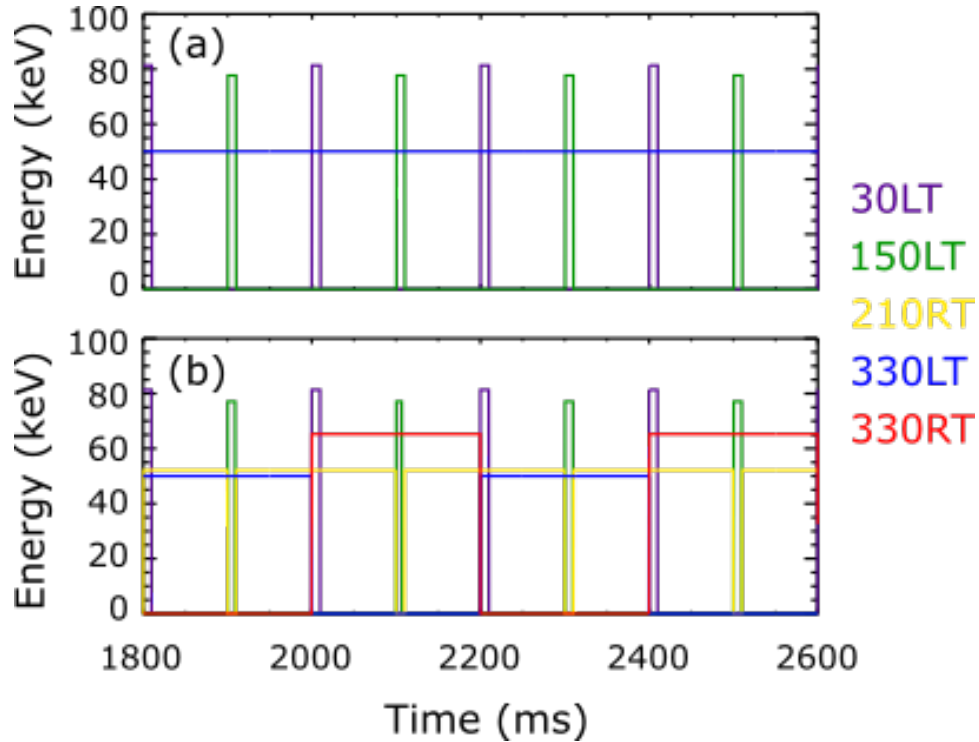


Figure 3.5: Beam patterns for discharge (a) 175242 and (b) 175244 are shown for two full cycles. (a) Shot 175242 contains 3 beams. The 330LT (blue) beam injects at 50 keV for the duration of the discharge while the 30LT (purple) beam at 82 keV and 150RT (green) beam at 78 keV blip for 10 ms alternating every 100 ms. (b) Shot 175244 contains 5 beams. The 30LT (purple) and 150RT (green) beams have the same timing and voltage from the previous shot. The 330LT (blue) beam at 50 keV now alternates with the 330RT (red) beam at 65 keV every 200 ms. The 210RT (yellow) beam is mostly constant at 52 keV except for 10 ms drops every 200 ms.

The second shot (175244) has a similar beam pattern from the previous shot but interleaves the co-injected 330RT beam at 65 keV with the 330LT beam. The beams alternate every 200 ms allowing for signal comparisons from both beams. In addition, the counter-injecting 210RT beam is on at 52 keV and turns off for 10 ms every 200 ms. This provides an active

43

beam for other fast ion diagnostics like FIDA. The 210RT beam is also known to create a strong passive signal seen in a small region on the image by the INPA which will be analyzed in section 3.4.2. ECH power was injected in the same way from the previous shot but performed more reliably without power drops.

## 3.3 Simulation

To simulate the signals seen by the INPA, the fast ion distribution is first calculated within the NUBEAM [34] module in TRANSP. TRANSP takes the experimental plasma profiles and models the deposition from the different heating sources into the plasma. NUBEAM keeps track of the fast ion distribution function and how it evolves through plasma collisions and atomic processes. The FRANTIC model [45] in TRANSP, which simulates the 1D transport of neutrals inside the separatrix as a function of minor radius, is used to produce the neutral density profile. Possible 3D effects of neutral profiles are neglected in this study. The process of fitting profiles and running TRANSP was performed in the OMFIT framework [46].

Once the fast ion distribution function is obtained, FIDASIM [47, 48] is able to determine the neutral flux to the INPA. FIDASIM simulates the injection of neutrals from the diagnostic beam and calculates the charge exchange reaction with the fast ion distribution. Developments in the code also allows for the calculation of neutral fluxes produced by charge exchange with edge neutrals. The diagnostic sightline is modelled to determine whether a fast neutral can make it to the detector.

The neutral flux from FIDASIM is then used in INPASIM [8, 49] to reproduce the camera image. First, the code calculates the interaction between the incident neutral flux and stripping foils. Then it traces the trajectory of particles from the stripping foil to the phosphor plate. The intensity of the light emission is assumed as a linear dependence on

incident energy. The transport of photons in the phosphor and resolution of the camera image are best fitted to a 2D Gaussian distribution. This code is also used to generate a grid corresponding to the energy and radial position of particles originating from the probing beam.

## 3.4 Results

Neutron rates are measured and compared to TRANSP simulations, shown in figure 3.6. A ratio of simulated and measured neutrons around 1.0 indicates agreement with the classical simulation. Similarly, the FIDA profiles measured from the experiment are also compared to the FIDASIM profiles in figure 3.7. Both the neutron rate and FIDA profiles agree with their simulated counterparts indicating that a classical fast ion distribution is present and the effect of MHD activity is minimal.
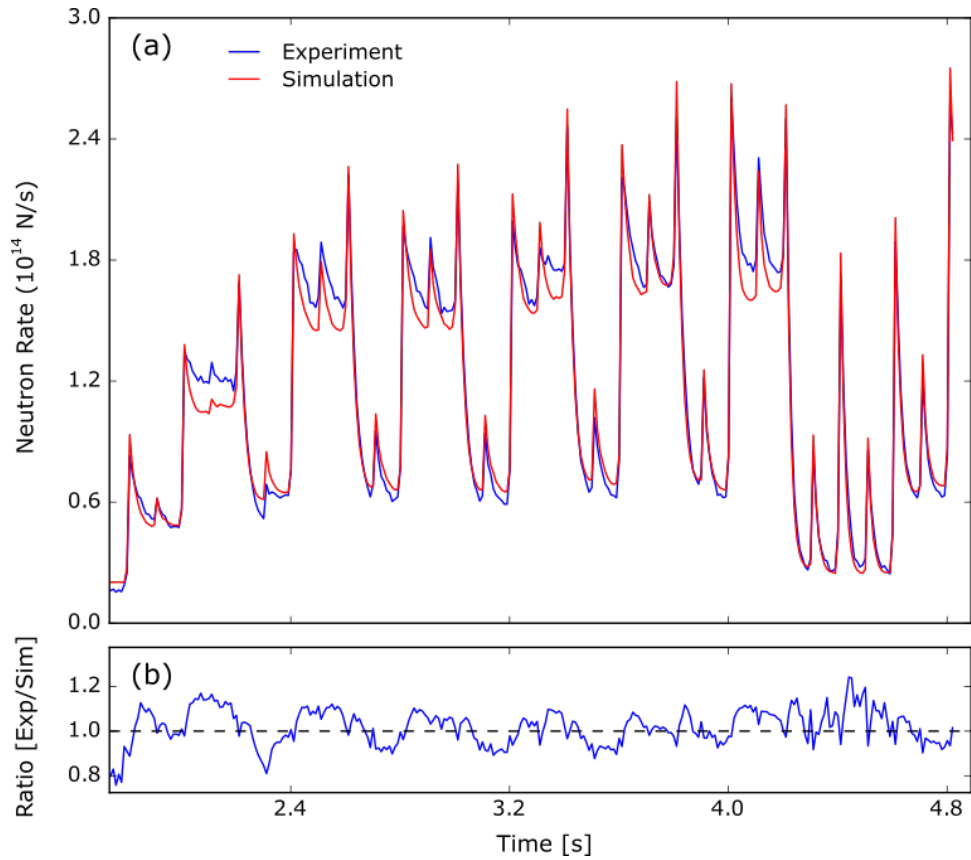
Figure 3.6: (a) The measured neutron rate is compared with the simulated rate from TRANSP for shot 175244. (b) The ratio of the experimental and simulated rates fluctuate around 1.0 indicating relatively good agreement.
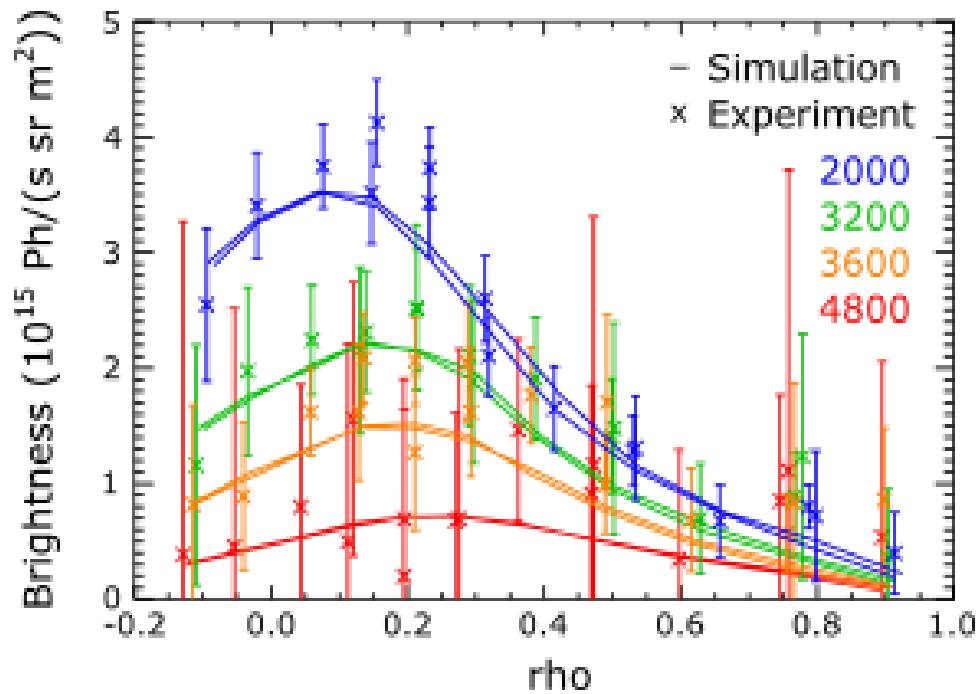
Figure 3.7: Experimental FIDA profiles compared to simulated profiles from FIDASIM at different times. There are two sets of chords spanning across the plasma that have nearly identical normalized flux (rho) values but are slightly displaced toroidally. The density rises at later time leading to lower signal levels and signal to noise ratios.

Fourteen 80 ms time periods are selected for analysis from the two shots. In the first shot, 6 different times with different ECH powers are selected, using 330LT as the active beam. In the second shot, 4 different times are selected for the 330LT beam.

### 3.4.1 Experimental comparison

To compare the experiment with simulation, images are first mapped onto radius and energy coordinates that are defined by the sightline intersection with the diagnostic beam. Next, the synthetic images need to be scaled to match the uncalibrated experimental images. To do this, the active and passive synthetic images are assumed to be a linear combination of the experimental image. An example of each synthetic component is shown in figure 3.8(a) and 3.8(b). The coefficient to the active component corresponds to an effective calibration factor and should not change between cases. For this reason, the active coefficient is set to a constant value which is an average from fitting all the cases. The passive signals are derived from charge exchange with edge neutrals which are calculated by TRANSP. The edge neutral profile is assumed to have the correct shape but not necessarily the correct magnitude, so this coefficient is allowed to vary between cases to obtain the best fit. The active and passive coefficients found by the INPA are checked for one case using the FIDA diagnostic. Figure 3.9 shows good agreement between the experimental and simulated FIDA spectra. Simulated and experimental INPA images are shown in figure 3.8(c) and 3.8(d) respectively.
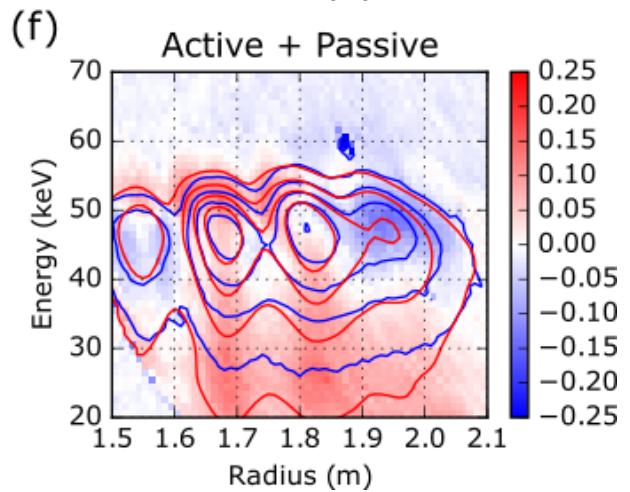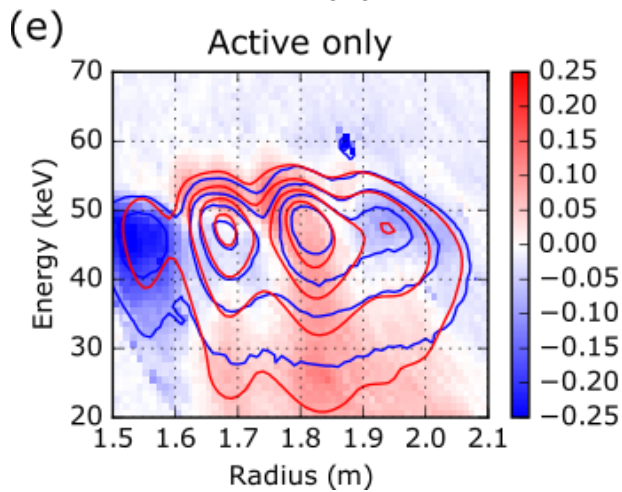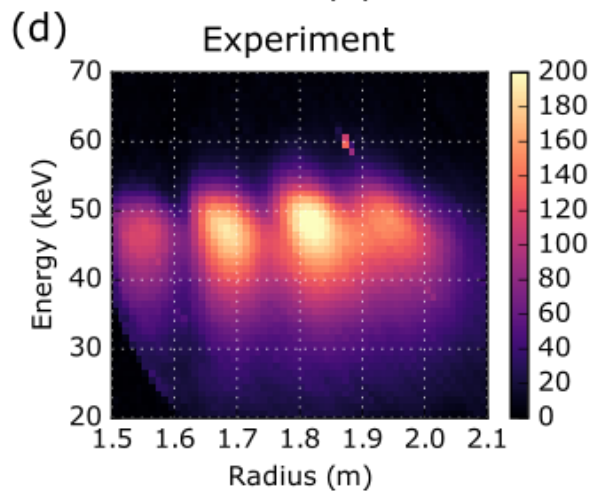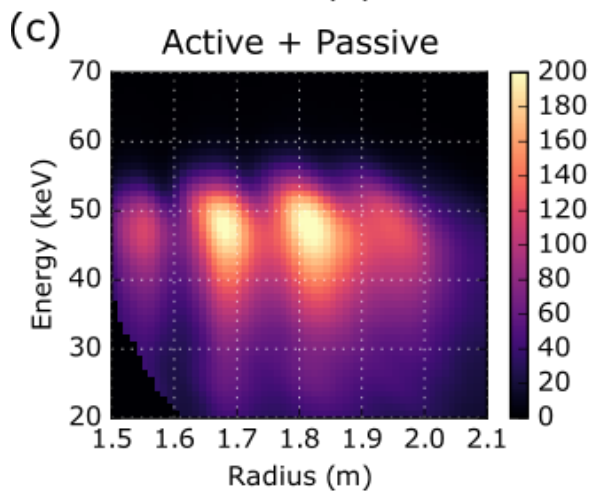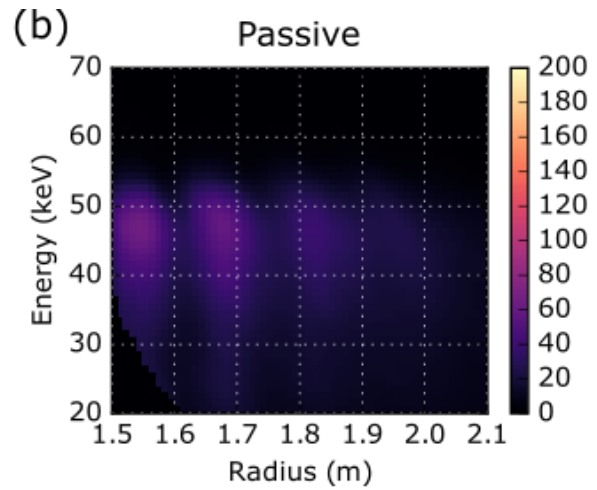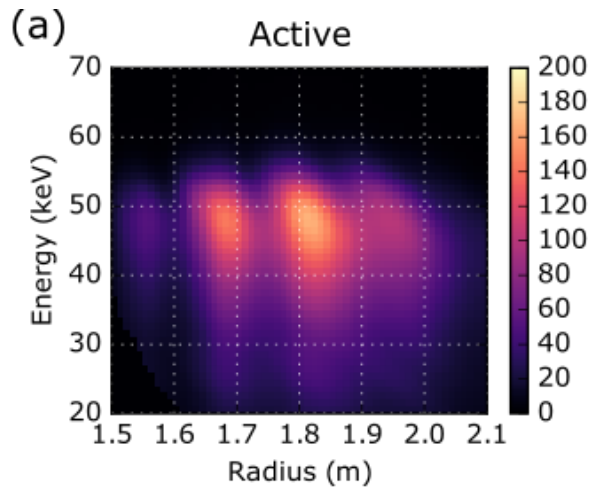
Figure 3.8: An image averaged from 2120 - 2200 ms for shot 175242 is analyzed. Synthetic images for the (a) active and (b) passive components are scaled with coefficients so the (c) sum of the simulated images match the (d) experimental image. The radial coordinate corresponds to the line of sight intersection with the centerline of the 330LT beam. Note that the dips in signal along the radial coordinate correspond to the support structures for the stripping foil blocking particles. The fractional signal difference between experiment and simulation are compared (e) without and (f) with the passive component. Red shading indicates that the region contains higher simulation values while blue shading indicates the region contains higher experimental values. The simulated image contours are plotted as red contour lines while the experimental image contours are plotted as blue contour lines. Incorrect assumption of linear dependence between light emission and particle energy is most likely the cause of the discrepancy at lower energies. The addition of passive signals resolve the feature between $R = 1.5 - 1.6$ m.
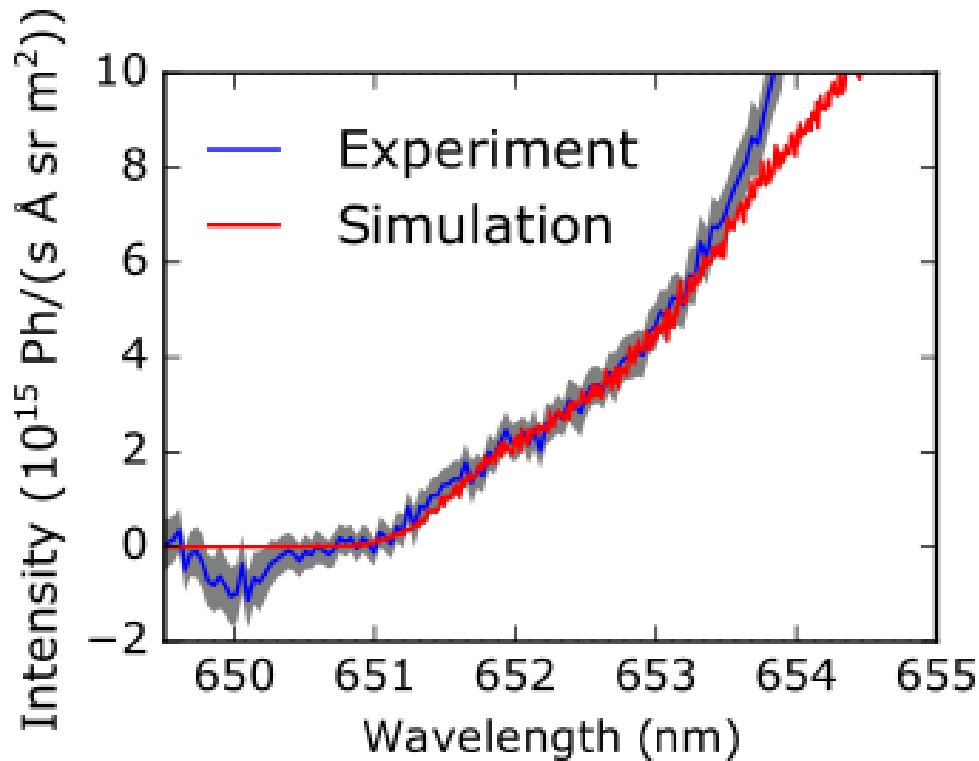


Figure 3.9: Background subtracted FIDA spectra (blue) is compared to the simulated FIDA spectra (red) calculated by FIDASIM. The error band (grey) for the experimental spectra is determined by the standard deviation of the time averaged spectra over 80 ms. The simulated spectra consists of the active and passive components with the ratio obtained by the INPA data. The slight dip centered around 650 nm corresponds to improper subtraction of the oxygen emission line. The experiment seems to agree well until around 653.5 nm, which corresponds to an energy of $\sim$ 15 keV. The red-shifted part of the FIDA spectra is known to have issues and has been omitted.

The features of the experimental images are compared to that of the synthetic images (without and with the inclusion of passive signals) in figure 3.8(e) and 3.8(f). This is done by taking the difference of the synthetic and experimental images and normalizing the result with the maximum value predicted in the simulation. The image without the passive signal shows a large deficit near R = 1.55 m. On the other hand, that deficit appears to be resolved with the addition of passive signals. This can be easily seen in figure 3.10 where a slice of the image is taken at $E = 47$ keV. In both cases, the simulated images differ from the experiment at certain areas. One area, that lies around $R = 1.9$ m, is most likely caused by the presence of the sawtooth instability that was not accounted for in the simulation. The mismatch centers around the $q = 1$ surface where redistribution would occur.
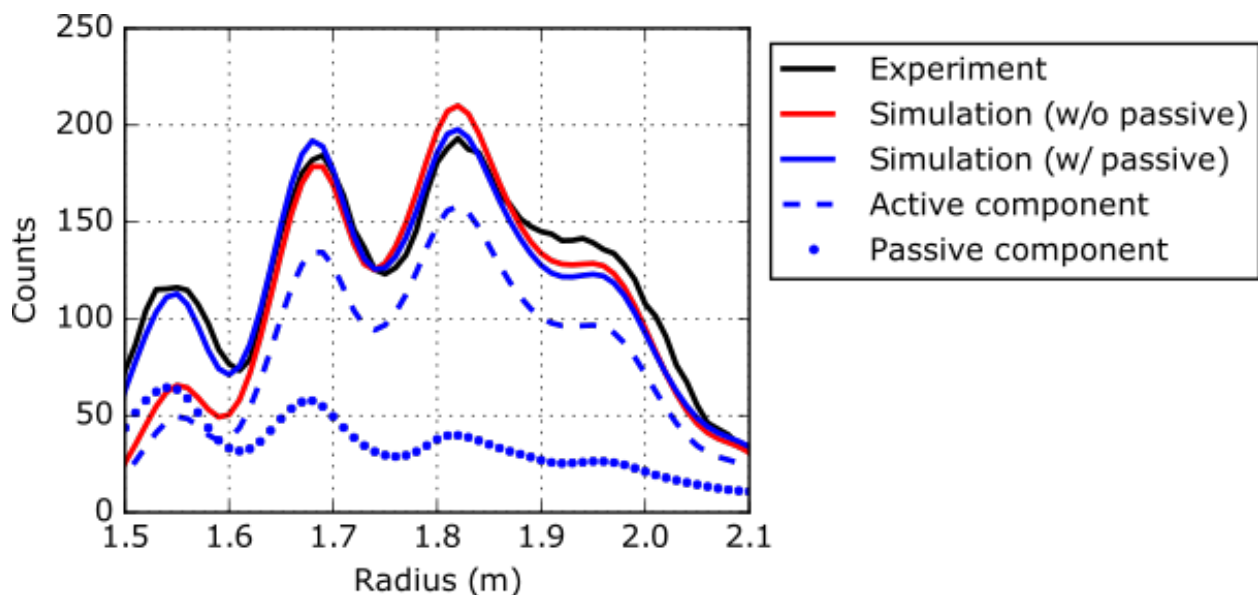


Figure 3.10: Slices of the image from figure 3.8 at $E = 47$ keV are plotted together. The black line is the signal observed from the experiment. The blue and red lines are the simulated signals that do and do not include the passive signals respectively. The active and passive components that make up the blue line are plotted in dashed and dotted lines. The dips in the plots are caused by the support structure blocking the neutral particles.

Another difference appears at lower energies where the simulated images predict more signal. Experimental comparisons with INPASIM images show differences that extend as far as $\sim 40$ keV. The linear dependence between the particle energy and intensity of light emitted

is most likely the cause for the overestimation in phosphor response since the relationship was merely chosen for simplicity. Looking back at figure 3.9, the spectra obtained from FIDASIM calculations start to deviate from the experiment near Doppler shifted energies of $\sim 15$ keV. This means FIDASIM is not the cause for the discrepancy at lower energies. Another possible cause of the discrepancy is an underestimation of charge-exchange losses in the TRANSP simulation, as strong charge exchange losses reduces the number of low-energy fast ions. This is explored in figure 3.11 by looking at a radial slice of the image at $R = 1.8$ m and comparing the experimental profile with multiple simulations using different neutral density values. The simulated result that uses 6.5 times the original neutral density seems to match the experimental profile the most, but it still overestimates the signal at lower energies. Results using higher neutral densities past that point seem to over-correct the charge exchange losses.
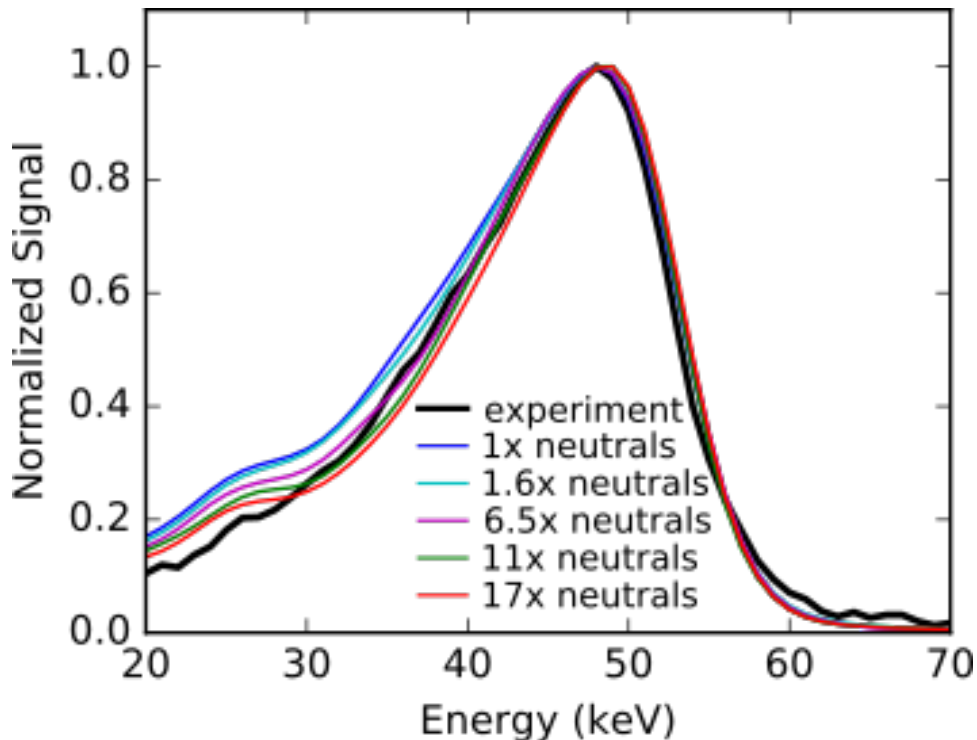


Figure 3.11: Slice of the image from figure 3.8 at $R = 1.8$ m overlaid with simulations using different neutral density values to vary the amount of charge exchange losses. Each result is normalized to their peak values for better profile shape comparison. Simulated signal values drop off faster at lower energies as neutral density increases.

The ratio of passive to active signals is compared in figure 3.12 for a slice at $E = 47$ keV. The passive contribution is larger than the active towards inner radii with the highest ratio appearing near smallest radii. The active component decreases towards lower radii since neutral particles from the core pass through regions of higher densities. This increases the re-ionization rate, thus decreasing the amount of signal detected. Low ratios around $R = 1.8$ m increases the confidence that most of the signals detected originate from the core of the plasma.
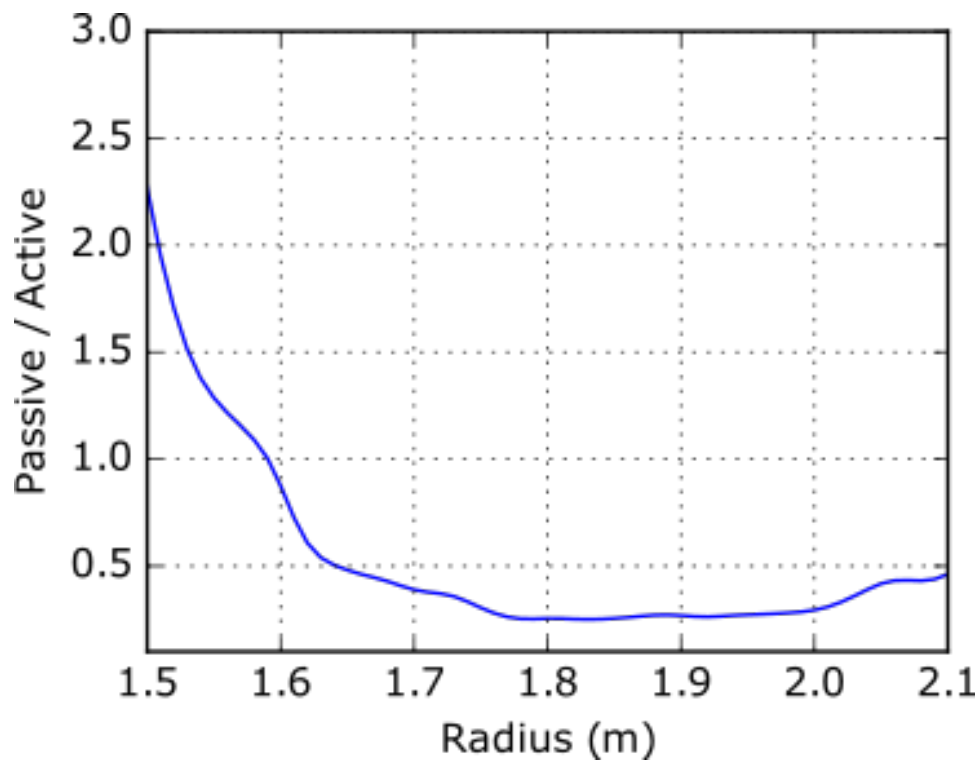


Figure 3.12: The passive to active ratio is taken from the simulation in figure 3.8(a) at $E = 47$ keV. The passive contribution exceeds the active contributions at inner radii.

Figure 3.13 shows a selection of four points on the image ranging from 1.5 m to 2 m centered around 47 keV for a signal produced by the 330LT beam. Simulated values are plotted against the experimental values at these 4 points to determine the deviation from experiment. Points that completely match should lie along a line with a slope of unity. Two models, one with and one without simulating passive signals, are compared to the experiment for the subset

of points in figure 3.14. The $r^2$ value, which is a measure of variance between the data and the model, is used to quantify the accuracy of each model. The result shows increasing agreement when the passive portion is included in the comparison, as the $r^2$ value increases from $r^2 = 0.66$ to $r^2 = 0.87$ for the four points on the image. The inner points, corresponding to radial positions of 1.52 and 1.67 m, deviate significantly and are caused by a different type of passive signal that will be discussed later on in section 3.4.2.
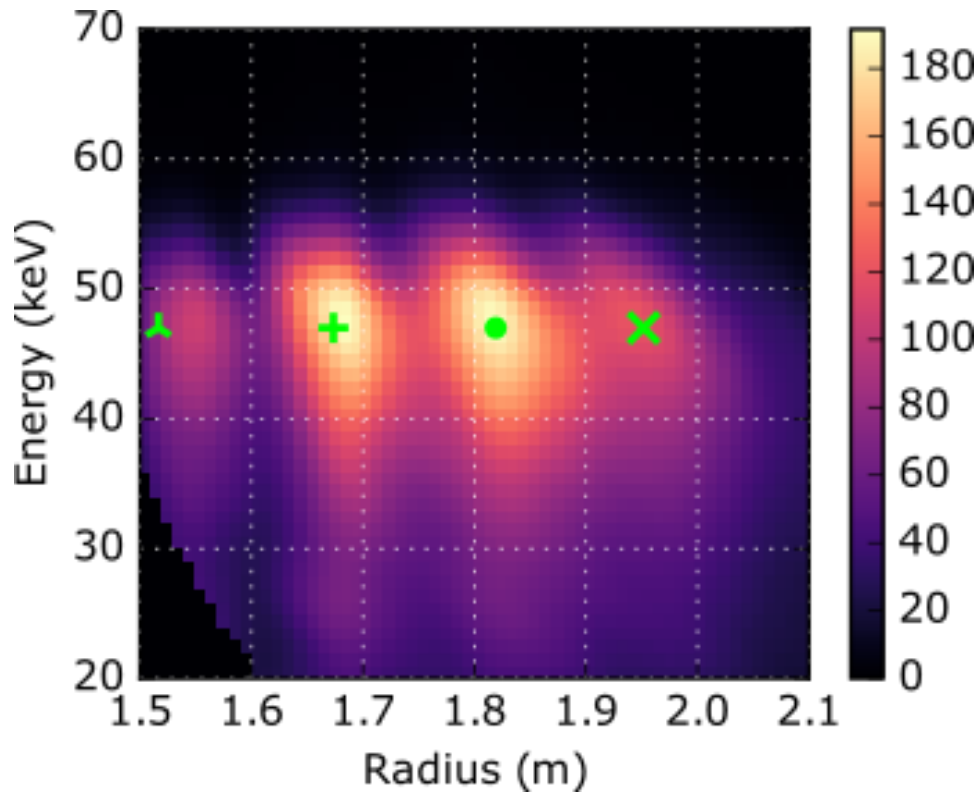


Figure 3.13: Four points are selected at different radii at $E = 47$ keV. The chosen points lie at the center between support structures.
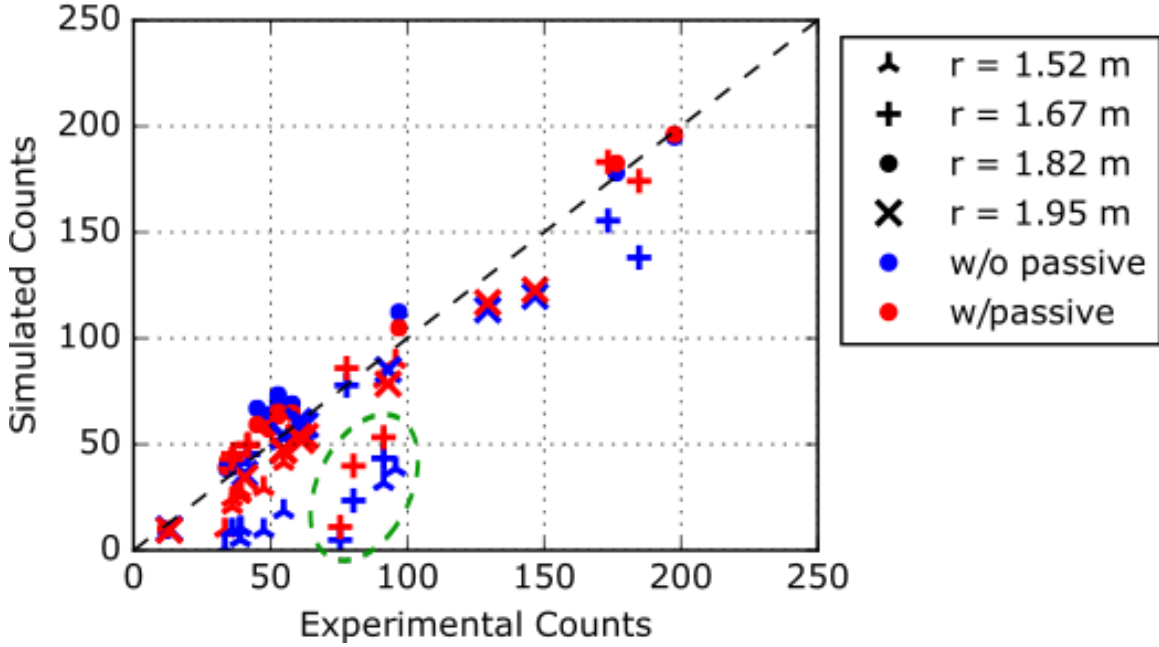
Figure 3.14: Simulated counts plotted against experimental counts at 4 radial positions for multiple conditions. Dashed line represents perfect agreement between simulation and experiment with a slope of 1. The simulation without passive signals has $r^2 = 0.66$ while the simulation with passive signals has $r^2 = 0.87$. The areas that significantly deviate from agreement are circled in green. Those points are attributed to another source of passive signals that are not accounted for in the current simulation.

The expected sensitivity of the diagnostic to various parameters, like temperature and density, is also checked by comparing the difference in signal. Each time period, corresponding to different plasma temperatures and densities, are subtracted from the previous time period to obtain the difference in signal. Figure 3.15 shows the comparison of signal changes through different background electron temperatures and densities between the experiment and simulation. The inclusion of passive signals marginally increases the agreement from $r^2 = 0.90$ to $r^2 = 0.95$ for the four locations indicated in figure 3.13. The simulation with and without passive signal matches the changes in signal for the experiment.
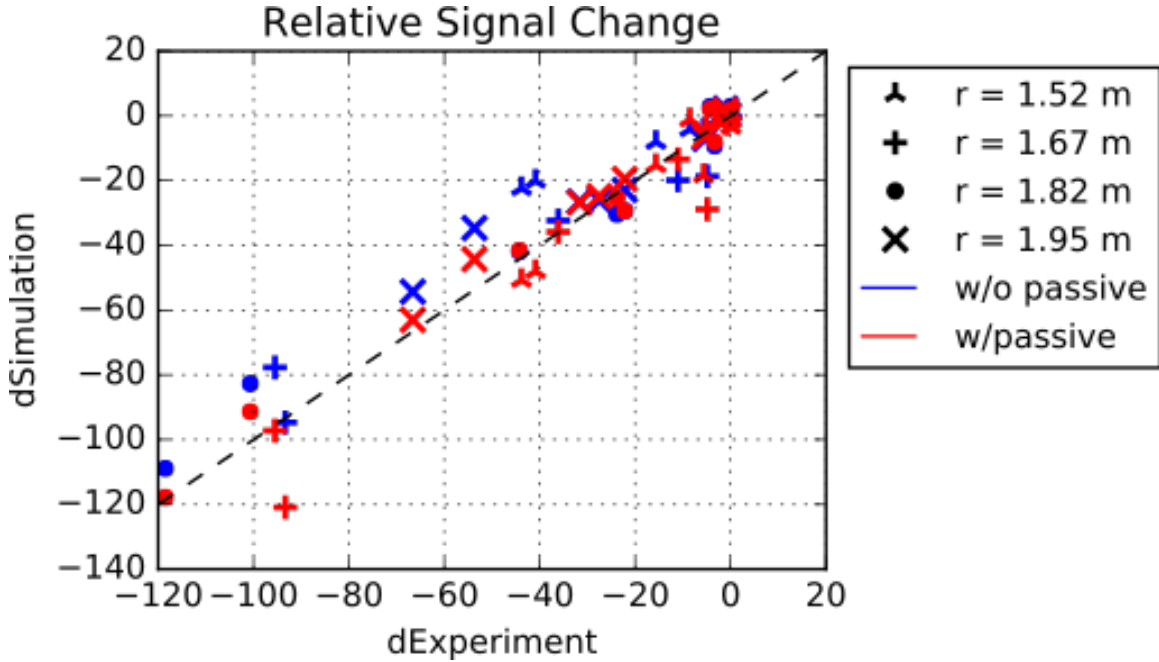
Figure 3.15: Temporal changes in signal, which corresponds to changes in electron temperatures and densities, are compared between the experiment and simulation for multiple cases. Dashed line represents perfect agreement with slope of 1. Changes in simulation with and without passive signals match well with experiment ($r^2 = 0.90$ and $r^2 = 0.95$ respectively).

Differences in the synthetic signal due to uncertainties in the input profiles are investigated in a sensitivity study. The Zeff profile contains one of the largest uncertainties because the quantity is not directly measured. For signals observed from the 330LT beam, changing Zeff by 20% causes a maximum signal change of around 15% as shown in figure 3.16(a). The plasma density is another quantity that is likely to cause large signal differences from uncertainties. Figure 3.16(b) shows that an error of 10% can cause a maximum signal change of around 80% at higher densities. The variation in the signal caused by profile uncertainties can account for the discrepancies in the simulated images.
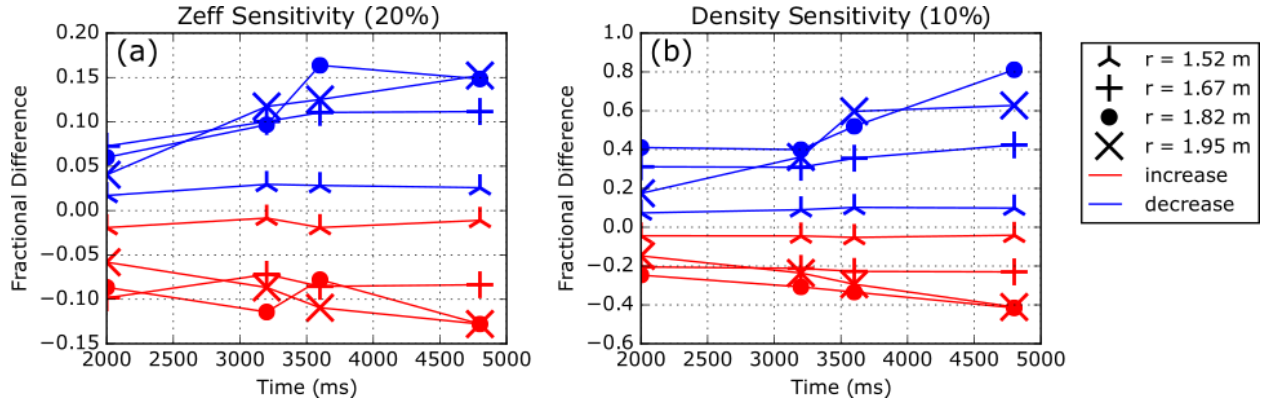
Figure 3.16: Sensitivity of 330LT beam to (a) 20% error in Zeff and (b) 10% error in density. The fractional difference of the INPA signal at different radii are plotted for different times.

## 3.4.2   Strong passive signal

The signal causing the deviation for the radii of 1.52 and 1.67 m in figure 3.14 is also observed in the absence of both diagnostic beams as shown in figure 3.17(a). Without beam neutrals, the edge cold neutrals are the only other neutral source for charge exchange within the INPA sightline. This leads to the conclusion that the strong signal originates from a population of fast ions with orbits that pass through the edge or SOL. This feature was not captured in the previous simulations since the distribution calculated by NUBEAM did not extend far enough into the SOL. This can be seen in figure 3.18(e) where the neutralization distribution, discussed later in this section, extends past the region where the NUBEAM distribution is defined (indicated by the white dashed lines). The NUBEAM distribution was created using the guiding center position of the particle but the actual particle location, which has a gyroradius around 2.5 cm at the edge, may be important in this case. Adjusting the charge exchange losses in the SOL did not appear to move distribution boundary.
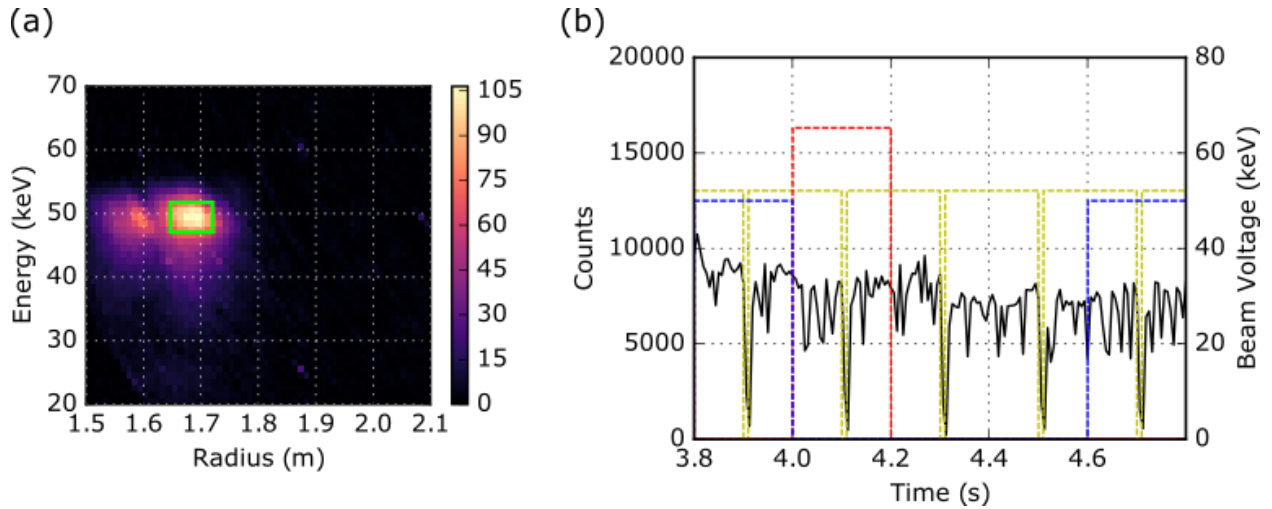
Figure 3.17: (a) Strong signal is seen on an INPA image during a period from 4.52 - 4.6 s from shot 175244. The core electron temperature and density is around 4 keV and $5 \times 10^{19}$ $m^{-3}$. (b) Total signal within the green boxed region is plotted (black) against time. The timing of the 330LT (blue), 330RT (red), and 210RT (yellow) beams are also plotted.
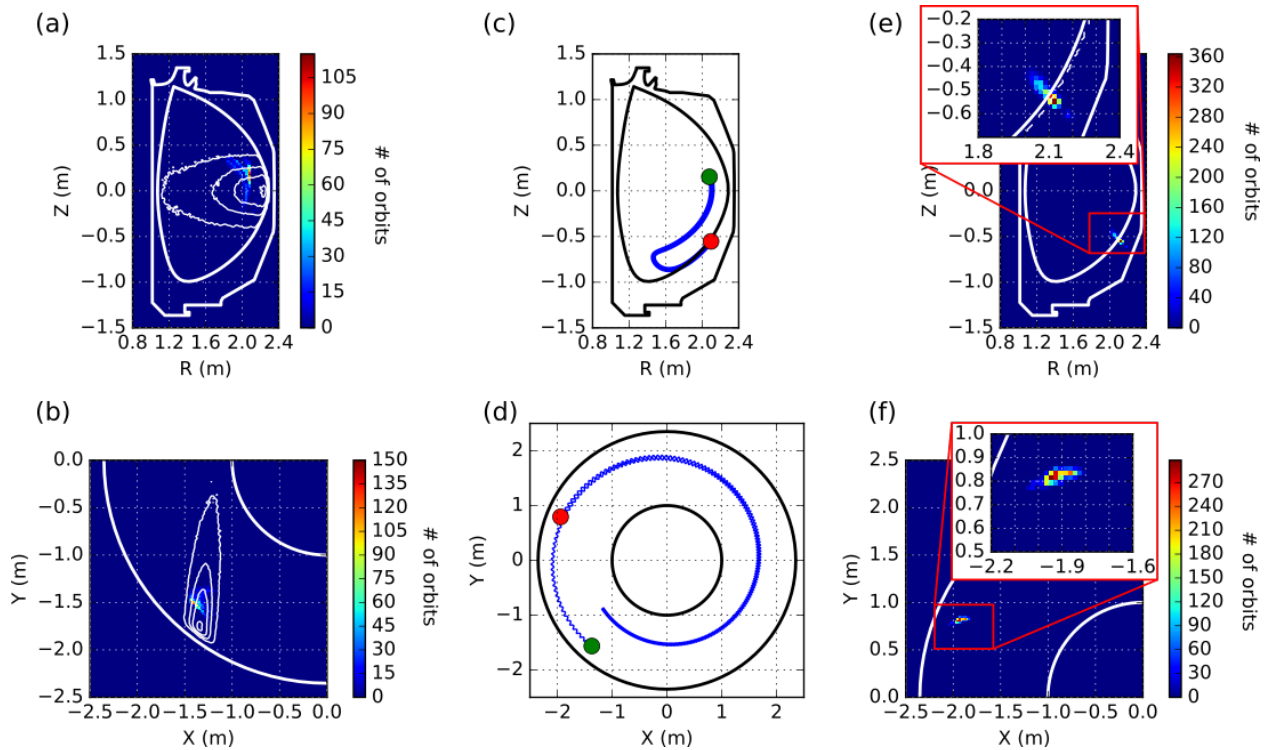
Figure 3.18: Birth distribution of particles that cause the strong passive signal are shown in (a) R-Z and (b) X-Y coordinates. The 210RT beam density contour is overlaid on the plot. A sample trajectory is shown in (c) R-Z and (d) X-Y coordinates. The green point indicates the birth location for the particle while the red point indicates the neutralization location. The trajectory is traced by the blue line. The distribution for the neutralization location is shown in (e) R-Z and (f) X-Y coordinates. The dashed white line in (e) represents the extent of the fast ion distribution calculated by NUBEAM.

The appearance and disappearance of the signal correlates with the timing pattern of the 210RT counter beam as shown in figure 3.17(b). In addition, the maximum particle energy detected matches the maximum injected beam energy. This suggests that the 210RT beam is the source of these passive signals. For this to happen, injected particles from the counter beam must change directions to be detected by the INPA.

To confirm the source of the passive signal, orbits are traced in reverse from two regions on the INPA in the absence of collisions. The first region corresponds to the location of the passive signal on the detector and spans labeled radii of $R = 1.63 - 1.73$ m on the image. The other region should not contain the passive signal and spans from labeled radii of $R = 1.91 - 2.01$ m on the image. The particles start on any point along the line of sight to simulate the neutralization location. The velocity vector is directed toward the detector and has a magnitude centered around the full energy component of the beam. Using a simple Eulerian method, time steps are taken in reverse to trace the orbit for two full poloidal cycles. During this period, scattering effects can be ignored since the orbit transit time is much shorter than the scattering time. Each point along an orbit is checked for any configuration space overlap with the 210RT beam footprint calculated by FIDASIM. Of the points that have the correct positional requirements, their velocity space coordinates are checked to make sure it falls within a valid range of birth pitch. If the phase space requirements are met, then the orbit is assumed to contribute to the signal.

After simulating around $\sim 10^7$ orbits, only a very small fraction ($\sim 10^3$) is found to contribute to the signal. Nevertheless, the ratio of signals between the two regions is found to be

around 100 (R $\sim$ 1.68) to 1 (R $\sim$ 1.96). This is qualitatively consistent with experimental observations where a ratio around 40 to 1 is found. The differences in ratios could be due to insufficient sampling and the simple method used to determine the signal level. In addition, noise from the experimental image may provide a systematic offset to the measured signal level.

Figure 3.18 shows the birth distribution and neutralization location of particles that contribute to the strong passive signal, along with a sample trajectory. As expected, most charge exchange events occur near the edge where the cold neutrals reside. Around 91.9% of particles follow trapped orbits while around 8.1% follow lost orbits. The particles appear to be born around $\rho \sim 0.7$, elevated 0.25 m above the midplane on the low field side. It should be noted that only particles born within the plasma are considered.

## 3.5   Conclusion

The INPA is a powerful diagnostic used to study local fast ion distributions. Active INPA measurements provide radial and energy resolved profiles of fast ions at a given pitch. Active and passive simulations successfully reproduce the experimental signals with an $r^2$ value of 0.87 at four different locations on the detector. The evolution of the experimental signals is also captured in the simulation with an $r^2$ value of 0.95, at the same four points. An effective calibration can be obtained using the results of the classical validation.

Difference in comparisons can be attributed to inaccuracies during modelling. The observed sawtooth instability was not accounted for within the TRANSP simulation leading to disagreement around the $q = 1$ surface located at $R = 1.9$ m. The discrepancies at lower energy regions could possibly be explained by inaccurate modelling within the INPASIM code, namely the linear relationship between light emission and particle energy. Uncertain-

ties in the Zeff and density profiles can explain the other differences between the experiment and simulation.

The most significant deviation from the experiment occurs when a strong passive signal caused by the 210RT beam is observed. The beam can deposit a small population of fast ions into trapped orbits that traverse the edge or even SOL region of the plasma. Preliminary calculations show precession times around 220 $\mu$s for these particular trapped orbits with charge exchange and slowing down times around 1.5 ms at the edge, indicating that these fast ions could lose $\sim 10\%$ of their energy on each orbit. Thus, there is a possibility that the population that produces the signal is toroidally localized but more work is needed to evaluate this possibility quantitatively. Additionally, the birth of fast ions outside of the plasma, which can be a source of toroidal asymmetry, was not accounted for and can play a significant role in the passive signal observed. Modelling of this population of fast ions can be performed with more accurate full orbit codes like ASCOT. Further exploration of the strong passive signal can potentially lead to new uses for the diagnostic, like the determination of the edge neutral density or localized edge fast ion measurements.

Local transport of fast ions can be studied using the high phase space resolution of the INPA. After noting the tendencies of the INPA during classical cases, deviations can be reliably attributed to instabilities. A measure of fast ion transport can be obtained by subtracting classical simulations from experimental signals to locate the surplus or deficit in signal.

# Chapter 4

# Characterization of EGAMs on DIII-D

## 4.1 Introduction

The term energetic particle-induced geodesic acoustic mode (EGAM) [9, 50] was first used after observations of a mode on DIII-D that was ∼50% below the geodesic acoustic mode (GAM) frequency. Associated fast ion losses from the mode were also observed and studied [9, 51, 52]. GAMs are n=0 oscillating zonal flows with m=0 perpendicular flow, m=1 pressure/density, and m=2 magnetic structures [53]. Their role in regulating cross-field turbulent transport makes them desirable to study. EGAMs share the same mode structure as GAMs but are driven by energetic particles rather than drift turbulence [54, 55, 53]. The first observation of GAM excitation by energetic particles appeared at JET using ion cyclotron resonance heating (ICRH) [56]. Since then EGAMs have been observed and studied at different devices like HL-2A [57, 58], LHD [59, 60, 61], ASDEX [62], EAST [63], and TCV [48]. Since EGAMs are usually observed when the counter plasma current (counter-$I_p$) beam

61

is present on DIII-D, the existence of a loss boundary is thought to provide the necessary gradient in energy to drive the mode [64]. The drive of the mode has been shown to be provided by inverse Landau damping on the beam ions [60].

Various theoretical works have studied whether modes originate from GAMs or they originate from a distinct branch [50, 65, 66]. Additionally, other studies have verified experimental observations for the different branches of EGAMs [67, 68, 69, 70, 71, 72, 73, 74, 75, 54]. Theoretical studies have found a pitch angle threshold for destabilizing EGAMs exists for conditions like DIII-D [76], but not for LHD [77]. The mode is found, through calculations, to have a small fast ion threshold for destabilization meaning that it appears quickly once the beam is turned on [78, 79, 80]. The structure of the mode can be determined by the plasma $\beta$ (ratio of plasma to magnetic pressure) [81]. Simulations show that resonant particle drift orbits provide a driving gradient for the mode to grow [82, 83]. The growth rate for the mode decreases when accounting for Landau damping [84]. EGAMs grow until the driving gradient is flattened through wave-particle trapping [65, 68, 78]. Second harmonics of the mode have been observed on DIII-D and are found to be caused by kinetic effects of energetic particles [85]. Experimental observations of daughter modes on LHD found to be caused by nonlinear wave coupling providing a seed for the mode [61, 86, 87, 73]. Frequency chirping has also been seen on LHD and is caused by hole clump formation in the pitch angle and energy velocity space coordinates for the energetic particle distribution [88]. Other studies have found that EGAMs affect turbulent transport [89, 69, 72] and channel energy and momentum from energetic particles to bulk ions [90, 91, 74, 92].

EGAMs have the potential to regulate new pathways for energy transfer between energetic particles and the bulk plasma. Before investigating the possible usage for EGAMs, it is important to have a proper understanding of the mode. The goal of this study is to robustly characterize EGAMs with a large database from DIII-D ($\sim$900 shots). The format of this chapter is as follows. Section 4.2 explains some underlying concepts of energy transfer

between particles and waves in tokamak plasmas. Section 4.3 explains the various diagnostics used in this study. Section 4.4 presents a typical case of a DIII-D EGAM. Section 4.5 presents results from a large database. Section 4.6 discusses discrepancies with previous studies and summarizes the findings.

## 4.2 Theory

The general resonance condition in Eq. 1.9 can be simplified in the case of EGAMs. The cyclotron motion is unlikely to contribute to resonance with EGAMs since the frequency is much larger than what is observed. The toroidal motion of the particle does not contribute energy to the mode because EGAMs are n=0 modes which do not have any fluctuating fields in the toroidal direction. As a result, the generalized resonance condition (Eq. 1.9) is simplified to

$$\omega = m\omega_\theta \tag{4.1}$$

because only the poloidal motion of the particle can transfer energy to the wave.

According to Ref. [93], the analytic growth rate of the EGAM is:

$$\gamma_G \approx \frac{\omega_G \sqrt{\pi}}{2} \left[ \sqrt{\pi} C_D \left[ (5\lambda_0 - 2)(2 - \lambda_0) - \frac{15\Delta\lambda_0^2}{4(1 - \lambda_0)} \right] \right. \\ \left. - \left[ \frac{1}{2} \frac{\omega_G^3 R_0^3 q^3}{v_{Ti}^3} + (1 + \tau_e) \frac{\omega_G R_0 q}{v_{Ti}} \right] e^{\left( -\frac{\omega_G^2 R_0^2 q^2}{v_{Ti}^2} \right)} \right] \tag{4.2}$$

where $\omega_G$ is the GAM frequency, $C_D$ is a parameter describing the distribution function, $\lambda_0 = v_\perp^2 / v^2$ is the central pitch angle parameter for the slowing down distribution, $\Delta\lambda_0$ is the width in pitch of the distribution, $R_0$ is the major radius, $q$ is the safety factor, $v_{Ti}$ is the ion thermal velocity, and $\tau_e$ is the ratio of the electron to the ion temperature. The first

term describes the mode drive from an injected beam distribution. Here, the effect of the loss boundary is not taken into account. The second term describes the ion Landau damping of the mode which is the dominant damping mechanism.

## 4.3   Apparatus

DIII-D is a mid-sized tokamak with a major radius of about R=1.67 m and a minor radius of about a=0.67 m. Up to 8 neutral beams are used to heat the plasma. For the data in this chapter, there were 2 beams directed in the counter-$I_p$ direction and 6 beams directed in the co-$I_p$ direction, with an option for 2 of the co-$I_p$ beams to be tilted into an off-axis position.

The magnetic equilibrium is reconstructed using the equilibrium code EFIT [38] constrained by magnetic probes around the vessel. The internal magnetic structure can be further constrained with the motional stark effect diagnostic (MSE) [39]. The electron density is typically measured using the Thomson scattering system [40] corroborated by the $CO_2$ interferometer [94]. The profile reflectometer can also be used to further validate the density profile [42]. While the Thomson scattering system is the main tool for diagnosing electron temperature, the electron cyclotron emission radiometer [41] can also be used for further validation of the temperature profile. Charge exchange recombination spectroscopy is used to measure the carbon impurity temperature, density, and rotation [43].

Magnetic fluctuations associated with EGAMs are detected by a toroidal array of 14 magnetic probes along the outer edge of the device. Density perturbations can be measured by the beam emission spectroscopy (BES) diagnostic [95]. Comparing the level of fluctuations along an array can provide information on the poloidal structure of the mode. The electrostatic potential perturbation is indirectly measured by the Doppler backscattering (DBS) diagnostic [96] through the ExB velocity fluctuation measurement.

The operating principle for each of these diagnostics are described in Ch. 2.

## 4.4   Example Discharge

An example discharge containing EGAMs is examined to get a picture of the mode. Shot 169121 is selected because it is primarily fueled by the counter-$I_p$ beam and the magnetic spectrogram (Fig. 4.1) does not show any other strong mode activity besides the EGAMs. The appearance of the mode is correlated with the timing of the counter-$I_p$ beam so the mode appears/disappears when the beam turns on/off. The co-$I_p$ beam appears for short blips for diagnostic purposes. Traces of various plasma parameters for the discharge are shown in Fig. 4.2. As the discharge evolves, the amplitude of the 1st harmonic and safety factor ($q$) decrease, while the current, density, and temperatures increase.

Based on the resolution of the spectrogram (Fig. 4.1), the mode appears to be bursting. Closer examination of the magnetics signal for the burst at $\sim$476 ms is shown in Figs. 4.3(a) and 4.3(c). The fundamental frequency of the perturbation is determined by the time between successive peaks indicated by the black points and appears to chirp over a range of $\sim$4 kHz. The clarity of the chirp is not as obvious due to the contribution of the 2nd harmonic. Figures 4.3(b) and 4.3(d) show a clearer example of chirping for another shot (134503) where the no second harmonic signal is present.

The location where the mode can resonate with the injected beam ion distribution can be seen in the space of normalized $P_\phi$ and $\mu$. Figure 4.4 shows beam deposition by the counter beam at 480 ms in the sample discharge. Since the EGAM appears shortly after the onset of counter-beam injection before appreciable collisional slowing can occur, the orbit topology map is for full-energy ions near the injection energy. Approximately 30% of the full-energy neutrals are deposited on loss orbits. Orbits that resonate with the observed
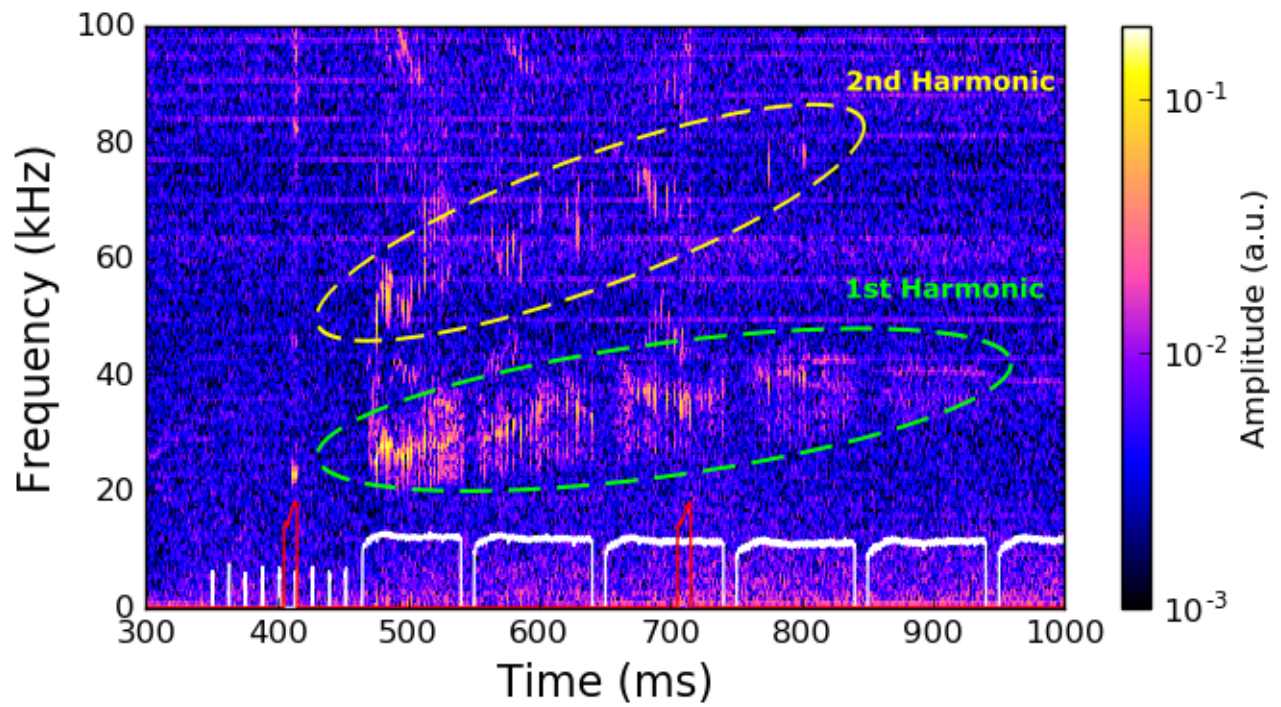
Figure 4.1: Magnetics spectrogram of shot 169121 showing the 1st (green) and 2nd (yellow) harmonics of EGAMs. The white traces indicate the timing of the counter $I_p$ beam ($\sim$76 keV, $\sim$1.7 MW) while the red trace indicates the timing of the co-$I_p$ beam ($\sim$81 keV, $\sim$2.4 MW).
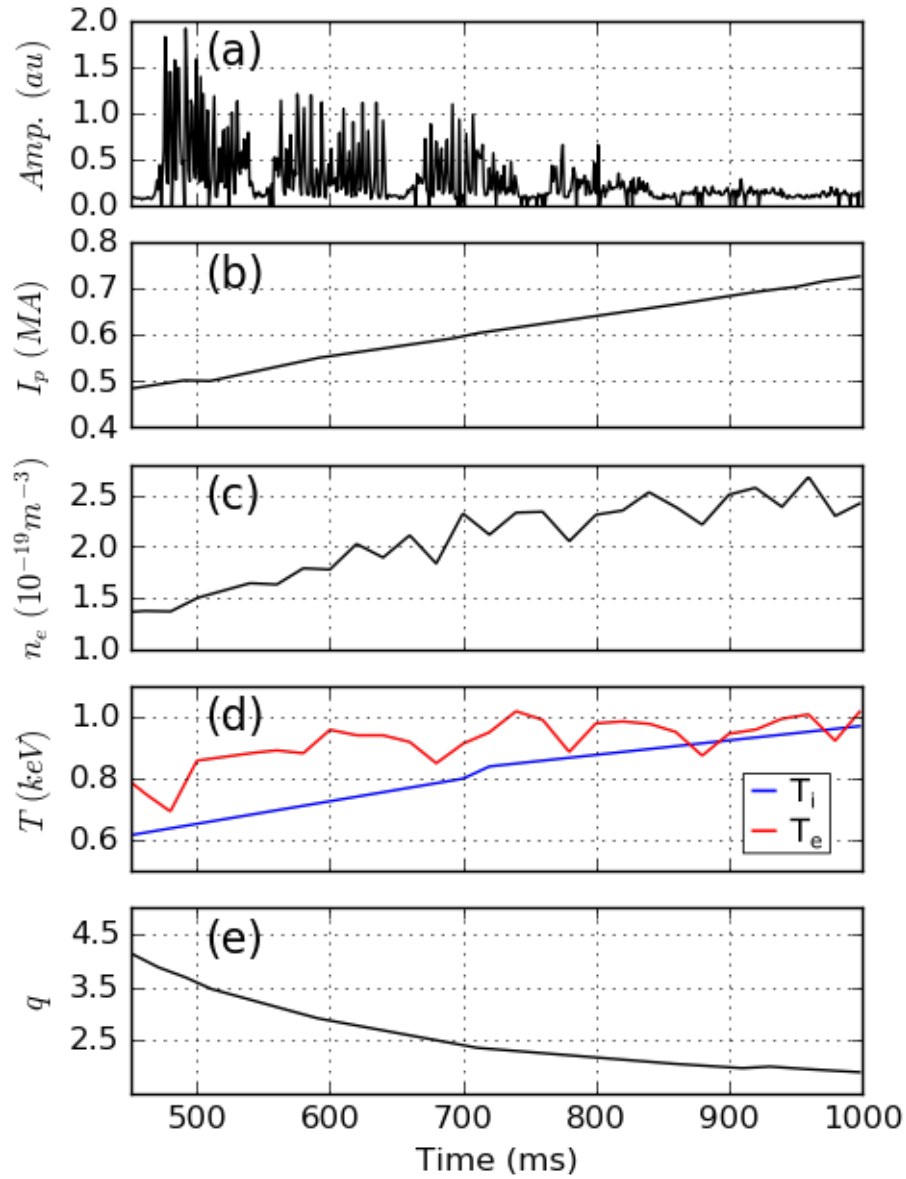
Figure 4.2: Time traces for shot 169121 for the (a) 1st harmonic mode amplitude, (b) current $I_p$, (c) density $n_e$, (d) temperatures T, and (e) safety factor $q$. The values for the density, temperatures, and safety factor are all taken at r/a∼0.25.
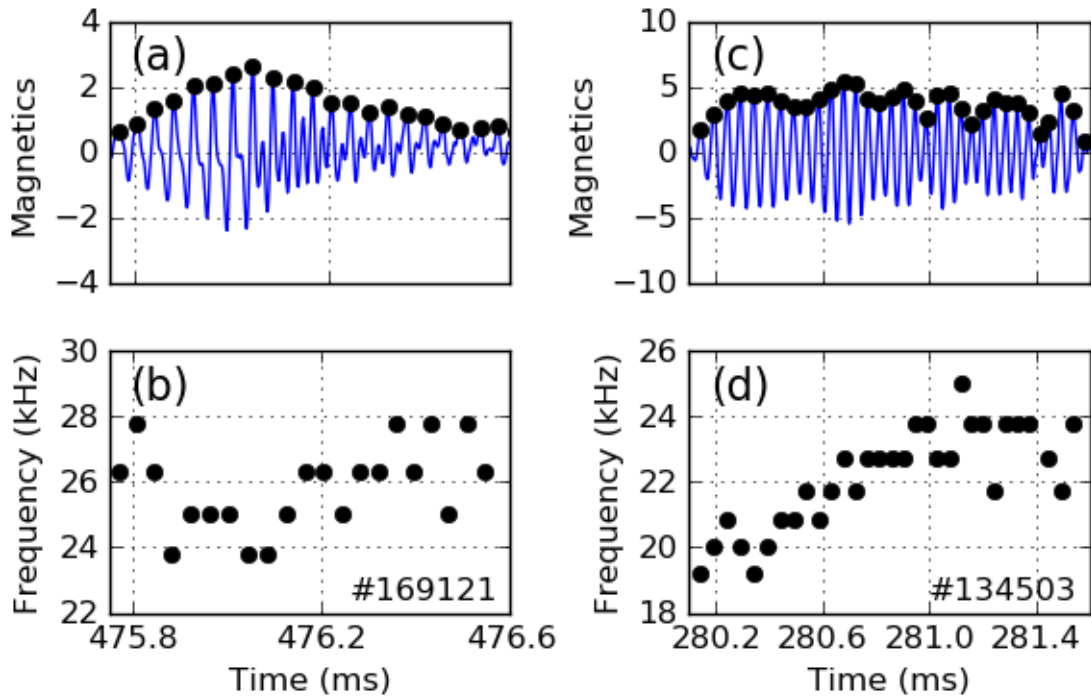
Figure 4.3: (a, c) Signals from magnetic probes for an EGAM. The black dots represent the peaks of the magnetic perturbation. (b, d) The frequency of the mode is determined by the period between each successive peaks. Overlap with the 2nd harmonic is present for shot 169121 (left) while only the 1st harmonic is observed for shot 134503 (right).
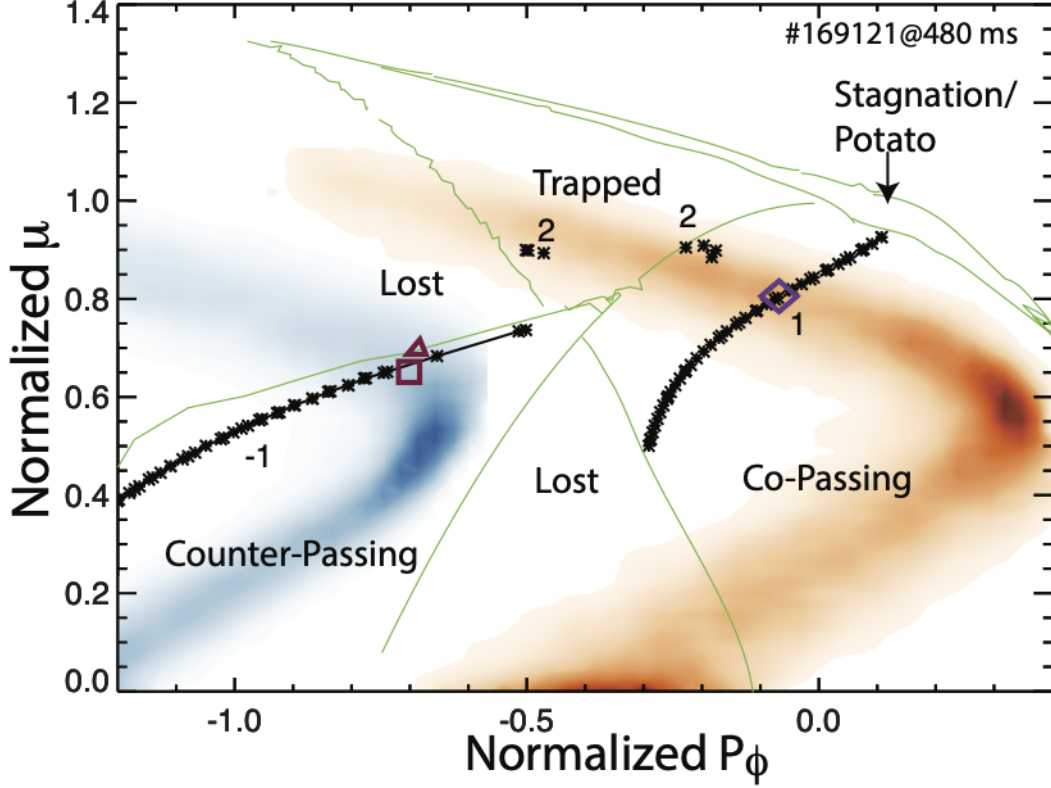
Figure 4.4: Location of beam deposition in phase space for full-energy beam ions injected by the tangential counter beam (blue shading) and by the tangential co beam (orange shading) in the discharge of Figs. 4.1 and 4.2. The symbols represent orbits that resonate with the 27 kHz, $n = 0$ EGAM; the numbers indicate the integer that multiplies $\omega_\theta$ in the resonance condition in Eq. 4.1. The ordinate is the normalized magnetic moment $\mu B_0 / W$, the abscissa is the toroidal canonical angular momentum normalized to the poloidal flux at the last closed flux surface, and the thin lines demarcate topological boundaries. The square and diamond represent the confined orbit shown in Fig. 4.5, while the triangle represents the unconfined orbit.

EGAM are close to the loss boundary, so a sharp velocity-space gradient is available to drive instability. Figure 4.5 shows that this boundary corresponds with the hyperbolic "X" point in orbit topology space that occurs on the small major radius side of the magnetic axis, at the boundary between confined counter-passing orbits and large unconfined banana orbits [97]. As assumed in Fu's original theory of EGAMs [50], the orbit width of the resonant counter-passing ions is very large, nearly half of the minor radius. Figure 4.4 also shows that co-passing orbits readily satisfy the resonance condition in Eq. 4.1 but, in contrast to counter-passing orbits, the resonant orbits do not straddle a loss boundary.
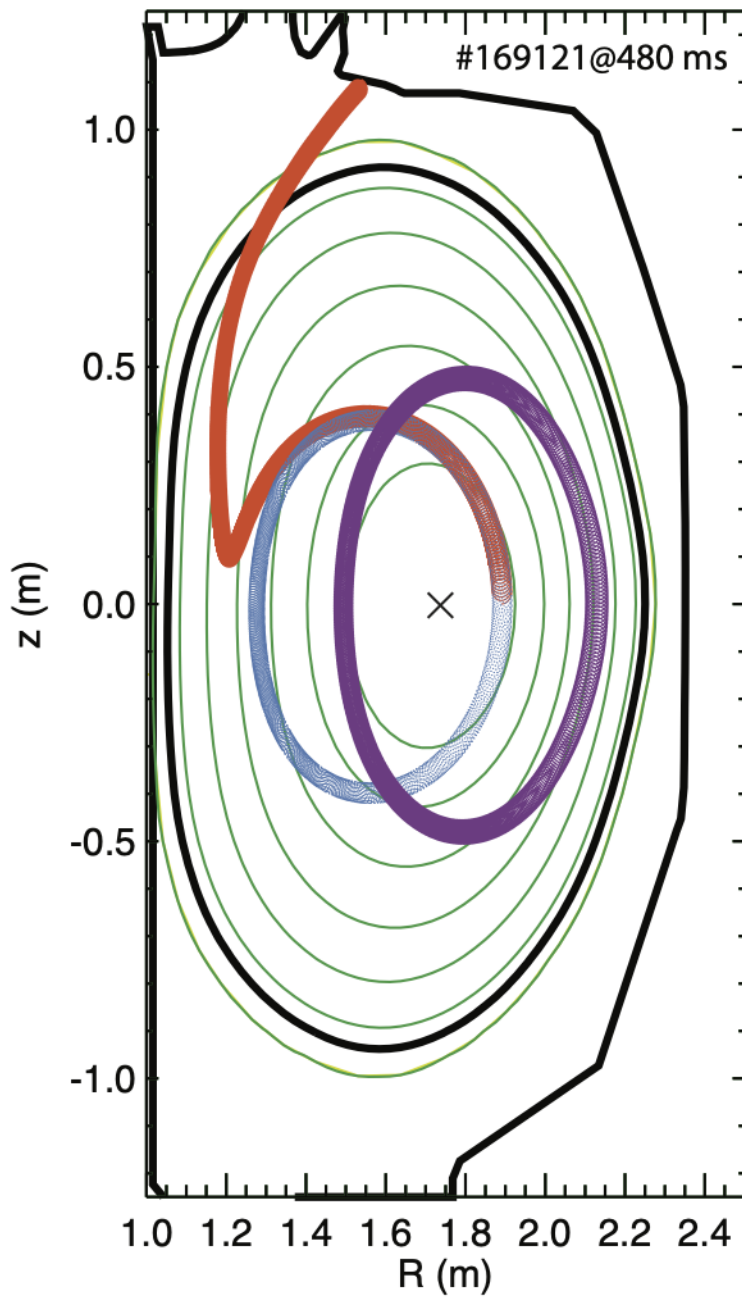
Figure 4.5: Elevation of DIII-D, showing flux surfaces (thin lines), the magnetic axis (X), and the last closed flux surface and vessel boundary (thick lines). Projections of a co-passing and counter-passing orbit that can resonate with the observed EGAM along with nearby loss orbit are also shown.

70

As the plasma current increases, the fast ions become better confined, so the counter-beam loss-boundary gradient weakens as the discharge evolves. If the increasing poloidal field was the only change in the discharge, the fraction of lost full-energy neutrals would fall to 18% by 1000 ms; however, since the density also increases, more neutrals are deposited at larger radius (where the confinement is poorer), so the actual lost fraction drops to 24%.

### 4.4.1   Mode structure

Figure 4.6 shows the toroidal and poloidal mode structure for the magnetic perturbation in shot 142111. Measurements by the toroidal array do not show any changes in the phase along the torus, which indicates toroidal symmetry (n=0) for the mode. The poloidal array measures a phase change of $4\pi$, suggesting an m=2 poloidal magnetics structure.

The multi-channel DBS diagnostic probes turbulent density fluctuations with low-to-intermediate wave number ($k_\theta \rho_s \sim$ 1 - 10 $cm^{-1}$) with a collimated millimeter wave beam propagating approximately orthogonal to the background magnetic field. The probe beam refracts as it penetrates the plasma, causing the wavenumber to decrease to its lowest point at cutoff, where the beam propagates approximately in the poloidal direction. The beam backscatters from turbulent fluctuations along its path with most of the scattered power coming from near the cutoff location. The Doppler shift of the backscattered millimeter waves is approximately given by $\omega_{Doppler} = k_\theta \, v_{E \times B}$, where $v_{E \times B}$ is the poloidal ExB velocity. Fluctuations in the Doppler shift at the EGAM frequency can be used to determine the EGAM potential fluctuation. In Fig. 4.7, measurements from the eight probe beams of the DBS system are used to construct a low resolution picture of the radial mode structure for the perturbed electric field on shot 169121. Ray tracing with the code GENRAY [98] shows the probe beams all propagate approximately in the plasma midplane, with cutoffs in the range $\rho = 0.02 - 0.98$, probing $k_\theta \sim$ 1 - 2 $cm^{-1}$. Of course, EGAMs have an associated density per-
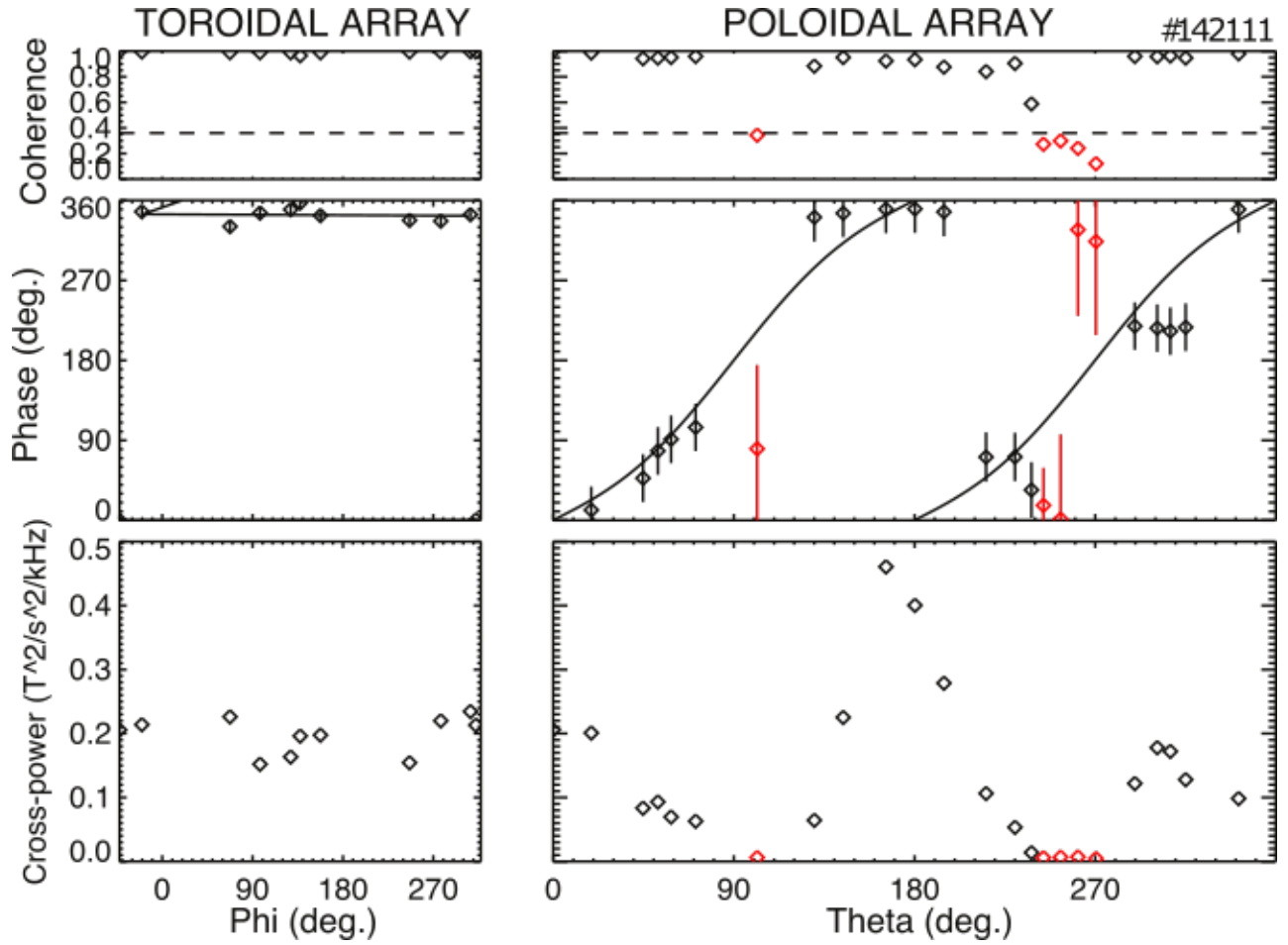
Figure 4.6: Phase of magnetic fluctuation measured by a toroidal and poloidal array of probes. The measured phase does not change between the toroidal array meaning that the measured mode is toroidally symmetric (n=0). The phase in the poloidal array changes by a $4\pi$ which means the mode has an m=2 poloidal magnetic structure. Points with coherence <0.36 are marked in red.

turbation that must be considered in interpreting the DBS measurements. Long wavelength density perturbations modulate the index of refraction of millimeter waves passing through them, which modifies the scattered spectrum in a way that is difficult to distinguish from a fluctuation of the Doppler shift. Since the density perturbation associated with EGAMs is expected to have an m=1 poloidal structure, the density pertubation is expected to be small in the plasma midplane, with little effect on the Doppler shift measurements used to infer the potential fluctuation (m=0 poloidal structure). The mode is localized towards the inner half of the plasma which is in qualitative agreement with Ref. [50]. Profile quantities within the database are characterized by the normalized toroidal flux parameter around r/a∼0.25 which appears to be the peak according to Ref. [50]. The amplitude of the perturbation for this shot is an order of magnitude lower than the inferred electric field perturbation in refs. [51, 52]. Despite the limited radial resolution, the electrostatic potential perturbation, obtained by the radial integration of the electric field perturbation, qualitatively agrees with the results shown in Ref. [54].

Reference [99] uses a camera to image the D-$\alpha$ beam emission over a broad spatial range. Part of the mode structure for the density perturbation (m=1) is measured and is in qualitative agreement with the results found in Fig. 4.7, for the electrostatic potential perturbation (m=0). The mode amplitude is lowest near the magnetic axis and increases as the distance from the center increases. Reference [9] used the BES diagnostic to show the m=1 poloidal structure of the density fluctuation. The null point at the height of the magnetic axis, diagnosed by a vertical BES array, was found to shift with the vertical displacement of the plasma.

Radial BES measurements from shot 134503 are shown in Fig. 4.8 where a strong outward radial propagation is observed. Density perturbations initially appear near the center of the plasma and eventually end up near the edge. Similar radial phase variations for toroidal Alfven eignenmodes imply that energy flows from the interior to the edge [100].
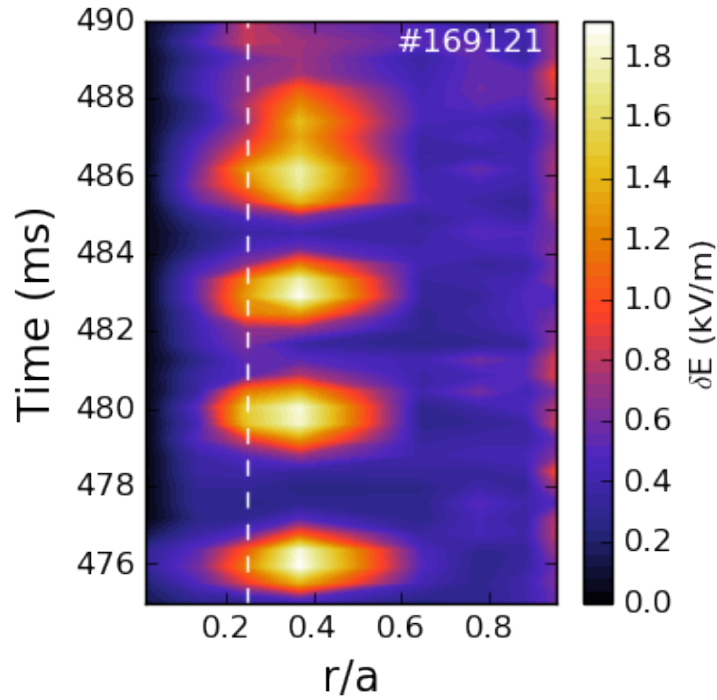
Figure 4.7: The mode structure of the electric field perturbation, diagnosed from the DBS diagnostic, for the 1st harmonic in Fig. 4.1 is plotted for the more prominent modes in shot 169121. The structure is measured at 8 radial locations and peaks around r/a~0.4. The white dashed line is situated at r/a=0.25 which is the radial value used to characterize profiles in the database.
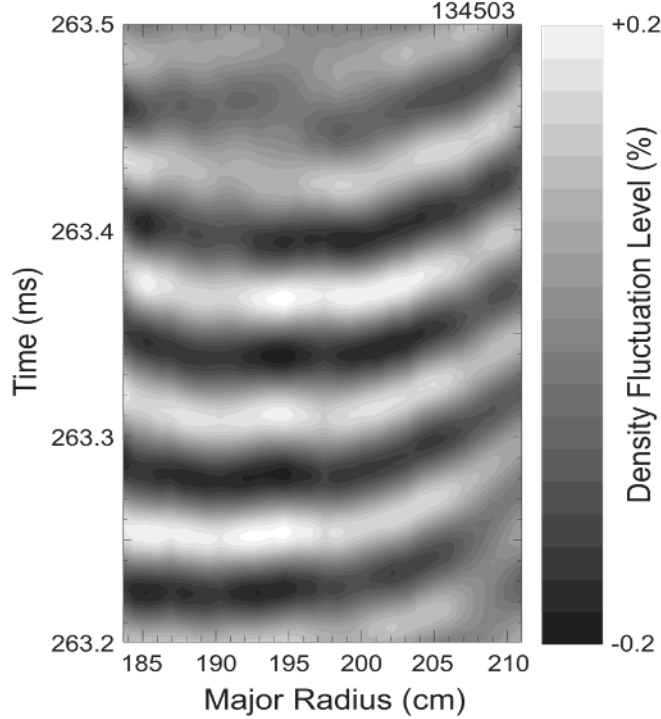
Figure 4.8: EGAM density fluctuation measured by a horizontal array of BES channels. Perturbations start at inner radii before ending at outer radii.

## 4.5 Database

A database from ~900 shots is compiled from t=300-1000 ms which is usually during the current ramp phase of the discharge. The selected shots are based off of the large database of Ref. [101]. In this database, plasma conditions for different parameters range from $0.4 \leq I_p \leq 1.1 \ MA$ for plasma current, $2.0 \leq B_T \leq 2.1 \ T$ for toroidal field, $0.2 \leq \beta_p \leq 1.9$ for poloidal beta, $0.2 \times 10^{-19} \leq n_e \leq 5.9 \times 10^{-19} \ m^{-3}$ for central electron density, $T_e \leq 8.1$ $keV$ for central electron temperature, and $T_i \leq 6.9 \ keV$ for central ion temperature.

Equilibrium reconstructions used in the database are only constrained near the edge with magnetic probes. While constraints with internal MSE measurements increase the fidelity, it comes at the cost of poorer statistics since data are only gathered when certain neutral beam patterns are used. Comparisons of results with and without internal measurements show that general conclusions remain unchanged.

Mode properties like amplitude and frequency are characterized using magnetic spectrograms. The temporal resolution is ~1 ms with a ~2 ms hanning window while the spectral resolution is ~0.5 kHz with a ~0.3 kHz smoothing range. The location for potential modes is found in the spectrogram by the following steps:

1. Frequency range manually selected where the 1st harmonic of EGAMs reside

2. Maximum amplitude within frequency range is detected for each time slice

3. Detected point is checked to have a gaussian-like shape in the frequency spectra

4. The phase difference between magnetic probes is checked to ensure an $n = 0$ mode structure

5. Point is classified as stable or unstable:

   (a) For an unstable point, the amplitude is checked to be above a manually set threshold

   (b) For a stable point, the amplitude is checked to be below a different manually set threshold and not within 5 ms of any points above threshold

Around 28000 unstable points and 26000 stable points are found with a counter-$I_p$ beam on; other beams may also be present. Lists of correlated parameters and stability correlations are listed in B.1 and B.2.

## 4.5.1 Mode frequency

The frequency of the mode is found to have the highest correlation ($r=-0.71$) with $q$. This relationship can be seen in Fig. 4.9 where lower frequency corresponds to higher $q$ values. Because of the $n=0$ EGAM structure, the poloidal orbit frequency of resonant particles is
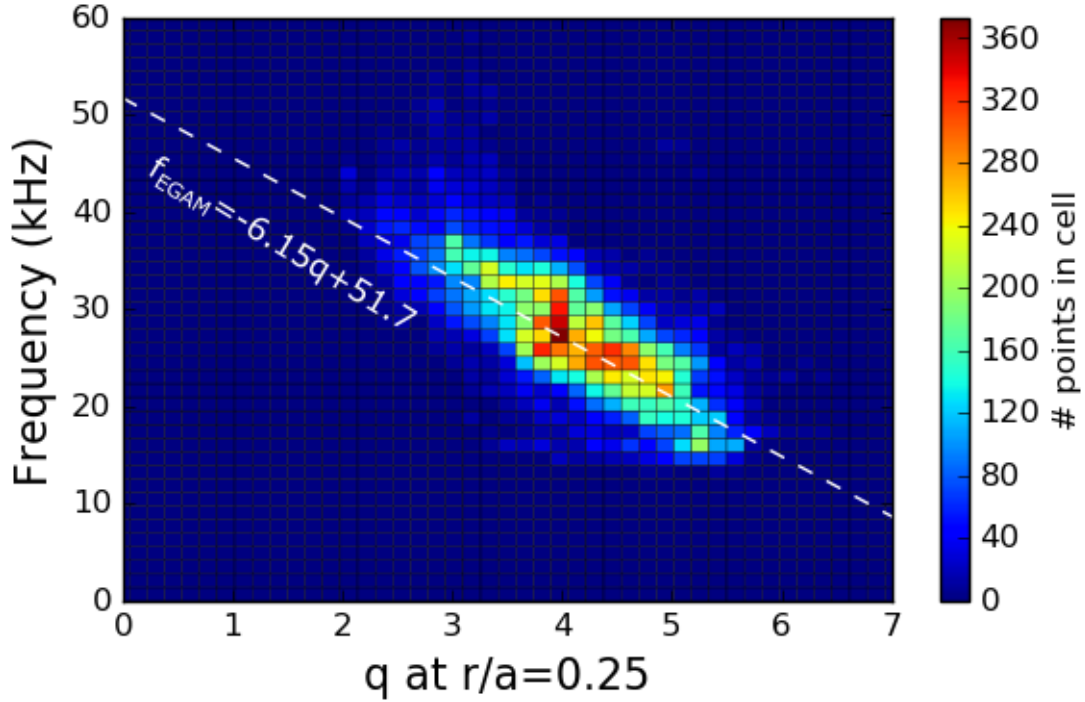
Figure 4.9: Histogram of mode frequency against $q$ shows a strong relationship where the mode frequency increases as the $q$ value decreases. The white line represents the best linear fit of the data points.

the quantity of interest, which is largely determined by the drift orbit. Higher $q$ values cause particles to have lower drift velocities which, from the resonance condition in Eq. 4.1, corresponds to lower mode frequency.

The EGAM frequency is compared to the GAM frequency in Fig. 4.10 and found to be around half the GAM frequency. The equation for the GAM frequency used is

$$\omega_{GAM}^2 = 2\frac{c_s^2}{R_0^2}\left(1 + \frac{1}{2q^2}\right) \tag{4.3}$$

which is derived from [102] and found in [103]. Here, $R_0$ is the major radius and $c_s = \sqrt{(T_e + 7/4\,T_i)/m_i}$ is the ion acoustic speed. Reference [50] shows that EGAMs typically have frequencies that are around half the GAM for $\omega_0/\omega_{GAM}=1$. It can be concluded that the observed mode on DIII-D originates from a distinct wave branch separate from the GAM branch.
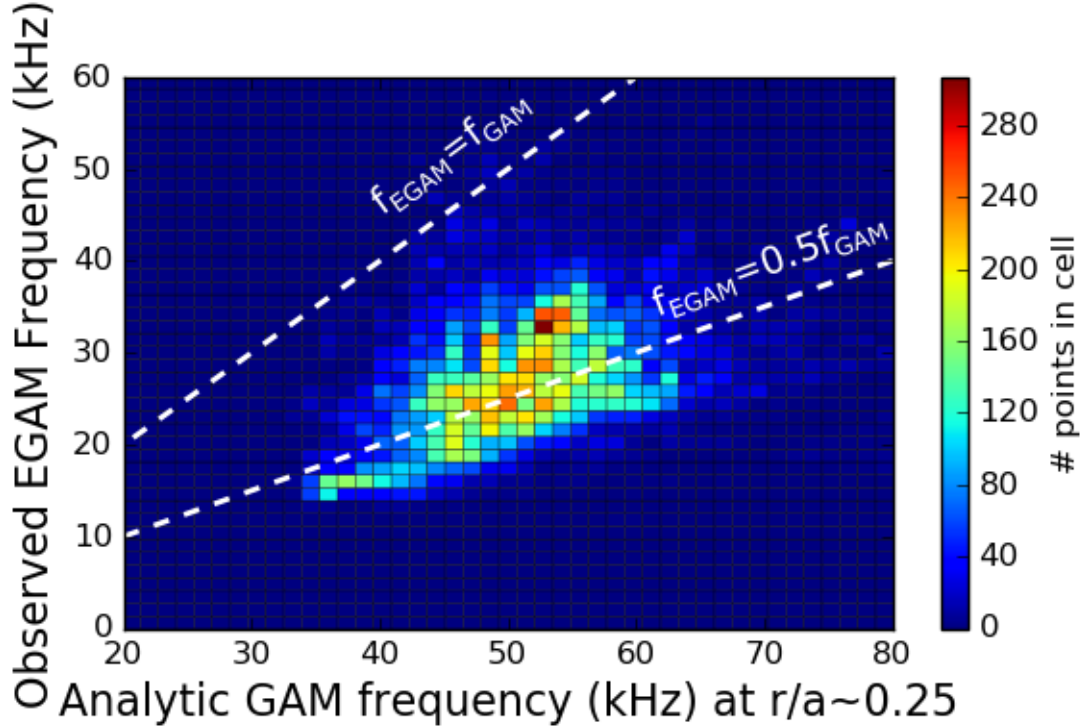
Figure 4.10: The frequency of the mode is about half the GAM frequency.

Figure 4.11 compares the frequency to the temperature, $(T_e + 7/4\,T_i)^{1/2}$, in Ref. [60] and found a correlation value of $r$=0.37. The result is similar to Fig. 4.10 since the temperature factor is proportional to the speed of sound and GAM frequency. The ratio of the temperatures $(T_i/T_e)$ is found to have no correlation with the mode frequency $(r$=0.02).

### 4.5.2 Mode stability

A stability map for EGAMs is shown in the space of $q$ and $\beta_p$ (ratio of plasma pressure to poloidal pressure) in Fig. 4.12. This is created by binning stable and unstable points and calculating the percentage of unstable points within a cell; the shading of the color for each cell reflects the percentage. The redder the color, the more unstable points there are in the cell, while the bluer the color, the more stable points there are in the cell. A white cell indicates the point where there are equal number of unstable and stable points within the
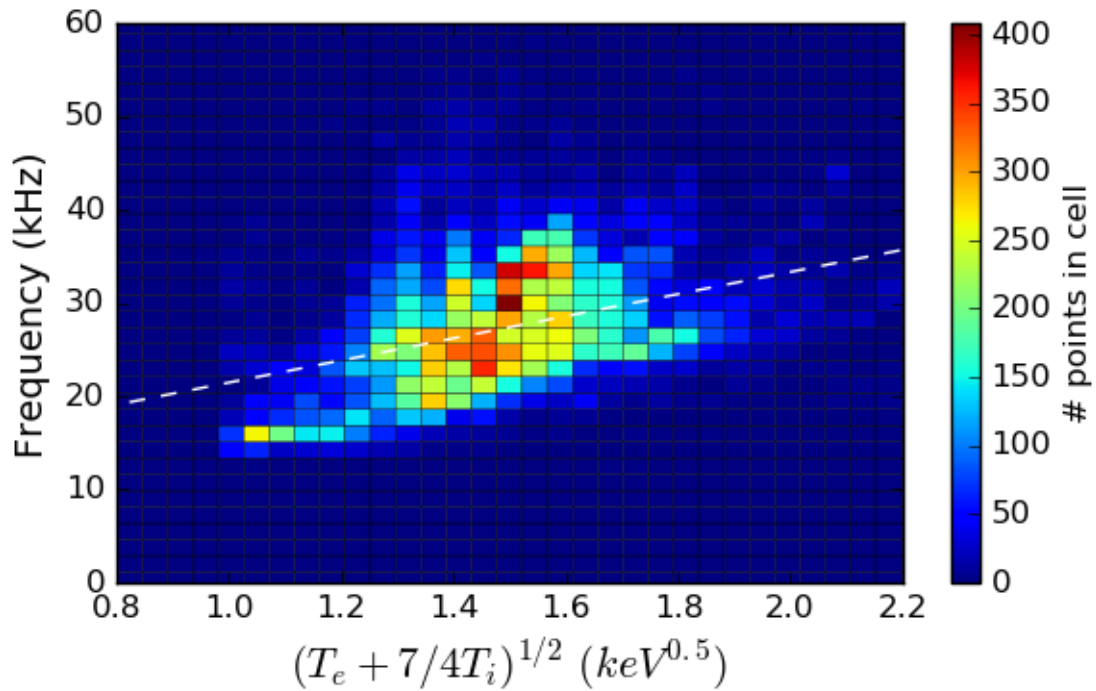
Figure 4.11: The linear correlation value of the EGAM frequency compared to the temperature is $r$=0.37. The linear best fit is represented by the dashed white line. This figure is similar to Fig. 4.10 since the temperature factor is proportional to the ion acoustic speed, which is also proportional to the GAM frequency.
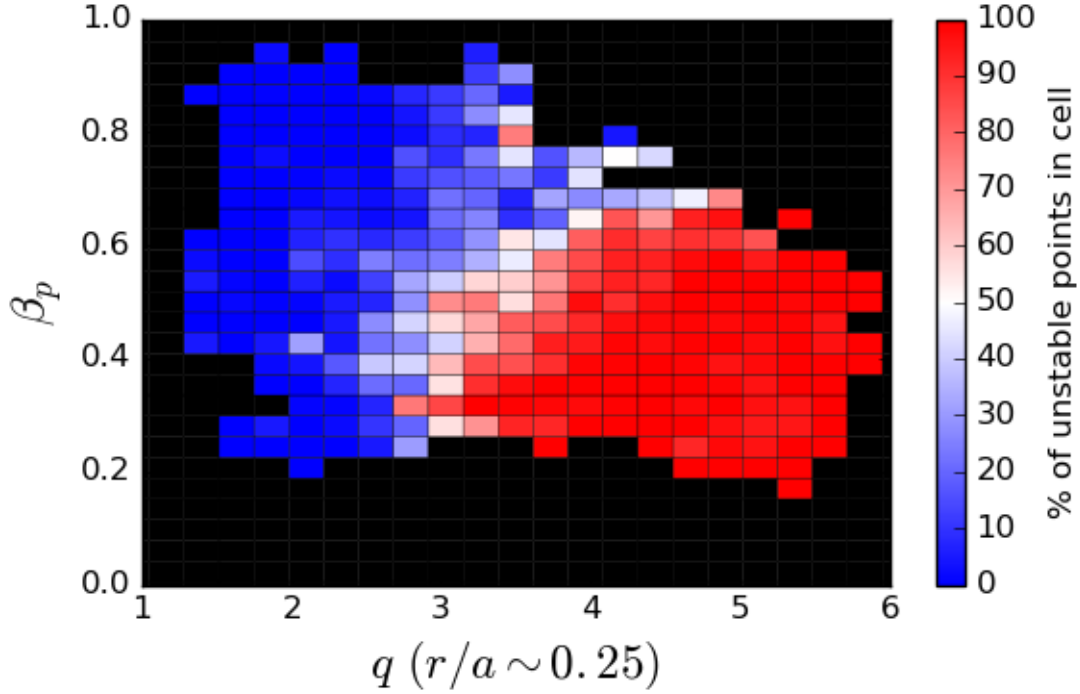
Figure 4.12: Stability map of EGAMs in the space of $q$ and $\beta_p$. The percentage of unstable points in each cell is indicated by the color. Redder colors indicate that there are more unstable points while blue colors indicate that there are more stable points. The mode tends to be unstable at high $q$ and low $\beta_p$.

cell. A boundary for the transition between stable and unstable regions is seen to follow an increase in $q$ and $\beta_p$. EGAMs tend to be more unstable at higher $q$ and lower $\beta_p$ for a given $q$.

**Beam dependence**

Figure 4.13 investigates the stability of the mode in the presence of the different beam geometries on DIII-D (one beam geometry for each data point). The beam powers for the counter-$I_p$, co-$I_p$, and off-axis cases range from $\sim$1-5 MW, $\sim$1-9 MW, and $\sim$1-4 MW respectively. The counter-$I_p$ beams have the largest proportion for the unstable region followed by the co-$I_p$ beams. The off-axis beams (in the co-$I_p$ direction) are virtually stable in the space that it fills. Table 4.1 shows the number of unstable and stable points found in

| Beam Geometry | Unstable Points | Stable Points | %Unstable Points |
|---|---|---|---|
| Counter-$I_p$ | 3899 | 3900 | 50.0% |
| Co-$I_p$ | 4615 | 68014 | 6.4% |
| Off-axis | 41 | 6073 | 0.7% |

Table 4.1: Table of the number of unstable/stable points for each beam geometry. The counter-$I_p$ beams have the largest fraction of unstable points, followed by the co-$I_p$ beams, and then the off-axis beams.

the presence of the different beam geometries. Around 50% of the points for the counter-$I_p$ beams are unstable, while around 6.4% of the points for the co-$I_p$ beams are unstable. Less than 1% of points for the off-axis beams are unstable. In comparison, the mode is most easily destabilized when only using the counter-$I_p$ beams. This is followed by the co-$I_p$ beams and then the off-axis beams.

**Mode drive**

Theoretically, the drive for the mode is determined by the fast ion density and the gradient in the fast ion distribution in the relevant phase space region. While the exact phase space region providing the drive is uncertain, these two factors can be characterized in other ways using quantities calculated by RABBIT [104]. RABBIT is a code that calculates the beam ion distribution assuming no transport by instabilities. The beam density at r/a∼0.25 is used to quantify the amount of fast ions available to transfer energy. Since the gradient is expected to be caused by the loss boundary, the amount of power lost to loss orbit can be used as a proxy for the gradient of the distribution; the higher the losses, the closer the center of distribution is to the boundary. Figures 4.14 and 4.15 shows the stability dependence on these quantities. No strong dependence is seen on these two quantities which mean that the variation in drive may be small compared to the variation in the growth rate.
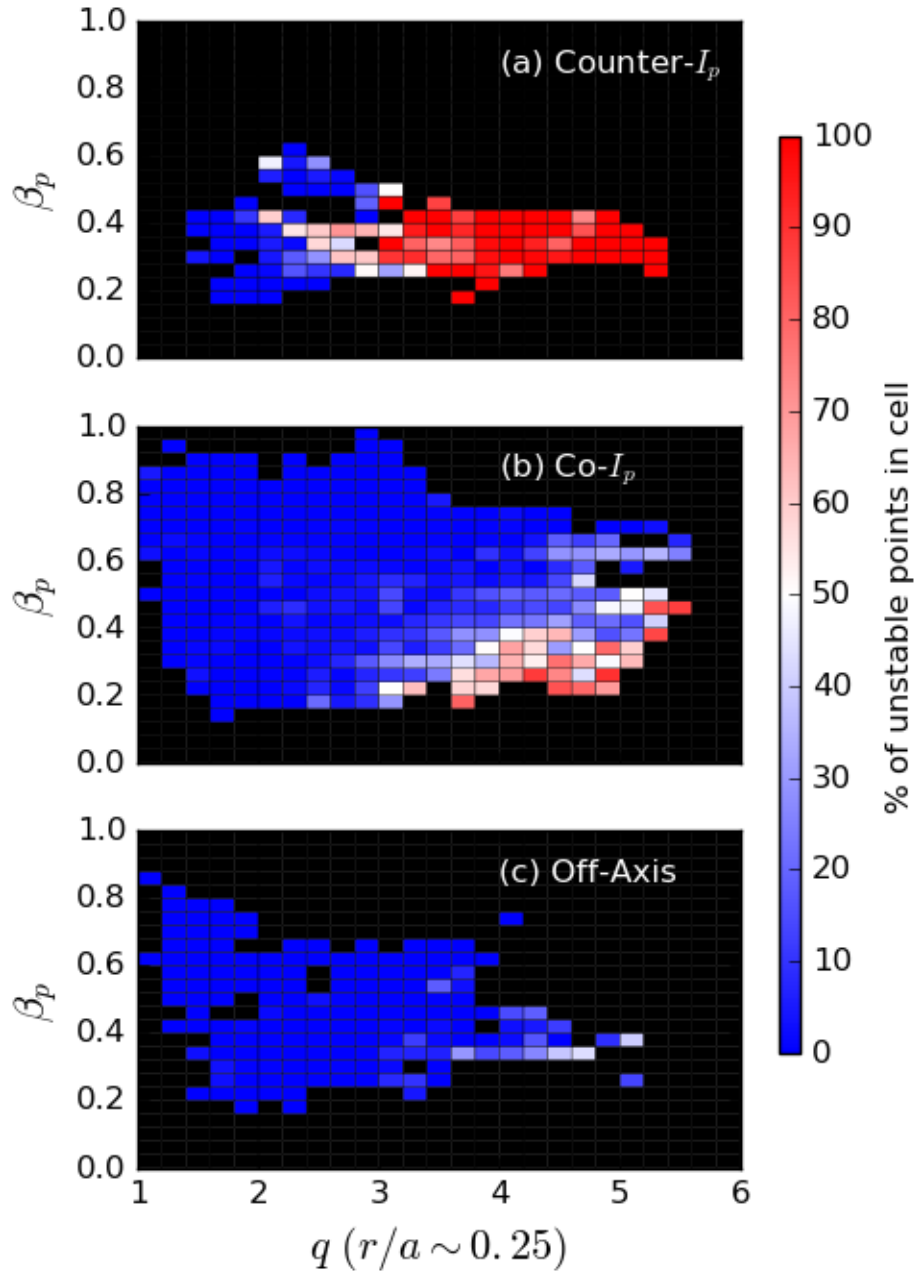
Figure 4.13: Stability map in the exclusive presence of (a) counter-$I_p$, (b) co-$I_p$, and (c) off-axis beams. The counter-$I_p$ beam has the largest unstable region followed by the co-$I_p$ beam and then the off-axis beam.
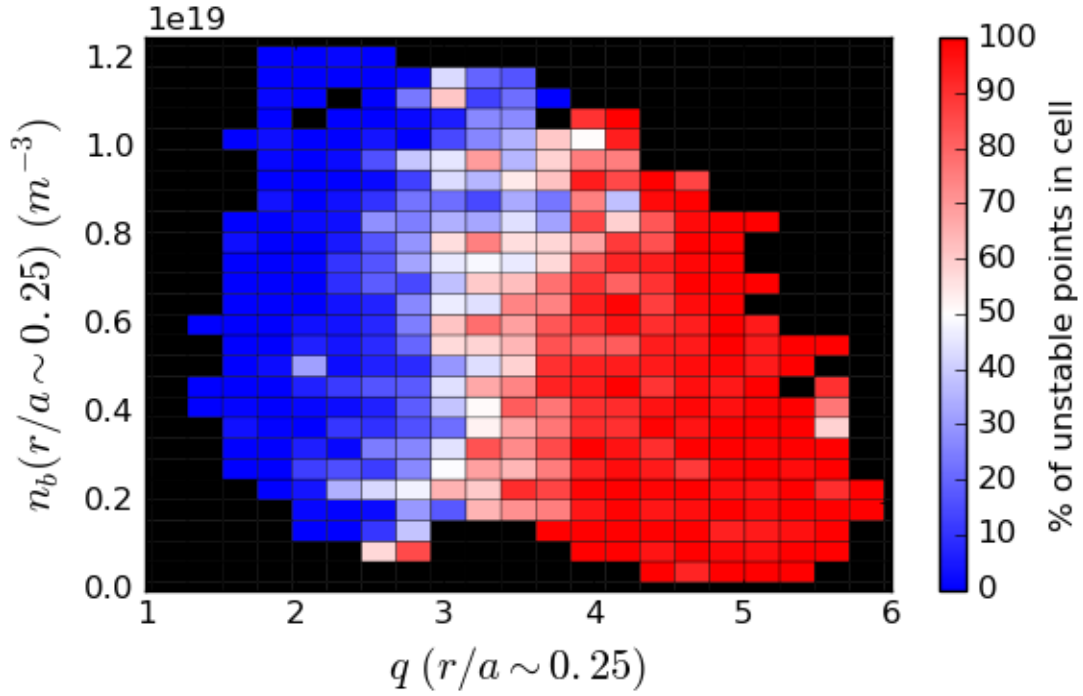
Figure 4.14: EGAM stability in the space of $q$ and beam density at $r/a{\sim}0.25$. No strong dependence on the beam density is found.
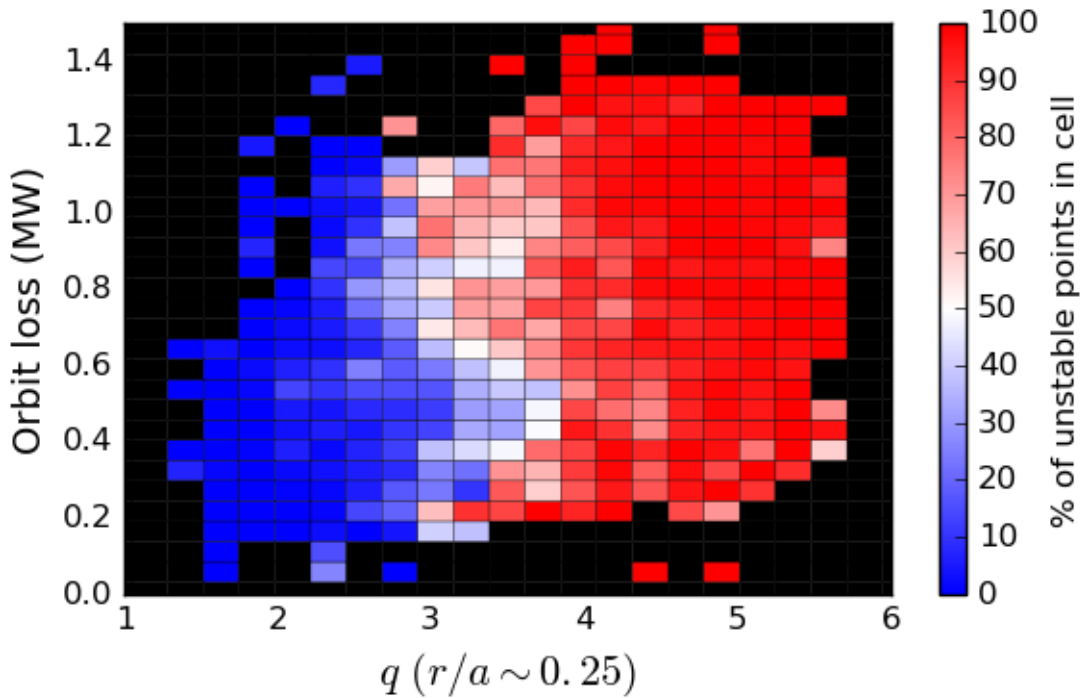


Figure 4.15: EGAM stability in the space of $q$ and power transferred to orbit losses. No clear dependence on the orbit loss is found.
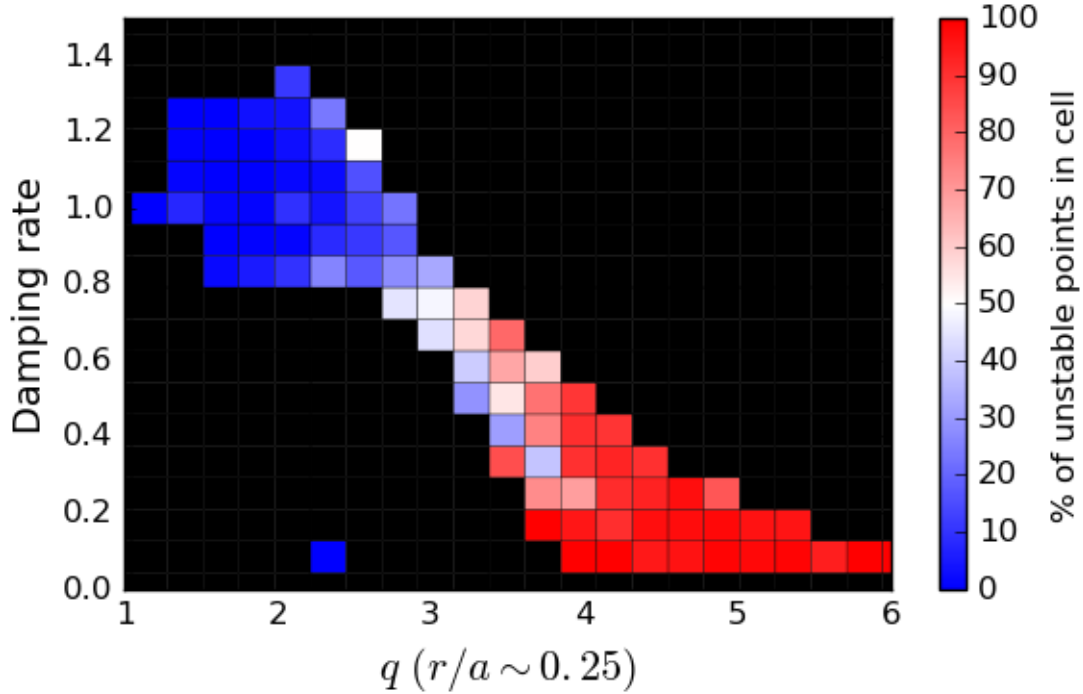
Figure 4.16: EGAM stability in the space of $q$ and damping rate. Dependence is nearly linear within the domain of the database. When the damping rate is less than ~0.7, the mode tends to be unstable

**Mode damping**

Figure 4.16 shows a stability map in the space of $q$ and the damping rate, calculated from the second term in Eq. 4.2. There is a nearly linear dependence between $q$ and the damping rate within the domain of the database. The damping rate decreases as $q$ increases and tends to be more unstable when the damping rate drops below 0.7. The strong distinction between the stable and unstable region suggests a strong stability dependence on damping rate.

### 4.5.3 2nd harmonic signal

A peak finding algorithm is employed to detect the different harmonics for EGAMs using the following steps:

1. Each time slice scanned for peaks in frequency

2. Check average coherence between each probe $> 90\%$

3. Check for n=0 mode number

4. Check that the mode is not an isolated blip

5. Harmonics are classified based on previous fitting of frequency against $q$ and density

Figure 4.17 shows histograms of the 2nd harmonic frequency. The number of 2nd harmonic points ($\sim$3000) is found to be be much less than the number of 1st harmonic points ($\sim$45000) by a factor of $\sim$15. The 2nd harmonic signals appear to be present when $q \geq 3.5$. No significant amount of other higher harmonic signals are detected in this study. A comparison of the amplitudes for the different harmonics is shown in Fig. 4.18. The 2nd harmonic amplitudes tend to be smaller than the 1st and follow a trend of $\log A_2 = 0.315 \log A_1 - 2.45$.

### 4.5.4 Turn on times

The time it takes for the mode to appear once the counter $I_p$ beam turns on is characterized. Figure 4.19 shows that the difference in time, when the beam turns on and when the mode first appears, is defined as the turn on time. Figure 4.20 plots a histogram of turn on times with mode frequency. Before the beam turns on, there should be no particles populating the resonant phase space. Once the beam turns on, the time it takes for the mode to appear is determined by the growth rate of the mode and the time it takes for particles to develop a significant gradient in the resonant region. The turn on times are $O(1ms)$ while scattering and resonant orbit times are $O(100ms)$ and $O(10\mu s)$ respectively. The largest fraction of data appears within 1 ms which indicates that modes are quickly excited once the beam turns on. There also appears to be a faint relationship where the mode takes longer to appear when the frequency is higher. This would imply that the resonant region lies further
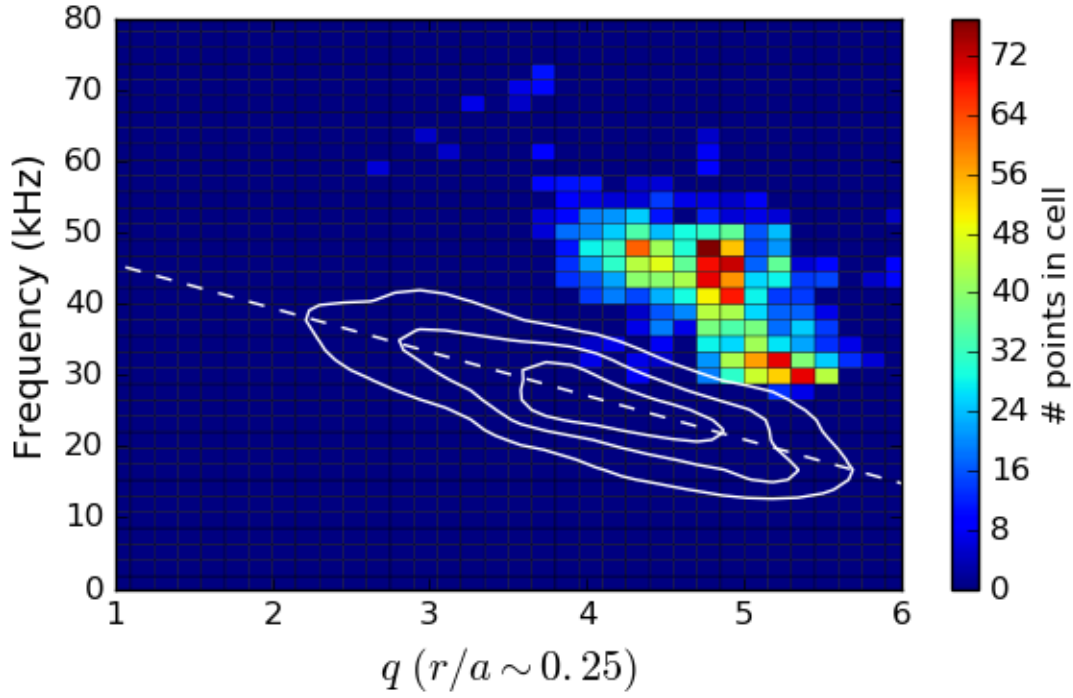
Figure 4.17: Density plot of the 2nd harmonic frequency against the $q$ value. The 2nd harmonic is typically observed when q>3.5. The density plot of the 1st harmonic and best fit line in Fig. 4.9 is represented by the white contours and white dashed line respectively.
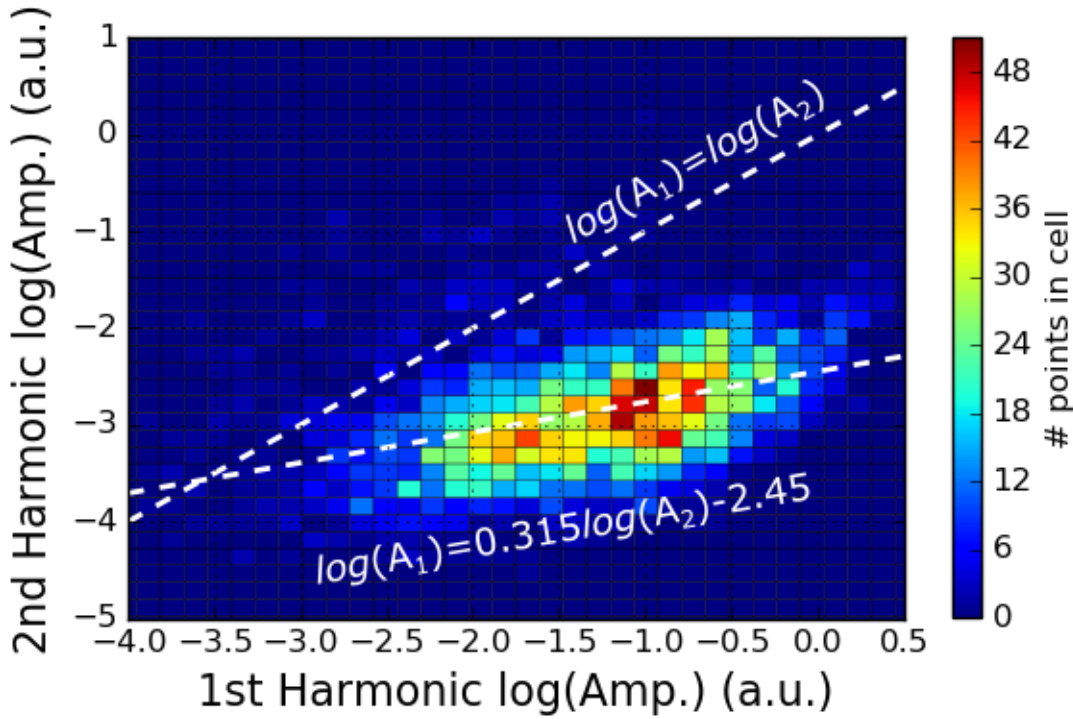


Figure 4.18: Density plot comparing the 1st harmonic amplitude with the 2nd harmonic amplitude. The 2nd harmonic amplitude is less than the 1st and increases at a slower rate.
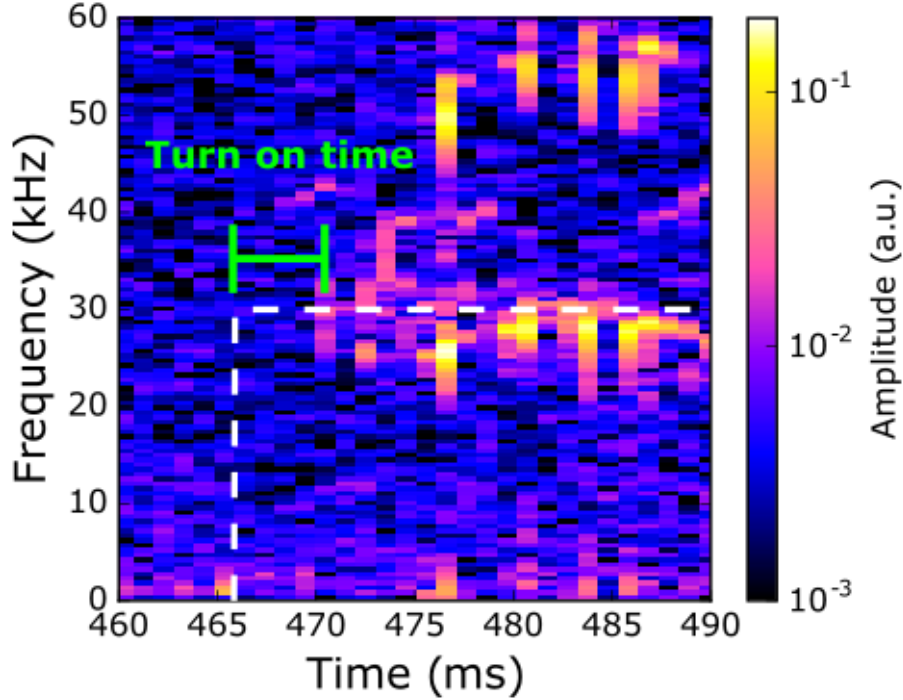
Figure 4.19: The turn on time is defined as the time it takes for the mode to appear once the beam turns on.

away from the injection location when higher frequencies are observed. Data for turn on times are sparse since at the most, only one slice per beam pulse can be used. Additionally, the resolution of the times are limited to the ∼1 ms resolution of the FFT.

## 4.5.5 Burst cycle

The nonlinear burst cycle for EGAMs is also characterized and shown in Fig. 4.21. The period between each successive burst is defined as the burst interval. From the database, there appears to be a clear exponential-like decay between the amplitude of the mode and the burst interval. This behavior is different from fishbone and TAE bursts where larger amplitudes have longer burst intervals [105]. Even though the beams replenish gradients faster in plasmas with large amplitude modes, large bursts flatten the gradient more than smaller amplitudes, which leads to a longer time before the gradient returns to the point of
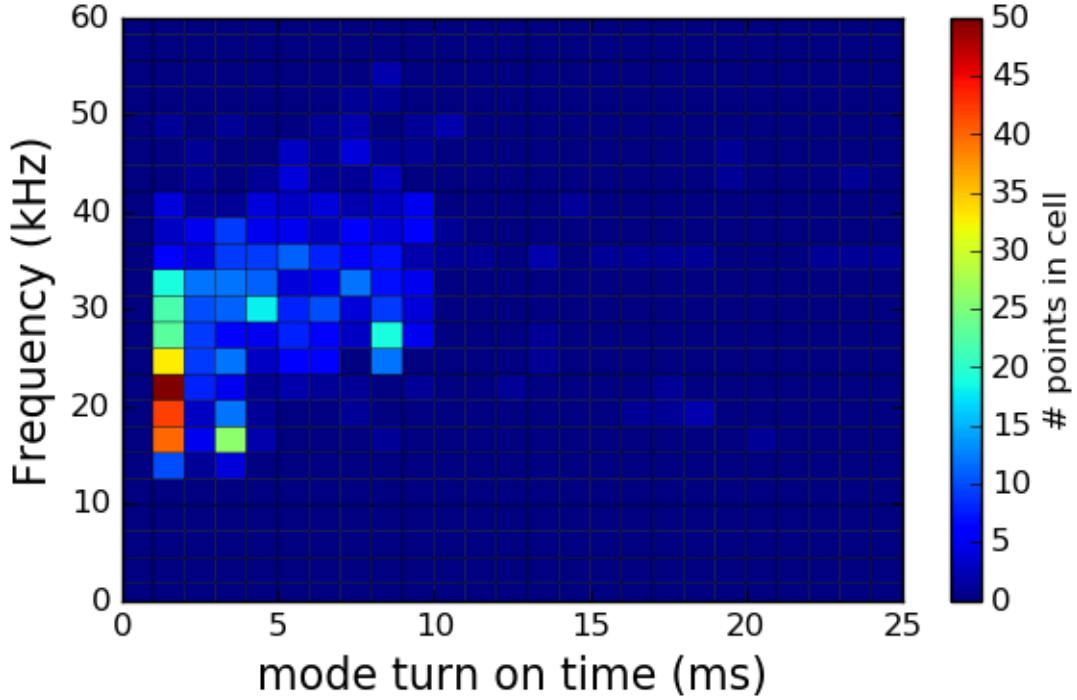
Figure 4.20: The turn on time is plotted against the frequency of the mode. The highest cluster of points appear within 1 ms. There is a faint trend where the turn on time increases with the frequency.

marginal stability. However, for EGAMs, the driving gradient may be flattened to a similar level for all amplitudes. Increased fuelling for larger amplitudes result in faster gradient recovery and shorter burst intervals.

### 4.5.6 Neutron losses

Investigation of neutron losses during EGAM bursts are performed. ZnS scintillators measure the amount of neutrons emitted from the plasma as a global measure of plasma performance. Drops in neutron emission typically correspond to events that cause confined particles to be lost. From Ref. [106], neutron losses can be characterized by

$$\nu(t) = \frac{\dot{I}_n(t_0) - \dot{I}_n(t)}{I_n(t)} \tag{4.4}$$
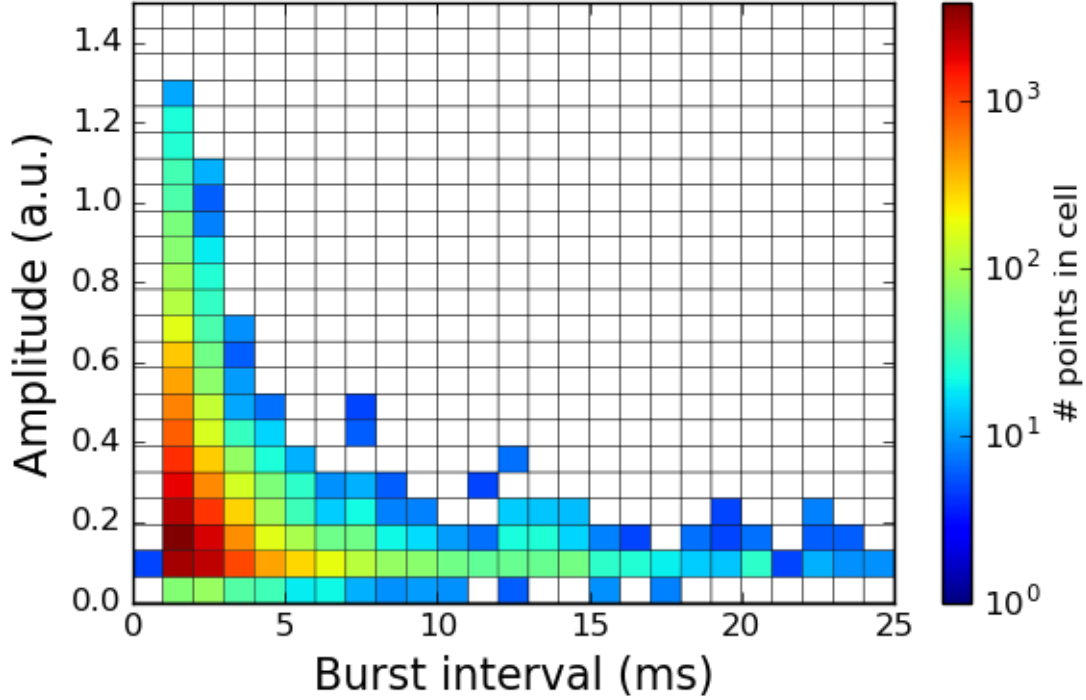
Figure 4.21: Exponential-like decay between the mode amplitude and time between successive bursts is observed.

where $\nu(t)$ is the neutron loss rate, $I_n$ is the value of the neutron emission, and $\dot{I}_n$ is the time varying change of neutron signal. The emission rate when the mode appears at time $t$ is subtracted at a time when the mode is not present at time $t_0$ and normalized to obtain the losses. Care is taken to not include neutron losses when different beams are turned on or off. Figure 4.22 shows the database results of neutron losses against mode amplitude. Neutron losses are only weakly correlated with the EGAM amplitude, possibly because only a small portion of the fast-ion distribution function is affected by the mode.

Significant losses by EGAMs, measured by drops in neutron rate, may have been overemphasized in previous studies [9]. The red points in Fig. 4.22 represent the neutron losses found in the study and appear to be an outlier compared to the rest of the database. The relatively large amount of loss is associated with counter-$I_p$ beam injection near the loss region early in the discharge. Figures 4.23(a) and 4.23(c) shows the EGAM amplitude and neutron losses for the discharge (133067) in Ref. [9], while Figs. 4.23(b) and 4.23(d) shows
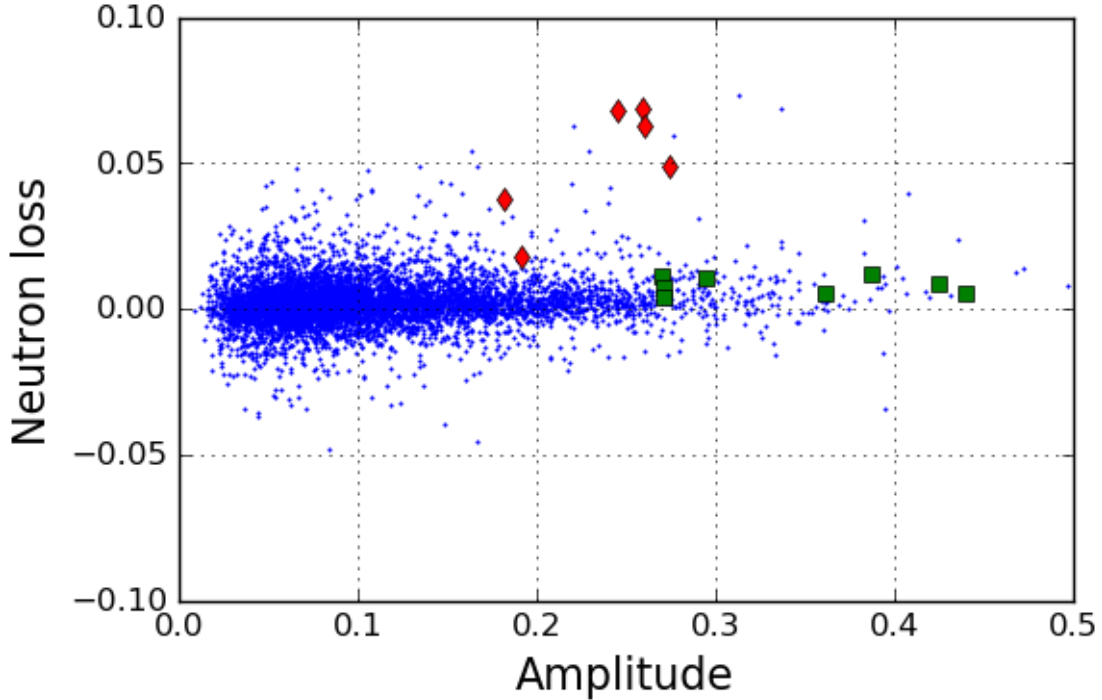
Figure 4.22: Neutron losses measured by a ZnS scintillator compared to the measured mode amplitude from magnetics. The red diamonds (133067) and green squares (159260) highlight the cases shown in Fig. 4.23. Neutron losses are centered around 0 for all mode amplitudes.

the same quantities for a different discharge (159260). The mode amplitude for shot 133067 is lower than that in shot 159260, but the neutron losses in the first case are higher than those in the second case. The window for shot 133067 occurs earlier in the discharge when neutron signals are lower due to poor confinement. Drops in neutron emission while the neutron signals are low will result in a larger loss percentage compared to the same drop when the neutron signals are higher.

## 4.6    Discussion and Summary

ASDEX reports chirping cases that spans ∼15 kHz over ∼5 ms [62], while LHD reports chirping cases that spans ∼45 kHz over ∼13 ms [60]. On DIII-D, chirping modes span over a smaller range (∼4 kHz) and period (∼1 ms). In ASDEX, EGAMs appear to resonate with
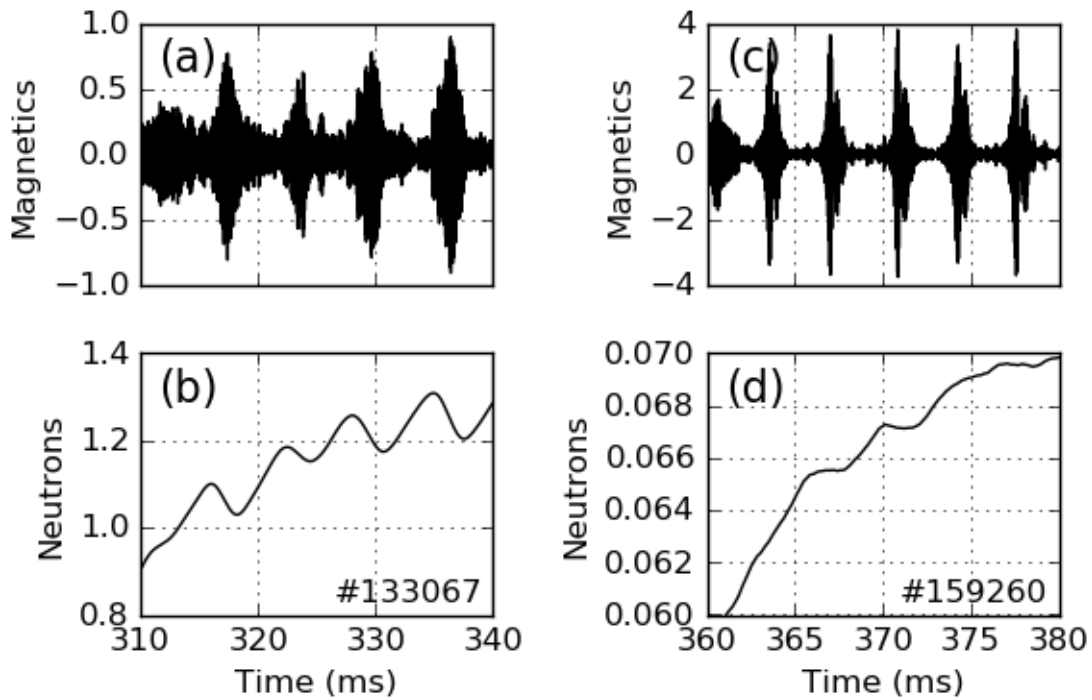
Figure 4.23: Signal from (a, c) a magnetic probe and (b, d) a ZnS neutron scintillator are plotted for a time window early in the discharges. Shot 133067 (left) was previously studied in Ref. [9] and showed significant losses corresponding with mode bursts. Shot 159260 (right) has small neutron losses at each mode burst. Neutron measurements are not absolutely calibrated and vary depending on the amplifier gain.

the fast ion distribution at lower energies (after significant time to slow down) [48]; however, in DIII-D, EGAMs appear almost immediately after the onset of injection, suggesting that the modes resonate with particles near the injection energy.

This work presents various properties of EGAMs in this database study on DIII-D. The frequency of EGAMs is typically $\sim$50% of the GAM frequency (Eq. 4.3) which is consistent with calculations from Ref. [50]. The mode frequency is strongly correlated with the safety factor $q$. The mode tends to be more unstable at high $q$ and low $\beta_p$ and is most easily destabilized by the counter $I_p$ beam. The stability of the mode is largely determined by changes in the damping rather than the drive of the mode. The 2nd harmonic of the mode appears when $q > 3.5$ and much less frequently than the 1st harmonic. The 2nd harmonic amplitude is also smaller than the 1st harmonic amplitude and displays a visible linear relationship. The mode is quickly excited once the beam turns on and there is an exponential-like decay relationship between the mode amplitude and burst interval. Further understanding of EGAMs can lead to developing new mechanisms of energy transfer between energetic particles and the bulk plasma which may lead to better heating efficiency.

# Chapter 5

# Summary and Outlook

## 5.1 D-alpha filtering technique

Section 2.4 discussed development of a new D-alpha filtering technique for the FIDA diagnostic. Reduction in the unshifted D-alpha emission is achieved to varying degrees using the reflection of a narrow bandpass filter. The performance of the filter is primarily affected by the divergence of the collimated beam. There are still improvements to be made for the D-alpha filtering technique. Currently, the out-of-band transmission is around 80% at best for the 200 $\mu$m fibers and it is too costly to filter each fiber individually. Instead, the filtering technique can be incorporated with the spectrometer design. The lens used to collimate the fibers have a larger focal length compared to the fiber collimators, which will result in a lower beam divergence (Eq. 2.4). With a lower beam divergence, the performance of the filter will improve resulting in deeper blocking and narrower width. The out-of-band transmission loss is most likely associated with the coupling of the collimated beam to an output fiber. With the filtering incorporated into the spectrometer, the collimated beam is focused onto the detector avoiding any possible coupling losses.

## 5.2 Utilization of the INPA

Chapter 3 discussed the verification and validation of signals measured by the novel INPA diagnostic. Simulated images from an experimental discharge recreate parts of the measured image. Strong passive signals are observed but are not reproduced in the simulation since the population that caused them lies outside of the simulation boundary (outside of the plasma). The result in the validation of the INPA measurement gives confidence to the diagnosis of the fast ion distribution. There are still some discrepancies with the energy dependence of the light emission from the scintillating plate that needs to be properly accounted for in the simulation. The high resolution measurement is useful for a narrow pitch range in phase space. Expansion of the coverage can be done by installing the diagnostic at different locations to probe a different pitch. The strong passive signal observed can be used to probe the fast ion distribution near the edge of the plasma if the edge neutral density is known. Conversely, as previous works have mentioned [37], robust passive signals from a well known fast ion source can lead to measurements of the edge neutral density.

## 5.3 EGAM effects on energetic particles

Chapter 4 explored and characterized the EGAM instability as observed on DIII-D. A large database is assembled to evaluate the mode properties with various plasma parameters. The mode frequency is found to strongly depend on the safety factor and is most easily excited when the counter-$I_p$ beam is on. The stability of the mode is largely determined by the damping mechanisms on DIII-D. One of the motivation for the work on characterizing the mode is to gauge its usability to facilitate energy transfer between energetic ions and the bulk plasma. Many different phenomena are observed but more work is needed to determine the mechanisms that drive each observation. While the present work found simple relationships

between two quantities, more complex relationships may be found using machine learning techniques for data mining. With the database mostly assembled, it should be straightforward to apply machine learning algorithms to find relationships between multiple different quantities. If the mode is proven to be favorable in facilitating more efficient energy transfer between the energetic and bulk ions, control of the mode would need to be developed in order exploit this beneficial aspect.

# Bibliography

[1] Plotting nuclear fusion cross sections. `https://scipython.com/blog/plotting-nuclear-fusion-cross-sections/`. Accessed: 2022-05-13.

[2] Fusion machines | Searching for the perfect shape.

[3] ITER Physics Expert Group on Energe Drive and ITER Physics Basis Editors. Chapter 5: Physics of energetic ions. *Nucl. Fusion*, 39(12):2471–2495, December 1999.

[4] R.B. White. *The Theory of Toroidally Confined Plasmas*. International series of monographs on physics. Imperial College Press, 2001.

[5] H.J. Meiden. *Thomson scattering on low and high temperature plasmas*. PhD thesis, Technische Universiteit Eindhoven, 2011.

[6] B. Geiger, M. Garcia-Munoz, W. W. Heidbrink, R. M. McDermott, G. Tardini, R. Dux, R. Fischer, V. Igochine, and the ASDEX Upgrade Team. Fast-ion D-alpha measurements at ASDEX Upgrade. *Plasma Phys. Control. Fusion*, 53(6):065010, 2011.

[7] M. García-Muñoz, H.-U. Fahrbach, and H. Zohm. Scintillator based detector for fast-ion losses induced by magnetohydrodynamic instabilities in the ASDEX upgrade tokamak. *Review of Scientific Instruments*, 80(5):053503, May 2009.

[8] X.D. Du, M.A. Van Zeeland, W.W. Heidbrink, D. Su, et al. Development of a novel scintillator-based imaging neutral particle analyzer in DIII-D tokamak. *Nucl. Fusion*, 58:082006, 2018.

[9] R. Nazikian, G. Y. Fu, M. E. Austin, H. L. Berk, R. V. Budny, N. N. Gorelenkov, W. W. Heidbrink, C. T. Holcomb, G. J. Kramer, G. R. McKee, M. A. Makowski, W. M. Solomon, M. Shafer, E. J. Strait, and M. A. Van Zeeland. Intense Geodesic Acousticlike Modes Driven by Suprathermal Ions in a Tokamak Plasma. *Phys. Rev. Lett.*, 101(18):185001, October 2008.

[10] D. J. Lin, C. M. Muscatello, and W. W. Heidbrink. Development of a narrow stopband filter for spectroscopic fast ion deuterium-alpha measurements. *Review of Scientific Instruments*, 92(3):033107, March 2021.

[11] D. J. Lin, X. D. Du, W. W. Heidbrink, and M. A. Van Zeeland. Validation of the imaging neutral particle analyzer in nearly MHD quiescent plasmas using injected beam ions on DIII-D. *Nucl. Fusion*, 60(11):112008, August 2020.

[12] D.J. Lin, W.W. Heidbrink, N.A. Crocker, X.D. Du, R. Nazikian, M.A. Van Zeeland, and K. Barada. Energetic particle-induced geodesic acoustic modes on diii-d. *Nucl. Fusion*, Submitted 2022.

[13] C. S. Collins, W. W. Heidbrink, M. Podestà, R. B. White, G. J. Kramer, D. C. Pace, C. C. Petty, L. Stagner, M. A. Van Zeeland, Y. B. Zhu, and The DIII-D. Team. Phase-space dependent critical gradient behavior of fast-ion transport due to Alfvén eigenmodes. *Nucl. Fusion*, 57(8):086005, 2017.

[14] W. W. Heidbrink and R. B. White. Mechanisms of energetic-particle transport in magnetically confined plasmas. *Phys. Plasma*, 27(3):030901, March 2020.

[15] Y. Todo. Introduction to the interaction between energetic particles and Alfven eigenmodes in toroidal plasmas. *Rev. Mod. Plasma Phys.*, 3(1):1, December 2018.

[16] C.S. Collins, W.W. Heidbrink, M.E. Austin, G.J. Kramer, D.C. Pace, C.C. Petty, L. Stagner, M.A. Van Zeeland, R.B. White, Y.B. Zhu, and DIII-D team. Observation of Critical-Gradient Behavior in Alfv\'en-Eigenmode-Induced Fast-Ion Transport. *Phys. Rev. Lett.*, 116(9):095001, February 2016.

[17] N. J. Fisch. The alpha channeling effect. *AIP Conference Proceedings*, 1689(1):020001, December 2015.

[18] W. W. Heidbrink. Fast-ion D measurements of the fast-ion distribution (invited)a). *Rev. Sci. Instrum.*, 81(10):10D727, October 2010.

[19] B. Geiger, R. Dux, R. M. McDermott, S. Potzel, M. Reich, F. Ryter, M. Weiland, D. Wünderlich, and M. Garcia-Munoz. Multi-view fast-ion D-alpha spectroscopy diagnostic at ASDEX Upgrade. *Rev. Sci. Instrum.*, 84(11):113502, November 2013.

[20] C. A. Michael, N. Conway, B. Crowley, O. Jones, W. W. Heidbrink, S. Pinches, E. Braeken, R. Akers, C. Challis, M Turnyanskiy, A. Patel, D. Muir, R. Gaffka, and S. Bailey. Dual view FIDA measurements on MAST. *Plasma Phys. Control. Fusion*, 55(9):095007, 2013.

[21] G. Z. Hao, W. W. Heidbrink, D. Liu, L. Stagner, M. Podestà, and A. Bortolon. On the scattering correction of fast-ion D-alpha signals on NSTX-U. *Rev. Sci. Instrum.*, 89(6):063507, June 2018.

[22] A. Jansen van Vuuren, B. Geiger, A. S. Jacobsen, M. Cavedon, R. Dux, and H. Köhnlein. An edge fast-ion D-alpha system installed at ASDEX Upgrade. *Rev. Sci. Instrum.*, 90(10):103501, October 2019.

[23] M. Scobey, P. Egerton, and R. Fortenberry. Advanced plasma deposition improves ultra-narrowband optical filters. *SPIE*, 2013.

[24] H. A. Macleod. *Thin-film optical filters*. CRC Press/Taylor & Francis, 4th ed edition, 2010.

[25] A. Johansen, A. Czajkowski, N. Cooper, M. Scobey, P. Egerton, and R. Fortenberry. HELIX™ Spectral Analysis System for Measuring High-Performance Thin-Film Optical Filters. *Alluxa*, June 2017.

[26] G. Best and Ö.M. Sezerman. SHEDDING LIGHT ON HYBRID OPTICS: A Tutorial in Coupling. *Optics & Photonics News, OPN*, 10(2):30–34, February 1999.

[27] M.A. Van Zeeland, X.D. Du, W.W. Heidbrink, L. Stagner, and D. Su. INPA measurements of confined fast ions in DIII-D. *JINST*, 14:C09027, 2019.

[28] W.W. Heidbrink and G.J. Sadler. The behaviour of fast ions in tokamak experiments. *Nucl. Fusion*, 34:535, 1994.

[29] S.L. Davis, D. Mueller, and C.J. Keane. Mass resolving charge-exchange system on the poloidal divertor experiment. *Rev. Sci. Instrum.*, 54:315, 1983.

[30] Y.V. Gott and A.G. Motlich. Comparative characteristics of atomic particle stripping analysers with solid and gaseous targets. *Nucl. Instrum.*, 155:443, 1978.

[31] S.J. Zweben, R.L. Boivin, R.E. Duvall, E.D. Fredrickson, R.J. Goldston, H.E. Mynick, J.D. Strachan, and R.B. White. MeV Ion Confinement in the TFTR Tokamak. *Phys. Fluids B*, 2(6):1411–1414, 1990. invited talk at the 1989 APS meeting in Anaheim.

[32] M. García-Muñoz, H.U. Fahrbach, H. Zohm, et al. Scintillator based detector for fast-ion losses induced by MHD instabilities in the ASDEX upgrade tokamak. *Rev. Sci. Instrum.*, 80:053503, 2009.

[33] D.L. Jassby. Neutral-beam-driven tokamak fusion reactors. *Nucl. Fusion*, 17:309, 1977.

[34] A. Pankin, D. McCune, R. Andre, G. Bateman, and A. Kritz. The tokamak Monte Carlo fast ion module NUBEAM in the National Transport Code Collaboration library. *Comp. Phys. Comm.*, 159, 2004.

[35] W.W. Heidbrink. Accurate measurements of the pitch-angle scattering of beam ions. *Plasma Phys.*, 9:28, 2002.

[36] W.W. Heidbrink, T. Beitzel, K.H. Burrell, R. Colchin, C.W. Guldi, and T. Kurki-Suonio. The effect of electric fields and pitch-angle scattering on the radial neutral flux. *Plasma Phys. Control. Fusion*, 44:373, 2001.

[37] N.G. Bolte, W.W. Heidbrink, D.C. Pace, M.A. Van Zeeland, and X. Chen. Measurement and simulation of passive FIDA emission from the DIII-D tokamak. *Nucl. Fusion*, 56:112023, 2016.

[38] L.L. Lao, H. St. John, R.D. Stambaugh, A.G. Kellman, and W. Pfeiffer. Reconstruction of current profile parameters and plasma shapes in tokamaks. *Nucl. Fusion*, 25(11), 1985.

[39] B.W Rice and D.G. Nilson. Simultaneous measurement of q and Er profiles using the motional Stark effect in high-performance DIII-D plasmas. 70(815), 1999.

[40] T.N. Carlstrom, G.L. Campbell, J.C. DeBoo, R. Evanko, J. Evans, C.M. Greenfield, J. Haskovec, C.L. Hsieh, E. McKee, R.T. Snider, R.E. Stockdale, P.K. Trost, and M.P. Thomas. Design and operation of the multipulse Thomson scattering diagnostic on DIII-D. *Rev. Sci. Instrum.*, 63(4901), 1992.

[41] M.E. Austin and J. Lohr. Electron cyclotron emission radiometer upgrade on the DIII-D tokamak. *Rev. Sci. Instrum.*, 74(1457), 2003.

[42] L. Zeng, G. Wang, E.J. Doyle, T.L. Rhodes, W.A. Peebles, and Q. Peng. Fast automated analysis of high-resolution reflectometer density profiles on DIII-D. *Nucl. Fusion*, 46(S677), 2006.

[43] P. Gohil, K.H. Burrell, R.J. Groebner, and R.P. Seraydarian. High spatial and temporal resolution visible spectroscopy of the plasma edge in DIII-D. *Rev. Sci. Instrum.*, 61(2949), 1990.

[44] D.G. Whyte, M.R. Wade, D.F. Finkenthal, K.H. Burrell, P. Monier-Garbet, B.W. Rice, D.P. Schissel, W.P. West, and R.D. Wood. Measurement and verification of Zeff radial profiles using charge exchange recombination spectroscopy on DIII-D. *Nucl. Fusion*, 38(3), 1998.

[45] S. Tamor. ANTIC: A code for calculation of neutral transport in cylindrical plasmas. *J. Comput. Phys.*, 40(104), 1981.

[46] O. Meneghini, S.P. Smith, L.L. Lao, O. Izacard, Q. Ren, J.M. Park, J. Candy, Z. Wang, C.J. Luna, V.A. Izzo, B.A. Grierson, P.B. Snyder, C. Holland, J. Penna, G. Lu, P. Raum, A. McCubbin, D.M. Orlov, E.A. Belli, N.M. Ferraro, R. Prater, T.H. Osborne, A.D. Turnbull, and G.M. Staebler. Integrated modeling applications for tokamak experiments with OMFIT. *Nuclear Fusion*, 55(8):083008, 2015.

[47] L. Stagner, B. Geiger, and W.W. Heidbrink. FIDASIM: A Neutral Beam and Fast-ion Diagnostic Modeling Suite. `https://doi.org/10.5281/zenodo.1341369`.

[48] B. Geiger, L. Stagner, W. W. Heidbrink, R. Dux, R. Fischer, Y. Fujiwara, A. V. Garcia, A. S. Jacobsen, A. Jansen van Vuuren, A. N. Karpushov, D. Liu, P. A. Schneider, I. Sfiligoi, P. Zs Poloskei, and M. Weiland. Progress in modelling fast-ion D-alpha spectra and neutral particle analyzer fluxes using FIDASIM. *Plasma Phys. Control. Fusion*, 62(10):105008, August 2020.

[49] X. D. Du, M. A. Van Zeeland, W. W. Heidbrink, L. Stagner, A. Wingen, D. Lin, and C. S. Collins. Resolving the fast ion distribution from imaging neutral particle analyzer measurements. *Nucl. Fusion*, 60(11):112001, August 2020.

[50] G. Y. Fu. Energetic-Particle-Induced Geodesic Acoustic Mode. *Phys. Rev. Lett.*, 101(18):185002, October 2008.

[51] G. J. Kramer, L. Chen, R. K. Fisher, W. W. Heidbrink, R. Nazikian, D. C. Pace, and M. A. Van Zeeland. Fractional Resonances between Waves and Energetic Particles in Tokamak Plasmas. *Phys. Rev. Lett.*, 109(3):035003, July 2012.

[52] R. K. Fisher, D. C. Pace, G. J. Kramer, M. A. Van Zeeland, R. Nazikian, W. W. Heidbrink, and M. García-Muñoz. Beam ion losses due to energetic particle geodesic acoustic modes. *Nucl. Fusion*, 52(12):123015, November 2012.

[53] G. D. Conway, A. I. Smolyakov, and T. Ido. Geodesic acoustic modes in magnetic confinement devices. *Nucl. Fusion*, 62(1):013001, December 2021.

[54] Yang Chen, Wenlu Zhang, Jian Bao, Zhihong Lin, Chao Dong, Jintao Cao, and Ding Li. Verification of Energetic-Particle-Induced Geodesic Acoustic Mode in Gyrokinetic Particle Simulations. *Chinese Phys. Lett.*, 37(9):095201, September 2020.

[55] P. H. Diamond, S.-I. Itoh, K. Itoh, and T. S. Hahm. Zonal flows in plasma—a review. *Plasma Phys. Control. Fusion*, 47(5):R35–R161, April 2005.

[56] H. L. Berk, C. J. Boswell, D. Borba, A. C. A. Figueiredo, T. Johnson, M. F. F. Nave, S. D. Pinches, S. E. Sharapov, and JET EFDA contributors. Explanation of the JETn= 0 chirping mode. *Nucl. Fusion*, 46(10):S888–S897, September 2006.

[57] W. Chen, X. T. Ding, L. M. Yu, X. Q. Ji, J. Q. Dong, Q. W. Yang, Yi. Liu, L. W. Yan, Y. Zhou, W. Li, X. M. Song, S. Y. Chen, Z. B. Shi, and X. R. Duan. EGAM induced by energetic electrons and nonlinear interactions among EGAM, BAEs and tearing modes in a toroidal plasma. *Physics Letters A*, 377(5):387–390, January 2013.

[58] W. Chen, X. T. Ding, L. M. Yu, X. Q. Ji, Z. B. Shi, Y. P. Zhang, W. L. Zhong, G. L. Yuan, J. Q. Dong, Q. W. Yang, Yi Liu, L. W. Yan, Y. Zhou, M. Jiang, W. Li, X. M. Song, S. Y. Chen, and X. R. Duan and. Observation of energetic-particle-induced GAM and nonlinear interactions between EGAM, BAEs and tearing modes on the HL-2A tokamak. *Nucl. Fusion*, 53(11):113010, September 2013.

[59] T. Ido, A. Shimizu, M. Nishiura, S. Nakamura, S. Kato, H. Nakano, Y. Yoshimura, K. Toi, K. Ida, M. Yoshinuma, S. Satake, F. Watanabe, S. Morita, M. Goto, K. Itoh, S. Kubo, T. Shimozuma, H. Igami, H. Takahashi, I. Yamada, and K. Narihara and. Potential fluctuation associated with the energetic-particle-induced geodesic acoustic mode in the Large Helical Device. *Nucl. Fusion*, 51(7):073046, June 2011.

[60] T. Ido, M. Osakabe, A. Shimizu, T. Watari, M. Nishiura, K. Toi, K. Ogawa, K. Itoh, I. Yamada, R. Yasuhara, Y. Yoshimura, and S. Kato and. Identification of the energetic-particle driven GAM in the LHD. *Nucl. Fusion*, 55(8):083024, July 2015.

[61] T. Ido, K. Itoh, M. Osakabe, M. Lesur, A. Shimizu, K. Ogawa, K. Toi, M. Nishiura, S. Kato, M. Sasaki, K. Ida, S. Inagaki, S.-I. Itoh, and the LHD Experiment Group. Strong Destabilization of Stable Modes with a Half-Frequency Associated with Chirping Geodesic Acoustic Modes in the Large Helical Device. *Phys. Rev. Lett.*, 116(1):015002, January 2016.

[62] L. Horváth, G. Papp, Ph Lauber, G. Por, A. Gude, V. Igochine, B. Geiger, M. Maraschek, L. Guimarais, V. Nikolaeva, and G. I. Pokol and. Experimental investigation of the radial structure of energetic particle driven modes. *Nucl. Fusion*, 56(11):112003, July 2016.

[63] Ming Xu, Jizong Zhang, Tianchun Zhou, Yanmin Duan, Liqun Hu, Yingying Li, Liqing Xu, Tonghui Shi, Yong Liu, Songtao Mao, and Juan Huang and. Observation of electromagnetic GAMs excited by NBI in EAST. *Nucl. Fusion*, 58(9):096004, July 2018.

[64] H. L. Berk and T. Zhou. Fast excitation of EGAM by NBI. *Nucl. Fusion*, 50(3):035007, March 2010.

[65] Zhiyong Qiu, , Liu Chen, and . Kinetic Theories of Geodesic Acoustic Modes: Radial Structure, Linear Excitation by Energetic Particles and Nonlinear Saturation. *Plasma Sci. Technol.*, 13(3):257, June 2011.

[66] Jean-Baptiste Girardo, David Zarzoso, Rémi Dumont, Xavier Garbet, Yanick Sarazin, and Sergei Sharapov. Relation between energetic and standard geodesic acoustic modes. *Physics of Plasmas*, 21(9):092507, September 2014.

[67] Z. Qiu, F. Zonca, and L. Chen. Geodesic acoustic mode excitation by a spatially broad energetic particle beam. *Physics of Plasmas*, 19(8):082507, August 2012.

[68] D. Zarzoso, X. Garbet, Y. Sarazin, R. Dumont, and V. Grandgirard. Fully kinetic description of the linear excitation and nonlinear saturation of fast-ion-driven geodesic acoustic mode instability. *Physics of Plasmas*, 19(2):022102, February 2012.

[69] D. Zarzoso, Y. Sarazin, X. Garbet, R. Dumont, A. Strugarek, J. Abiteboul, T. Cartier-Michaud, G. Dif-Pradalier, Ph. Ghendrih, V. Grandgirard, G. Latu, C. Passeron, and O. Thomine. Impact of Energetic-Particle-Driven Geodesic Acoustic Modes on Turbulence. *Phys. Rev. Lett.*, 110(12):125002, March 2013.

[70] A. Biancalani, A. Bottino, Ph Lauber, and D. Zarzoso. Numerical validation of the electromagnetic gyrokinetic code NEMORB on global axisymmetric modes. *Nucl. Fusion*, 54(10):104004, October 2014.

[71] D. Zarzoso, A. Biancalani, A. Bottino, Ph Lauber, E. Poli, J.-B. Girardo, X. Garbet, and R. J. Dumont. Analytic dispersion relation of energetic particle driven geodesic acoustic modes and simulations with NEMORB. *Nucl. Fusion*, 54(10):103006, September 2014.

[72] D. Zarzoso, P. Migliano, V. Grandgirard, G. Latu, and C. Passeron. Nonlinear interaction between energetic particles and turbulence in gyro-kinetic simulations and impact on turbulence properties. *Nucl. Fusion*, 57(7):072011, June 2017.

[73] Hao Wang, Yasushi Todo, Takeshi Ido, and Yasuhiro Suzuki. Chirping and Sudden Excitation of Energetic-Particle-Driven Geodesic Acoustic Modes in a Large Helical Device Experiment. *Phys. Rev. Lett.*, 120(17):175001, April 2018.

[74] Hao Wang, Yasushi Todo, Masaki Oasakabe, Takeshi Ido, and Yasuhiro Suzuki. Simulation of energetic particle driven geodesic acoustic modes and the energy channeling in the Large Helical Device plasmas. *Nucl. Fusion*, 59(9):096041, August 2019.

[75] A. G. Elfimov, R. M. O. Galvão, and N. N. Gorelenkov. Geodesic modes driven by untrapped resonances of NB energetic ions in tokamaks. *Physics of Plasmas*, 26(10):102508, October 2019.

[76] Zhiyong Qiu, Fulvio Zonca, and Liu Chen. Nonlocal theory of energetic-particle-induced geodesic acoustic mode. *Plasma Phys. Control. Fusion*, 52(9):095003, July 2010.

[77] Jintao Cao, Zhiyong Qiu, and Fulvio Zonca. Fast excitation of geodesic acoustic mode by energetic particle beams. *Physics of Plasmas*, 22(12):124505, December 2015.

[78] Ya I. Kolesnichenko, V. V. Lutsenko, Yu V. Yakovenko, B. S. Lepiavko, B. Grierson, W. W. Heidbrink, and R. Nazikian. Manifestations of the geodesic acoustic mode driven by energetic ions in tokamaks. *Plasma Phys. Control. Fusion*, 58(4):045024, March 2016.

[79] Z.S. Qu, M.J. Hole, and M. Fitzgerald. Energetic Geodesic Acoustic Modes Associated with Two-Stream-like Instabilities in Tokamak Plasmas. *Phys. Rev. Lett.*, 116(9):095004, March 2016.

[80] Xijin Xiang and Guoyong Fu. Linear properties of global energetic particle induced geodesic acoustic mode with bump-on-tail distribution in tokamak plasmas. *Physics of Plasmas*, 26(3):032509, March 2019.

[81] Ya I. Kolesnichenko, B. S. Lepiavko, and V. V. Lutsenko. Geodesic acoustic mode in tokamaks: local consideration and eigenvalue analysis. *Plasma Phys. Control. Fusion*, 55(12):125007, November 2013.

[82] Hao Wang, Yasushi Todo, Takeshi Ido, and Masaki Osakabe. Simulation study of high-frequency energetic particle driven geodesic acoustic mode. *Physics of Plasmas*, 22(9):092507, September 2015.

[83] M. Sasaki, N. Kasuya, K. Itoh, K. Hallatschek, M. Lesur, Y. Kosuga, and S.-I. Itoh. A branch of energetic-particle driven geodesic acoustic modes due to magnetic drift resonance. *Physics of Plasmas*, 23(10):102501, October 2016.

[84] Haijun Ren. Energetic particle driven geodesic acoustic mode in a toroidally rotating tokamak plasma. *Nucl. Fusion*, 57(1):016023, November 2016.

[85] G. Y. Fu. On nonlinear self-interaction of geodesic acoustic mode driven by energetic particles. *Journal of Plasma Physics*, 77(4):457–467, August 2011.

[86] M. Lesur, K. Itoh, T. Ido, M. Osakabe, K. Ogawa, A. Shimizu, M. Sasaki, K. Ida, S. Inagaki, S.-I. Itoh, and the LHD Experiment Group. Nonlinear Excitation of Subcritical Instabilities in a Toroidal Plasma. *Phys. Rev. Lett.*, 116(1):015003, January 2016.

[87] M. Lesur, K. Itoh, T. Ido, S.-I. Itoh, Y. Kosuga, M. Sasaki, S. Inagaki, M. Osakabe, K. Ogawa, A. Shimizu, and K. Ida and. Nonlinear excitation of subcritical fast ion-driven modes. *Nucl. Fusion*, 56(5):056009, April 2016.

[88] Hao Wang, Yasushi Todo, and Charlson C. Kim. Hole-Clump Pair Creation in the Evolution of Energetic-Particle-Driven Geodesic Acoustic Modes. *Phys. Rev. Lett.*, 110(15):155006, April 2013.

[89] G. Wang, W. A. Peebles, T. L. Rhodes, M. E. Austin, Z. Yan, G. R. McKee, R. J. La Haye, K. H. Burrell, E. J. Doyle, J. C. Hillesheim, M. J. Lanctot, R. Nazikian, C. C. Petty, L. Schmitz, S. Smith, E. J. Strait, M. Van Zeeland, and L. Zeng. Multi-field characteristics and eigenmode spatial structure of geodesic acoustic modes in DIII-D L-mode plasmas. *Physics of Plasmas*, 20(9):092501, September 2013.

[90] Ya. I. Kolesnichenko, V. V. Lutsenko, and B. S. Lepiavko. Cooling and transport of energetic ions due to the global geodesic acoustic mode. *Physics Letters A*, 378(36):2683–2687, July 2014.

[91] M. Sasaki, N. Kasuya, K. Itoh, Y. Kosuga, M. Lesur, K. Hallatschek, and S.-I. Itoh. Toroidal momentum channeling of geodesic acoustic modes driven by fast ions. *Nucl. Fusion*, 57(3):036025, January 2017.

[92] I. Novikau, A. Biancalani, A. Bottino, Ph. Lauber, E. Poli, P. Manz, G. D. Conway, A. Di Siena, N. Ohana, E. Lanti, and L. Villard. Nonlinear dynamics of energetic-particle driven geodesic acoustic modes in ASDEX Upgrade. *Physics of Plasmas*, 27(4):042512, April 2020.

[93] F. Camilo de Souza, G. Gorelenkov, A. Elfimov, R. Galvao, C. Collins, M. Podesta, and E. Fredrickson. Description of global egam in the maximum of local frequency during current ramp-up discharges in DIII-D. *Journal of Plasma Physics*, page submitted, 2021.

[94] T. N. Carlstrom, D. R. Ahlgren, and J. Crosbie. Real-time, vibration-compensated $CO_2$ interferometer operation on the DIII-D tokamak. *Review of Scientific Instruments*, 59(7):1063–1066, July 1988.

[95] G. McKee, R. Ashley, R. Durst, R. Fonck, M. Jakubowski, K. Tritz, K. Burrell, C. Greenfield, and J. Robinson. The beam emission spectroscopy diagnostic on the DIII-D tokamak. *Review of Scientific Instruments*, 70(1):913–916, January 1999.

[96] T. L. Rhodes, K. Barada, W. A. Peebles, and N. A. Crocker. Simultaneous measurement of magnetic and density fluctuations via cross-polarization scattering and Doppler backscattering on the DIII-D tokamak. *Review of Scientific Instruments*, 87(11):11E726, November 2016.

[97] James A. Rome and Y.-K. M. Peng. The topology of tokamak orbits. *Nucl. Fusion*, 19(9):1293–1205, September 1979.

[98] A.P. Smirnov and R.W. Harvey. *The GENRAY Ray Tracing Code*, 2001.

[99] M. A. Van Zeeland, J. H. Yu, W. W. Heidbrink, N. H. Brooks, K. H. Burrell, M. S. Chu, A. W. Hyatt, C. Muscatello, R. Nazikian, N. A. Pablant, D. C. Pace, W. M. Solomon, and M. R. Wade. Imaging key aspects of fast ion physics in the DIII-D tokamak. *Nucl. Fusion*, 50(8):084002, July 2010.

[100] William W Heidbrink, Erik Hansen, Max E Austin, Gerrit J Kramer, and Michael A Van Zeeland. The radial phase variation of reversed-shear and toroidicity-induced Alfvén eigenmodes in DIII-D. *Nucl. Fusion*, 2022.

[101] W.W. Heidbrink, M.A. Van Zeeland, M.E. Austin, A. Bierwage, Liu Chen, G.J. Choi, P. Lauber, Z. Lin, G.R. McKee, and D.A. Spong. 'BAAE' instabilities observed without fast ion drive. *Nucl. Fusion*, 61(1):016029, January 2021.

[102] Niels Winsor, John L. Johnson, and John M. Dawson. Geodesic Acoustic Waves in Hydromagnetic Systems. *The Physics of Fluids*, 11(11):2448–2450, November 1968.

[103] O. P. Fesenyuk, Ya. I. Kolesnichenko, and Yu. V. Yakovenko. Frequencies of the geodesic acoustic mode and Alfvén gap modes in high-q2 plasmas with non-circular cross section. *Physics of Plasmas*, 20(12):122503, December 2013.

[104] M. Weiland, R. Bilato, R. Dux, B. Geiger, A. Lebschy, F. Felici, R. Fischer, D. Rittich, M. van Zeeland, and and. RABBIT: Real-time simulation of the NBI fast-ion distribution. *Nucl. Fusion*, 58(8):082032, July 2018.

[105] W. W. Heidbrink, H. H. Duong, J. Manson, E. Wilfrid, C. Oberman, and E. J. Strait. The nonlinear saturation of beam-driven instabilities: Theory and experiment. *Physics of Fluids B: Plasma Physics*, 5(7):2176–2186, July 1993.

[106] J. D. Strachan, B. Grek, W. Heidbrink, D. Johnson, S. M. Kaye, H. W. Kugel, B. Le Blanc, and K. McGuire. Studies of energetic ion confinement during fishbone events in PDX. *Nucl. Fusion*, 25(8):863–880, August 1985.

# Appendix A

# FIDA GUI on DIII-D

This material covers the use of the FIDA GUI on DIII-D for streamlined analysis of experimental measurements. Access to the DIII-D iris cluster is required to use the GUI.

## A.1   Running the GUI

On iris use the following commands to launch the FIDA GUI in IDL:

```
$ module load ep
$ fidagui
```

## A.2   FIDA GUI settings

1. Options across the top applies for the different tabs (Fig. A.1)

    (a) Shot: shot number

Figure A.1: Settings on the top part of the GUI

(b) Diag: diagnostic system to use (oblique, CER, or main ion), dedicated FIDA system uses oblique

(c) Fudge: cross talk correction specifically for the 3G system during the 2015 and 2016 campaign

(d) Beam: active diagnostic beam to use

(e) Extra Chords: option to add additional chords to view

(f) Load: load data for a particular shot

(g) t: central time for analysis

(h) dt: half the averaging width ($\Delta$t = (t+dt) – (t-dt))

(i) FIDA range: integrated wavelength range for profiles

2. FPLOT tab views the spectra (Fig. A.2)

(a) Scroll bars under the plot adjusts the chord (left) and central time (right) to view

(b) Plotting range can be adjusted either by left-clicking the corners of the desired region, or entering the it into the fields provided (xrange and yrange). Note that right-clicking the plot anywhere will reset the plot to the central time and stated range

   i. Auto: automatically plot the full y-range of the data

(c) Log scale: changes plot to be logarithmic in y

(d) Average: averages the spectra within $\Delta$t

(e) Background: set the wavelength range, for the selected chord, where signal is assumed to be unchanging when beam is on/off
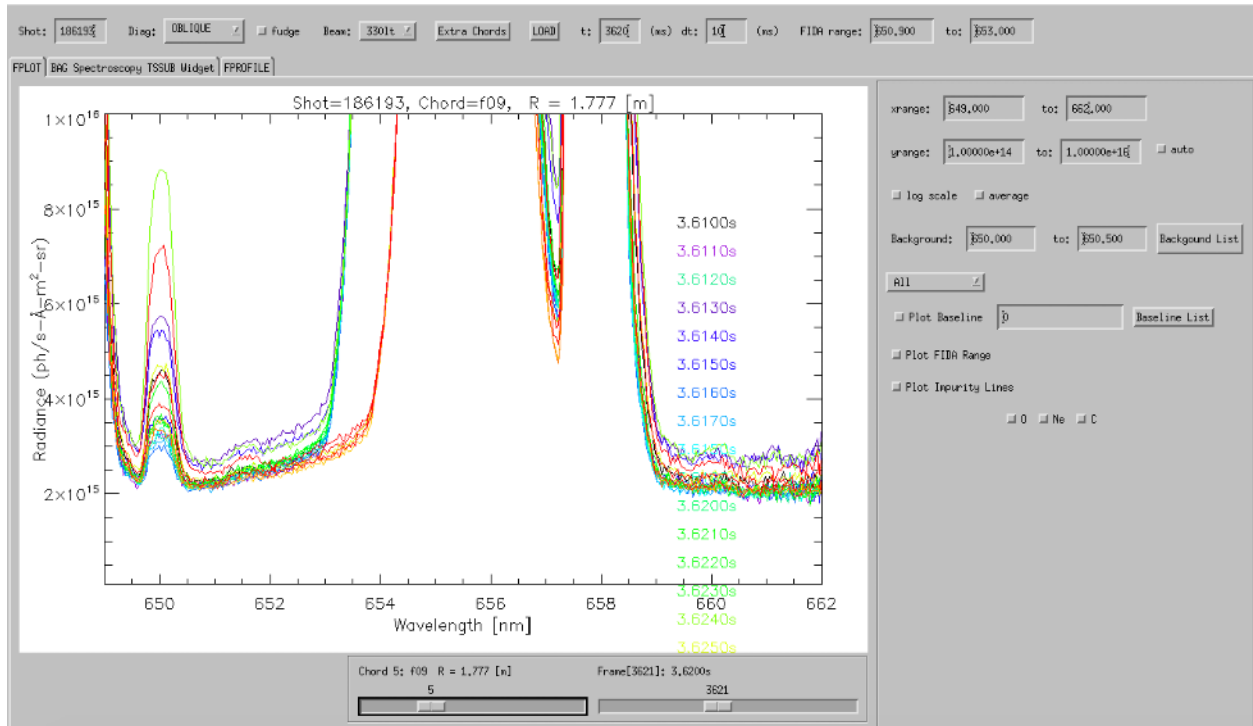
Figure A.2: GUI display of the spectra plotting tab (fplot)

(f) Choice to plot calibrated spectra (All), raw uncalibrated data (Raw), time slice subtracted data (TSSUB), or active beam data (Active) in drop down menu. Note that the raw data contains subtraction with frames when no plasma is present. TSSUB and Active data require data obtained from the next tab.

(g) Plot Baseline: Plots the baseline defined in the field. The baseline is used to determine offset for TSSUB data. If left blank, wavelength range defined in background is used

(h) Plot FIDA Range: plots the range defined in FIDA range

(i) Plot Impurity Lines: plots impurity lines for commonly seen emissions

   i. O: oxygen emissions

   ii. Ne: neon emissions

   iii. C: carbon emissions

3. TSSUB tab aids in finding acceptable time slices for time slice subtraction (Fig. A.3)
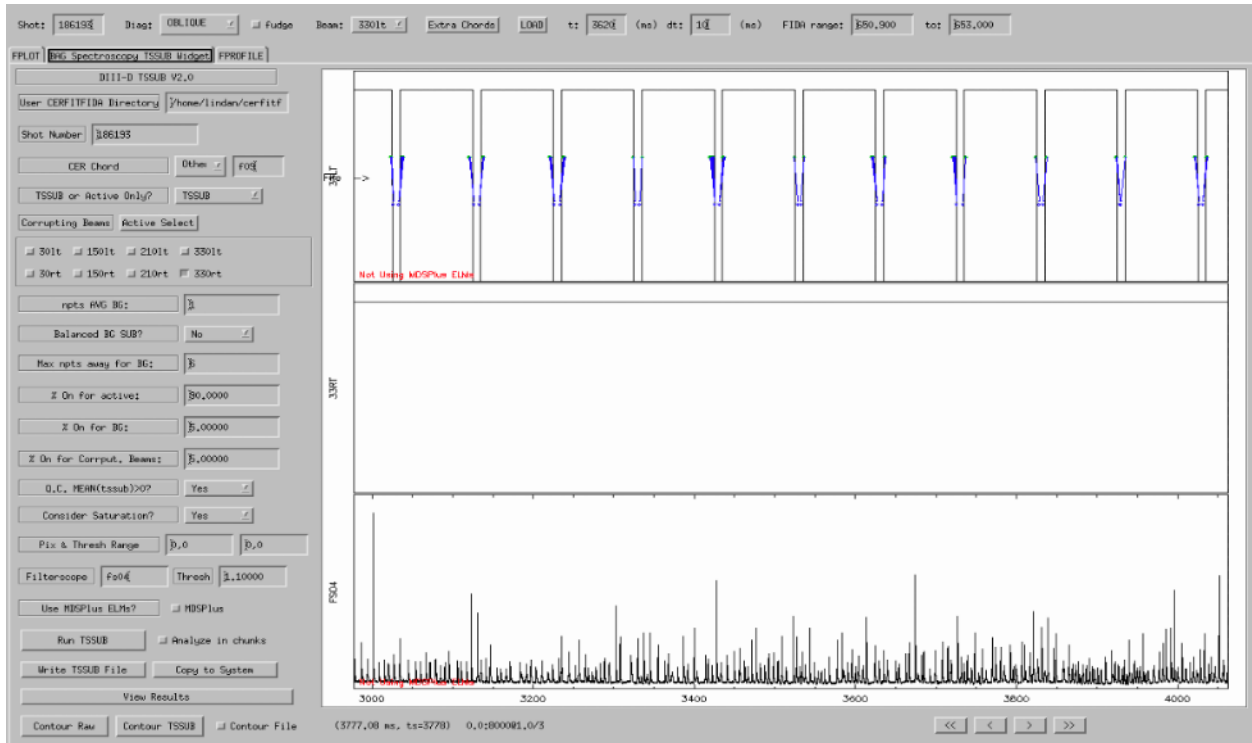
Figure A.3: GUI display of the time slice selection tab (TSSUB)

(a) Plotting range can be changed by dragging across desired time range or scrolling with arrow buttons on the bottom. Note that a single left click will reset the plot range

(b) User CERFITFIDA Directory: directory where timing data is stored (defaults to /home/$USER/cerfitfida)

(c) Shot Number: shot number (defaults to shot stated above)

(d) CER Chord: Chord to view integration time (f09 should be sufficient to use)

(e) TSSUB or Active Only?: Choice to analyze TSSUB (finds appropriate times with beam off slices) or Active (finds appropriate times without beam off slices)

(f) Corrupting Beams: used during TSSUB analysis to determine beams that might corrupt measurement

(g) Active Select: used during Active analysis to determine beams used in conjunction with diagnostic beam

(h) npts AVG BG: number of background points to average

(i) Max npts away for BG: furthest distance that time slices can be associated with a background slice

(j) % On for active: percentage of the beam on within a single time slice to be considered on

(k) % On for BG: percentage of beam off within a single time slice to be considered off

(l) % On for Corrupt. Beams: percentage of the corrupting beam on within a single time slice to be considered on

(m) Consider Saturation?: yes rejects slices if saturation is present

(n) Filterscope: selects which filterscope to use to view ELMs (fs04 seems to work)

(o) Thresh: Normalized threshold to determine whether an ELM is present

(p) Run TSSUB: finds valid time slices within plotted range

    i. Analyze in chunks: does not override previously analyzed chunk in time if checked

(q) Write TSSUB File: writes TSSUB file for the selected chord

(r) Copy to System: copies TSSUB file to all similar chords

(s) View Results: refreshes plot with current settings

(t) Contour Raw: contour plots of raw data for selected range

(u) Contour TSSUB: contour plots of TSSUB data

(v) Contour File: plots contour from file if checked

4. FPROFILE tab views the profile (Fig. A.4)

(a) Plotting range can be adjusted either dragging across the desired region, or entering the it into the fields provided (xrange and yrange). Note that right-clicking the plot anywhere will reset the plot range
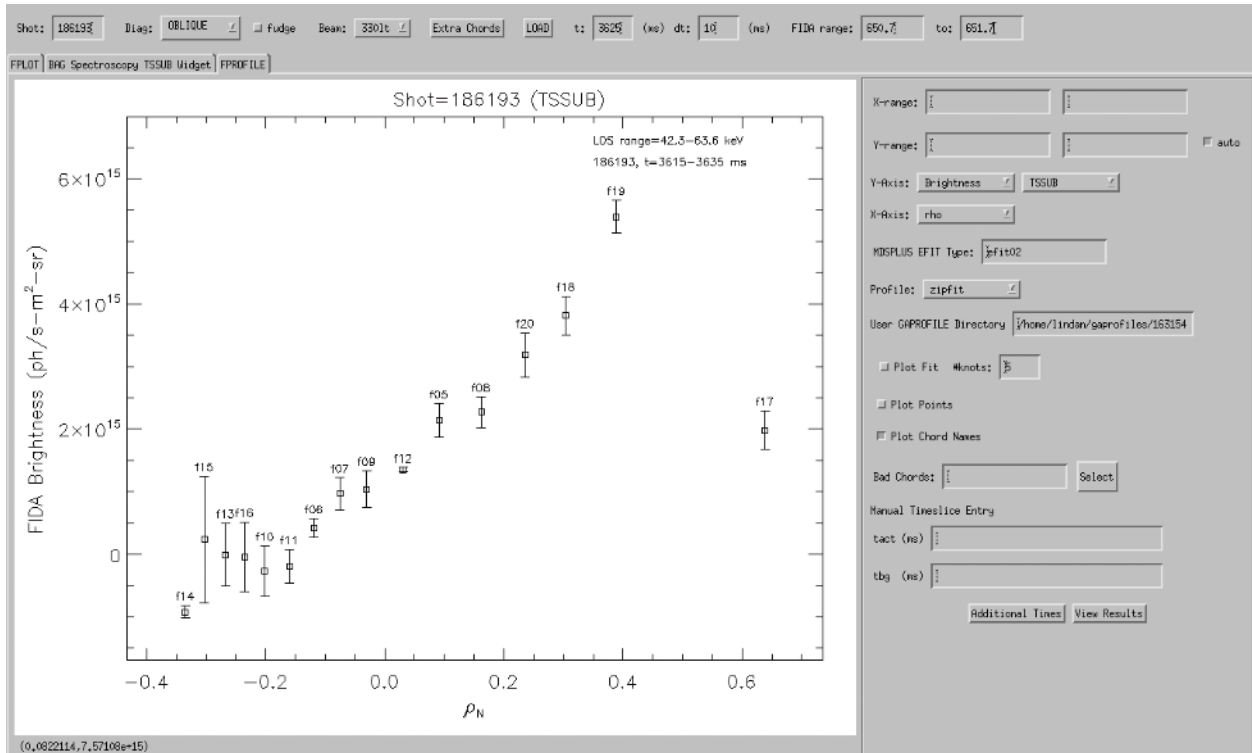
Figure A.4: GUI display of the profile plotting tab (fprofile)

  - Auto: automatically plot the full y-range of the data

(b) Y-Axis: choice to plot different data types

  i. Brightness: integrated radiance over specified wavelength range

  ii. Density: brightness values corrected with a rough estimation of the neutral beam density

  iii. NB Density: neutral beam density

  iv. TSSUB: time slice subtracted data

  v. Active Only: data without background subtraction

(c) X-Axis: choice to plot against different axis

  i. rho: radial position in normalized flux coordinates determined by the specified EFIT

  ii. R_major: radial position in machine coordinates

  iii. Time: plot series of data in time

(d) Profile: profiles to use to estimate beam deposition (zipfit or gaprofiles)

(e) User GAPROFILE Directory: directory where GAProfiles are stored (defaults to /home/$USER/gaprofiles/$SHOT)

(f) Plot Fit: plots spline fit based on number of specified knots

(g) Plot Points: plot data points instead of average with error bars

(h) Plot Chord Names: plots chord names over points

(i) Bad Chords: chords to ignore when plotting

(j) Manual Timeslice Entry: manually enter times with corresponding background times to plot

(k) Additional Times: entry to add other available TSSUB times to overplot

(l) View Results: calculates profiles based on existing settings


# A.3  Typical GUI workflow

1. Enter information at the top and load the data

2. View spectra in the FPLOT tab

3. Obtain proper time slice selection using the TSSUB tab

4. Reload the data to gather new TSSUB information using the load button

5. Check spectra in FPLOT tab

6. View profile in FPROFILE tab

# A.4   Manual data processing

1. Data can be retrieved on IDL using the get_oblique_data function after the proper routines have been compiled (one can run the fidagui from the terminal and just use the session rather than the GUI)

   ```
   IDL> shot=186193
   IDL> data=get_oblique_data(shot, /ALL)
   ```

2. The following is the relevant data structure:

   - Data
       - Shot – shot number
       - Chords – available chords
       - Beam – active beam
       - F[XX] – chord information
           * Wavelength – calibrated wavelength
           * Radius – radial position of LOS and beam intersection
           * Data – calibrated data (wavelength, time)
           * Datatime – time base of data
           * Spec – timeslice subtracted data (if available)
           * Time – time associated with spec
           * Rawdata – uncalibrated data (contains darkshot background subtraction)

# Appendix B

# EGAM correlations

This material presents the different correlation values found within the database presented in Ch. 4.

## B.1   Correlated parameters

Table B.1 shows selected correlations between multiple variables when EGAMs are observed. While correlations are useful in determining relationships, they do not necessarily reveal new information or imply causation. The first entry shows a high correlation between EGAM frequency and $q$ because the orbits of the resonant particles are affected by $q$. The correlation for the second entry simply reinforces the fact that $\beta_t$ is related to the temperature through the plasma pressure term. The correlation for the third entry is caused by the domain of the database. Since the early part of the discharge is used, quantities like $I_p$ and $\beta_t$ ramp up at similar rates (due to operational and physical constraints).

| Parameter 1 | Parameter 2 | Correlation |
|---|---|---|
| $f_{EGAM}$ | $q$ | -0.71 |
| $\beta_t$ | $T_i$ | 0.70 |
| $I_p$ | $n_e$ | 0.68 |
| Turn on time | $\beta_t$ | 0.67 |
| $I_p$ | $\beta_t$ | 0.65 |
| $I_p$ | $q$ | -0.64 |
| $\beta_t$ | $T_e$ | 0.62 |
| $\beta_t$ | $\beta_p$ | 0.61 |
| $f_{EGAM}$ | $I_p$ | 0.59 |
| $\beta_t$ | $n_e$ | 0.59 |
| $q$ | $\beta_t$ | -0.57 |
| Amplitude | $f_{EGAM}$ | -0.57 |
| $I_p$ | $T_i$ | 0.53 |
| $T_e$ | $\tau_{sl}$ | 0.52 |
| $I_p$ | $T_e$ | 0.49 |
| $f_{EGAM}$ | $n_e$ | 0.49 |
| Amplitude | $q$ | 0.48 |
| $\beta_t$ | $\tau_{PAS}$ | -0.48 |
| $q$ | $T_e$ | -0.47 |
| $\beta_p$ | $T_e$ | 0.46 |
| $f_{EGAM}$ | $\beta_t$ | 0.45 |
| Turn on time | $T_i$ | 0.44 |
| Amplitude | $I_p$ | -0.43 |
| $\beta_p$ | $T_i$ | 0.43 |
| $I_p$ | $\tau_{PAS}$ | -0.42 |
| $q$ | $T_i$ | -0.41 |
| Turn on time | $q$ | -0.41 |
| $q$ | $n_e$ | -0.41 |

Table B.1: Table of selected parameters with $r \geq |0.40|$. Correlated quantities may not directly be related.

## B.2   Stability correlation

Table B.2 shows the effect of various parameters on the stability of EGAMs. Correlation values are obtained by fitting the parameter with a corresponding value for stability (e.g. 0 for stable and 1 for unstable) and quantifies the distribution of points between the two cases.

| Parameter | Stability Correlation |
|:---------:|:---------------------:|
| $q$ | 0.72 |
| $\beta_t$ | -0.55 |
| $\beta_n$ | -0.55 |
| $W_{mhd}$ | -0.51 |
| $I_p$ | -0.40 |
| $\beta_p$ | -0.39 |
| Loss orbits | 0.33 |
| $T_e$ | 0.30 |
| $\tau_{PAS}$ | 0.30 |
| $Z$ | -0.27 |
| $P_{beam}$ | -0.25 |
| $n_{beam}$ | -0.24 |
| $\tau_{sl}$ | -0.23 |
| $\omega_\phi$ | -0.22 |
| $a$ | 0.22 |
| $B_0$ | -0.20 |
| $R_{axis}$ | -0.20 |
| $V$ | 0.19 |
| $\Delta_{top}$ | -0.18 |
| Gap in | -0.16 |
| $T_i$ | 0.15 |
| Gap top | 0.14 |
| $\Delta_{bot}$ | -0.14 |
| Gap out | -0.12 |
| $\kappa$ | -0.10 |
| Gap bottom | -0.10 |
| $n_e$ | -0.09 |
| $Z_{axis}$ | -0.01 |

Table B.2: Table of the different parameters and its correlated effect on mode stability. Correlation values are determined by fitting the parameter with a boolean value for stability.